PORTIONS

OF THIS

DOCUMENT

ARE

ILLEGIBLE

ornl

ORNL-5669

OAK RIDGE NATIONAL LABORATORY

UNION CARBIDE

Analysis of the Conceptual Shielding Design for the Upflow Gas-Cooled Fast Breeder Reactor

C. O. Slater
D. A. Reed
S. N. Cramer
M. B. Emmett
E. T. Tomlinson

OPERATED BY
UNION CARBIDE CORPORATION
FOR THE UNITED STATES
DEPARTMENT OF ENERGY

ORNL-5669
Distribution Category UC-77
Gas-Cooled Reactor Technology

Contract No. W-7405-eng-26

Engineering Physics Division

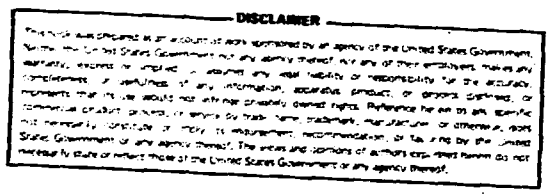

ANALYSIS OF THE CONCEPTUAL SHIELDING DESIGN FOR THE UPFLOW GAS-COOLED FAST BREEDER REACTOR

C. O. Slater
D. A. Reed[a]
S. N. Cramer
M. B. Emmett[b]
E. T. Tomlinson[b,c]

[a]University of Tennessee
[b]UCCND Computer Sciences Division
[c]Present address: Tennessee Valley Authority
Chattanooga, Tennessee

Date Published - January 1981

OAK RIDGE NATIONAL LABORATORY
Oak Ridge, Tennessee 37830
operated by
UNION CARBIDE CORPORATION
for the
DEPARTMENT OF ENERGY

TABLE OF CONTENTS

ABSTRACT. v

INTRODUCTION. 1

SHIELDING DESIGNS 1

DESIGN CONSTRAINTS ON RADIATION EXPOSURE. 5

SOURCE CALCULATIONS 5

K-Calculation. 5

Peripheral Boundary Source Calculations. 7

Full Homogeneous Model Caiculation. 7

Correction for Axial Streaming. 8

Correction for Radial Streaming 9

SHIELDING CALCULATIONS. 14

Mid-Level Regions. 14

Upper Plenum Shield. 26

Lower Plenum Shield. 28

Flow-Through Plenum Shield Slit Streaming. 34

Preliminary Flow-Through Shield Design Analysis 35

Final Flow-Through Shield Design Analysis 44

REMAINING ISSUES. 56

SUMMARY 57

ABSTRACT

Conceptual Shielding Configuration III for the Gas-Cooled Fast Breeder Reactor (GCFR) was analyzed by performing global calculations of neutron and gamma-ray fluences and correcting the results as appropriate with bias factors from localized calculations. Included among the localized calculations were the radial and axial cell streaming calculations, plus extensive preliminary calculations and three final confirmation calculations of the plenum flow-through shields. The global calculations were performed on the GCFR mid-level and the lower and upper plenum regions. Calculated activities were examined with respect to the design constraint, if any, imposed on the particular activity. The spatial distributions of several activities of interest were examined with the aid of isoplots (i.e., symbols are used to describe a surface on which the activity level is everywhere the same).

In general the results showed that most activities were below the respective design constraints. Only the total neutron fluence in the core barrel appeared to be marginal with the present reactor design. Since similar results were obtained for an earlier design, it has been proposed that the core barrel be cooled with inlet plenum gas to maintain it at a temperature low enough that it can withstand a higher fluence limit. Radiation levels in the prestressed concrete reactor vessel (PCRV) and liner appeared to be sufficiently below the design constraint that expected results from the Radial Shield Heterogeneity Experiment should not force any levels above the design constraint.

A list was also made of a number of issues which should be examined before completion of the final shielding design.

1. INTRODUCTION

After the completion of the analysis[1] of the preliminary shielding design for the upflow Gas-Cooled Fast Breeder Reactor (GCFR), the shielding design underwent major changes, and a new conceptual shielding design was established. This shielding design differs from the previous one in that helium flows through the upper and lower plenum shields rather than through gaps formed by off-setting the radial and the plenum shields. It also has a different core design called "Shielding Core Model C." This design has been dubbed "GCFR Conceptual Shielding Configuration III." (Conceptual Configuration II was the preliminary upflow shielding design, and Conceptual Configuration I was the downflow design.) This report presents the results of the analysis of the GCFR Conceptual Shielding Configuration III.

2. SHIELDING DESIGNS

The shielding design analyzed was established through correspondence from General Atomic Company (GAC) to ORNL.[2-7] Reference 2 gave the core compositions and dimensions for Shielding Core Model C. References 3-7 gave details of the radial and plenum shield designs. There were some changes to the shield design after the analysis had begun. In particular, the analysis of the portion of the GCFR between the bottom of the grid plate and the top of the exit shield/orifice region (mid-level region) was based on the design shown in Fig. 1. The upper and lower plenum shield analysis was based on the design shown in Fig. 2. While Fig. 2 shows a different arrangement for the radial shield from that of Fig. 1, the effect of those changes can be reasonably estimated, precluding the need for an expensive recalculation of the shielding in the mid-level region. The major changes occurred in the upper and lower plena. A horizontal cut through the plenum shield is shown in Fig. 3, which shows three possible designs for the flow-through paths in the shields. Two of the flow-through paths have a single bend and are called chevron slits, while the third flow-through path has two bends and is called a herringbone slit. A closeup of the chevron slit, which was selected for the conceptual design, is shown in Fig. 4. The slit has a width of either 5.08 cm (upper plenum) or 7.62 cm (lower plenum).

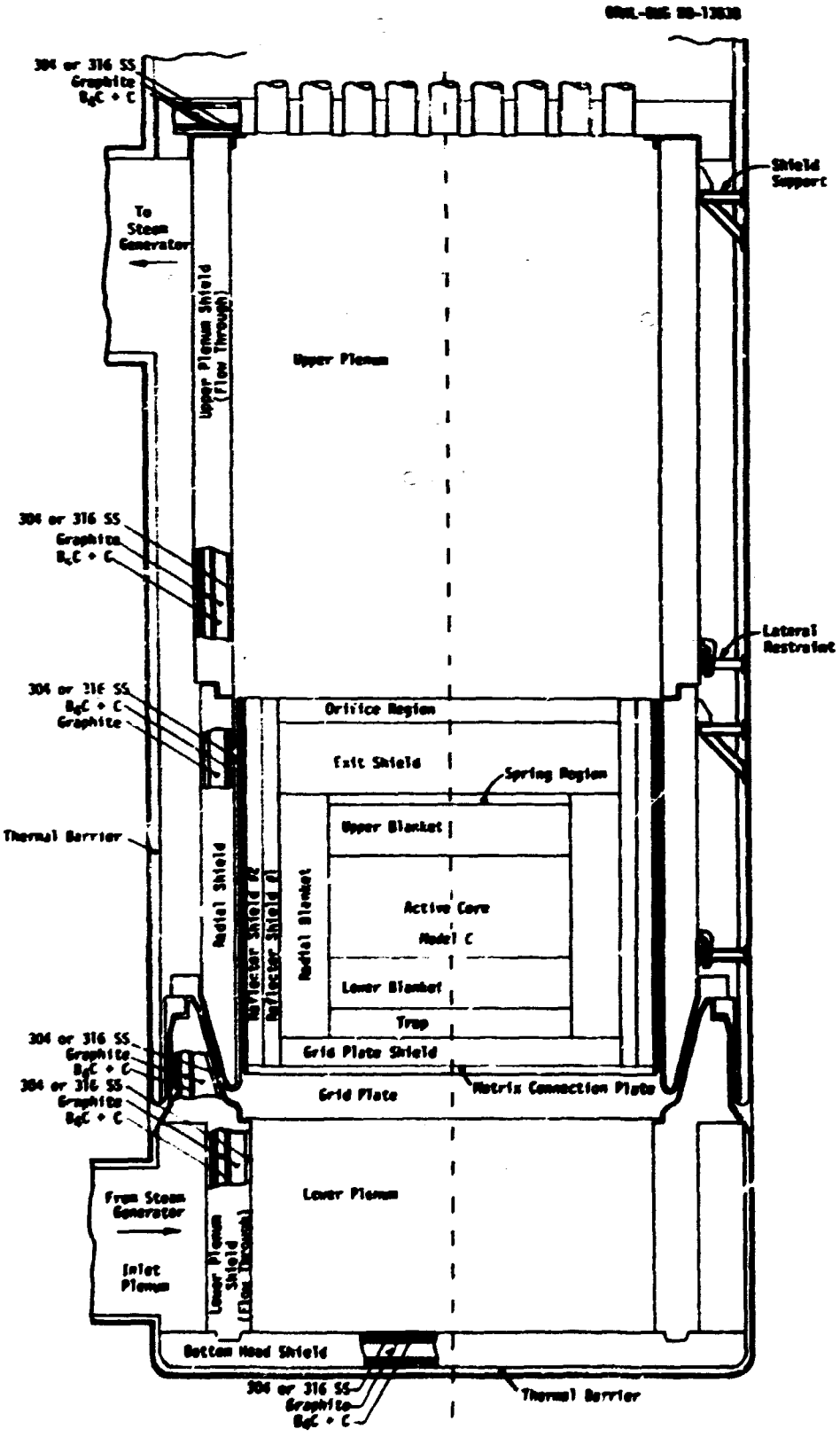

Fig. 1. Sketch of the GCFR Conceptual Shielding Configuration III design as used in the mid-level region analysis.

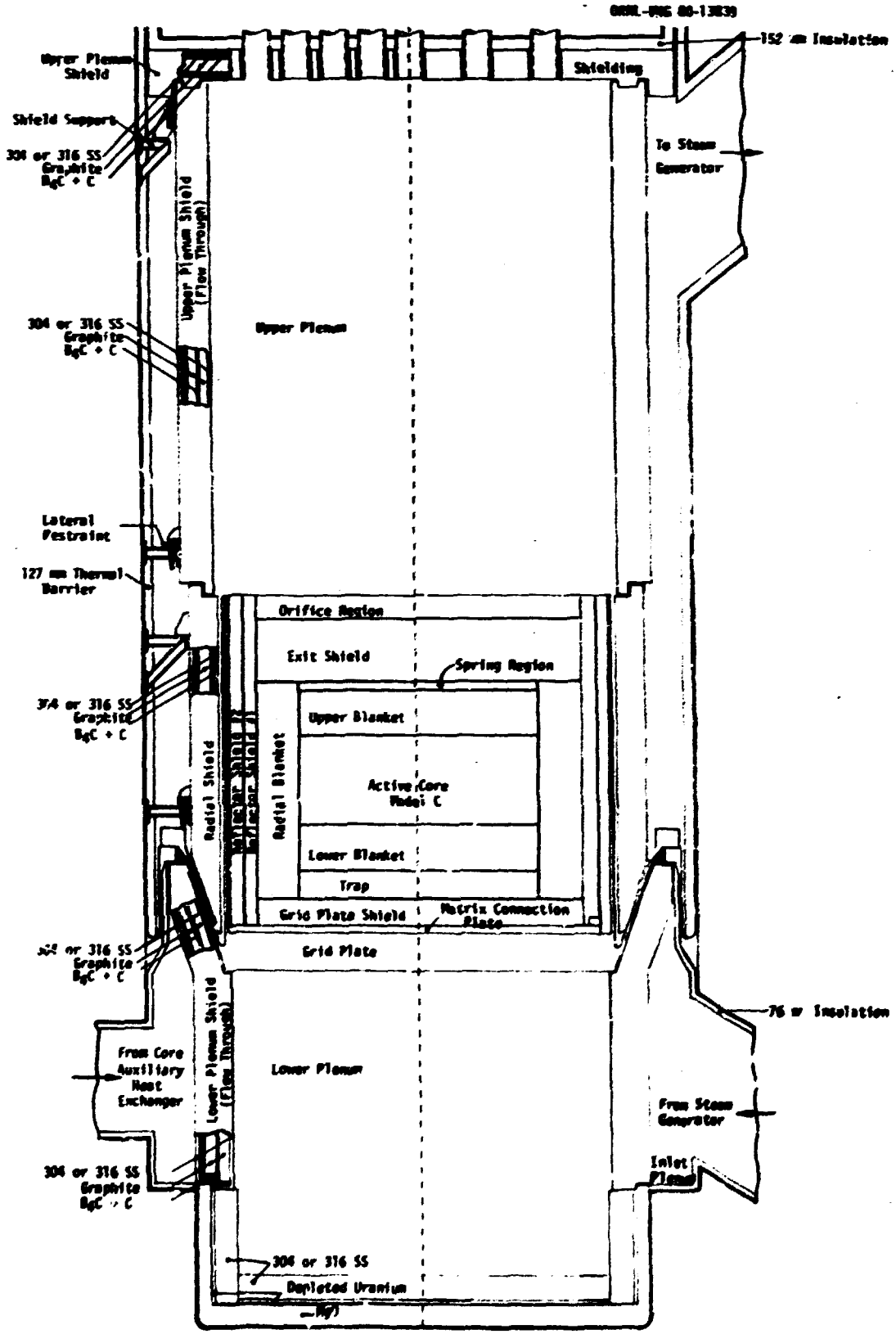

Fig. 2. Sketch of the GCFR Conceptual Shielding Configuration III design as used in the upper and lower plenum shield analyses.

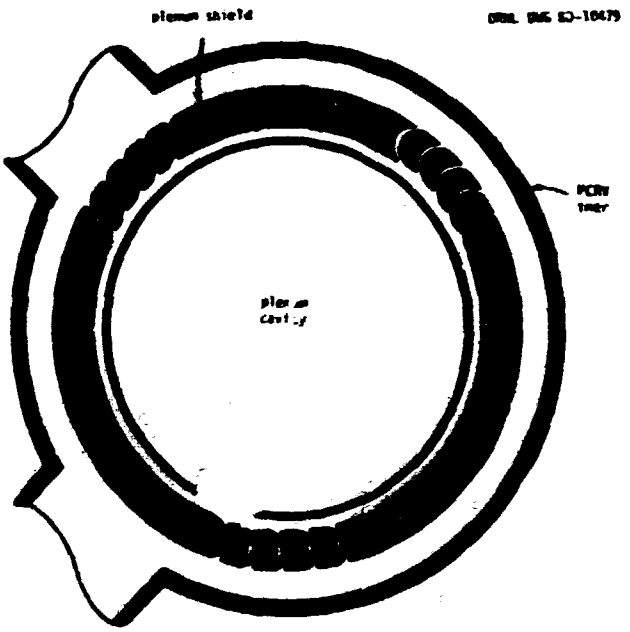

Fig. 3. Horizontal cut through reactor plenum showing flow through plenum shields concepts.

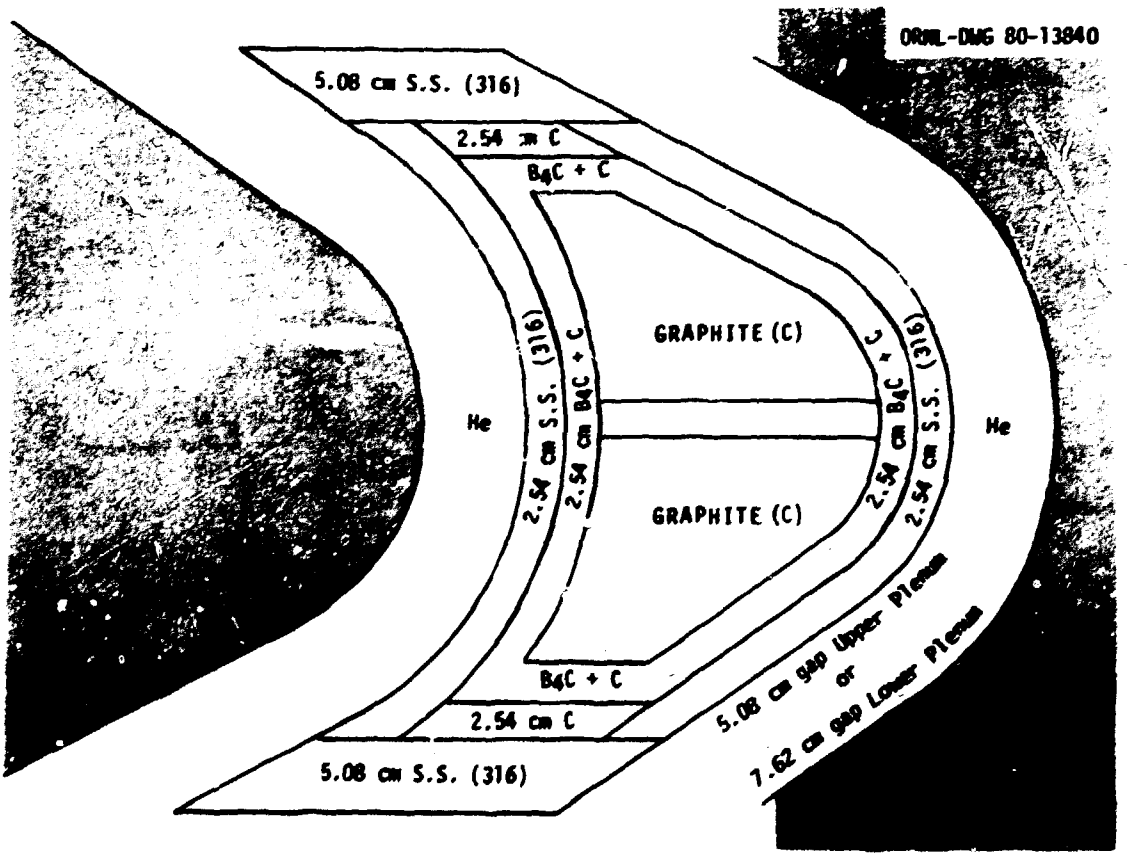

Fig. 4. Sketch of a segment of the chevron design flow-through shield concept.

3. DESIGN CONSTRAINTS ON RADIATION EXPOSURE

General Atomic Company has established several lifetime radiation exposure constraints for the permanent reactor components.[8] These are summarized in Fig. 5. The constraints based on residual ductility and nil ductility temperature shift depend on precise damage functions for relating neutron flux levels to the mechanical property change. Since there is large uncertainty in the damage functions, the residual ductility constraint in high temperature regions (T > 550°C) has been equated with a total neutron fluence limit of 10^{21} cm^{-2} and in moderate temperature regions (T < 550°C) with a neutron fluence limit of 10^{22} cm^{-2}. Likewise, the nil ductility temperature shift constraint has been equated with a total neutron fluence limit of 10^{19} cm^{-2}. Hence, the neutron fluence limit for all the structural steels with T > 550°C is 10^{21} cm^{-2}, but for lower temperatures (T < 550°C) the limit is 10^{22} cm^{-2}. For the PCRV liner, the PCRV concrete, rebar, cooling tubes, and tendons the fluence limit is 10^{19} cm^{-2}. An equivalent fission fluence for graphite damage (EFFGD) is used to specify the graphite fluence limit. Fluence limits were found to be 3.8×10^{22} cm^{-2} at 400°C, 3.5×10^{22} cm^{-2} at 600°C, and 1.4×10^{22} cm^{-2} at 800°C. ORNL uses graphite displacement cross sections supplied by General Atomic Company.

In addition to the above constraints for the permanent structures, there are constraints for the replaceable components which determine how often they should be replaced. In particular, the boronated graphite reflector-shield subassemblies will lose some of their shielding effectiveness due to burnup of the boron. The increased low-energy neutron flux transmitted could have some effect on the total fluence and the gamma-ray heating and dose in regions outside the reflector shields.

4. SOURCE CALCULATIONS

4.1 k-Calculation

To obtain a source for the shielding calculations, the distribution of the fission neutrons within the core and blankets was needed. The distribution was obtained with the DOT-IV[9] two-dimensional discrete ordinates transport computer code. Use was made of the model and atom

LIFETIME RADIATION EXPOSURE CRITERIA FOR PERMANENT COMPONENTS

ORNL DWG 80-10403

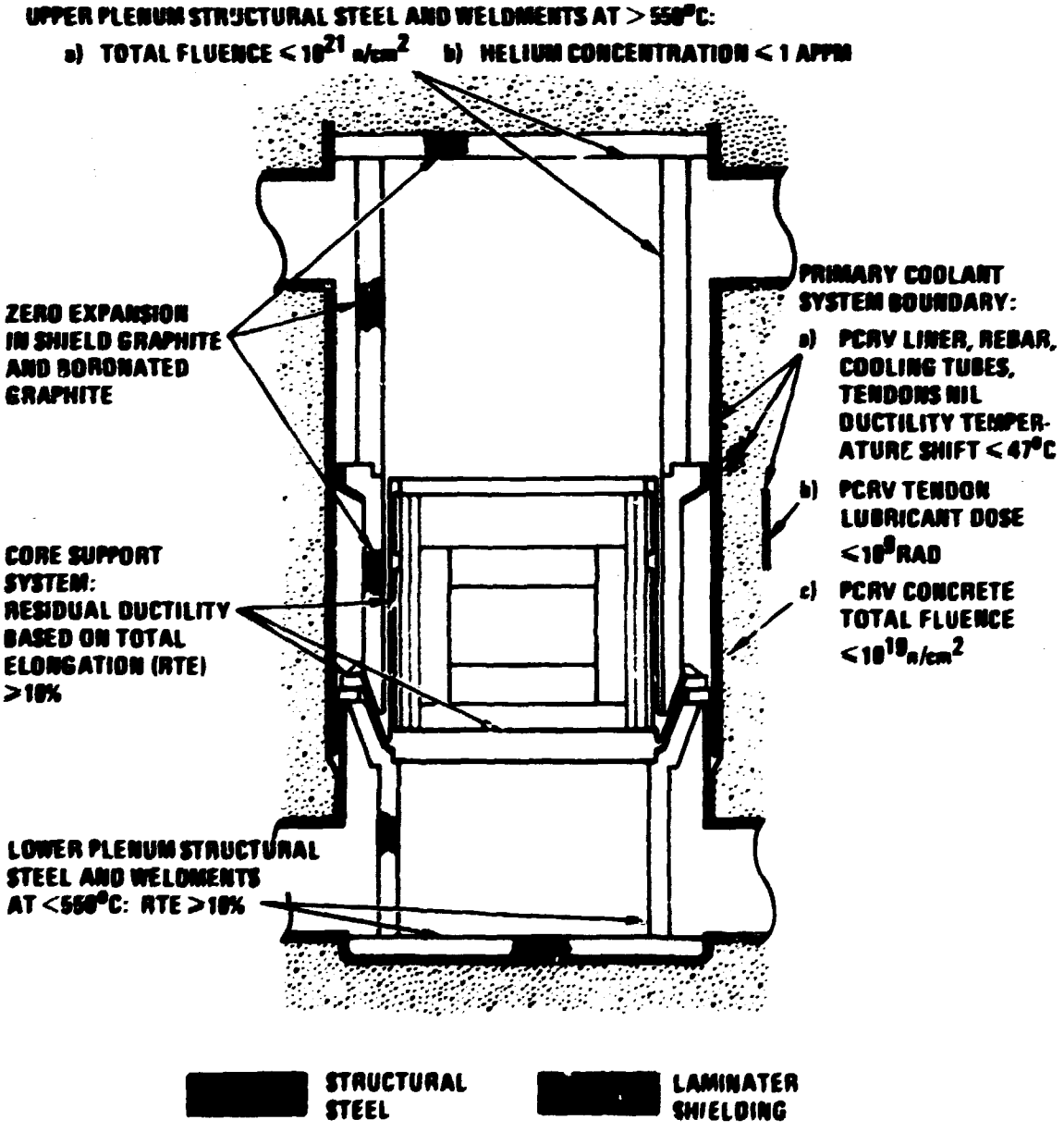

Fig. 5. Illustration of the lifetime radiation exposure constraints for permanent components of the upflow GCFR.

densities found in Ref. 2. In addition, the core and blanket regions were surrounded by the immediately adjacent regions for neutron reflection purposes. The calculation was performed with 51 neutron groups, first with diffusion theory until convergence and then S_4P_3 transport theory. An effective multiplication factor (k) of 1.05 was obtained.

4.2 Peripheral Boundary Source Calculations

4.2.1 Full Homogeneous Model

A fixed source calculation of a homogeneous mockup of the upflow GCFR mid-level regions (the portion of the GCFR located axially between the bottom of the grid plate and the top of the exit shield/orifice region) was performed to obtain flux levels in the mid-level regions and to obtain boundary sources to be input to peripheral shielding calculations. The calculation was performed with DOT-IV using 76 groups (51 neutron and 25 gamma-ray), S_8 quadrature (48 directions), and P_3 cross sections.* The fixed source for the calculation was obtained using the flux output from the k-calculation (sec. 4.1), the fission and fission production cross sections, spectra giving the fraction of neutrons per fission that emerge in a given group, and spectra giving the equilibrium number of fission-product gamma-rays per fission. The neutron source was obtained by multiplying the fission spectrum by the matrix obtained by folding the flux with the fission production cross section $\nu\Sigma_f$. The fission product gamma-ray source was obtained by multiplying the fission-product gamma-ray fission spectra by the matrix obtained by folding the flux with the fission cross section Σ_f. The fission spectrum for the neutrons was a ^{239}Pu spectrum while the gamma-ray spectra were generated using the ORIGEN[10] code. In generating the gamma-ray spectra, the energy per fission was forced to be 200 MeV. Examination of the source showed a total prompt neutron energy of 6.03 MeV/fission and a total fission-product gamma-ray energy of 3.66 MeV/fission. Glasstone and Edlund[11] showed for ^{235}U that fission-product gamma-rays, prompt neutrons, and prompt gamma-rays carried away 5, 6, and 6 MeV, respectively, from fission. Thus, the ORIGEN value for the fission-product gamma-ray energy appears low. A later calculation

*Macroscopic cross sections library prepared by L. R. Williams.

with a different nuclide library, which contained more fission-product data than the library used in the first calculation, showed results consistent with Glasstone and Edlund with less than a factor of 2.0 increase in the number of gamma rays per fission. As will be seen later, the increase in the source should have little effect on the calculated results obtained using the lower strength source.

The source was normalized using the reactor's thermal power (1076 MW), the number of fissions per unit fission source (0.36244), and a conversion factor of 3.2×10^{-11} watt-second per fission to give a normalization factor of 9.28×10^{19} s^{-1}. Since k = 1.05, a total neutron source of 9.76×10^{19} s^{-1} would be generated. The total fission-product gamma-ray source was 2.66×10^{20} s^{-1}.

Peripheral boundary sources were output at the outside of the outer row of reflector shields, at the top of the exit shield/orifice region for upper plenum analysis, and at the bottom of the grid plate for lower plenum analysis. Streaming correction factors were applied to the sources for the peripheral shielding calculations.

4.2.2 Correction for Axial streaming

To correct the peripheral boundary sources for axial streaming, heterogeneous axial cell calculations were performed on the central fuel subassembly. The cells were reflected at the core midplane and on the left and right sides. The calculations were done using 76 groups, S_{12} quadrature (96 directions), and P_3 cross sections. The source for the calculation was a fission source which included both prompt neutrons and fission-product gamma rays. The source was obtained as described under section 4.2.1. The streaming correction factors were obtained by comparing the leakages from the heterogeneous cells with those from equivalent homogeneous cells from the full homogeneous mockup (section 4.2.1). The streaming correction factors were quite large. For neutrons they ranged from 7.5 to 76 for the upper plenum and from 20 to 530 for the lower plenum. Factors for gamma-rays ranged from 8.3 to 194 for the upper plenum and from 34 to 2210 for the lower plenum. Correction factors averaged over neutron and gamma-ray groups amounted to 21.5

for the upper plenum and 35.1 for the lower plenum. The ORNL/TSF exit shield experiment should determine the reasonableness of the heterogeneous calculation results.

Isoplots of the 24 full-power-year neutron fluence within the cells are shown in Figs. 6 and 7 for the upper and lower cells, respectively. The maximum neutron fluence at the exit of the upper cell is about 1.8 x 10^{20} cm^{-2} while the maximum at the exit of the lower cell is about 3.6 x 10^{20} cm^{-2}. Fig. 7 also shows a maximum neutron fluence in the grid plate of about 7 x 10^{21} cm^{-2}. (The top 10 cm of the region shown as the grid plate is known as the PES Plate and contains connections for the pressure equilization system.) The maximum fluence level in the grid plate is only about 30% below the fluence limit for stainless steel support structures in regions with temperatures less than 550°C. If, as before,[1] an experimental bias factor is applied to the calculated peak fluence in the grid plate to account for the sharpness of the peak over the interassembly gap, the maximum fluence might approach 9 x 10^{21} cm^{-2}, just 10% below the limit.

4.2.3 Correction for Radial Streaming

Radial streaming from the core is expected to occur mainly in the gaps between subassemblies. Also it was theorized that streaming would be significant only in regions beyond the core since the localized fission sources in the core mask the effects of streaming. Thus, a representative cell was carved out of the subassemblies comprising the second and third rows of the radial blanket and the two reflector shield rows. The cell is illustrated in Fig. 8.

The representative cell from Fig. 8 was converted to a two-dimensional X-Y mockup for use in a DOT calculation. The cell was modeled in both heterogeneous and homogeneous geometries with the Y-axis being the longer dimension of the cell. A fission source was included for the portion of the blanket within the cell, and an external boundary source was placed on the Y = 0.0 cm boundary to account for the net leakage across the center of radial blanket row 2. The calculations were performed using 76 groups, S_{12} symmetric quadrature (96 directions), and P_3 cross sections.

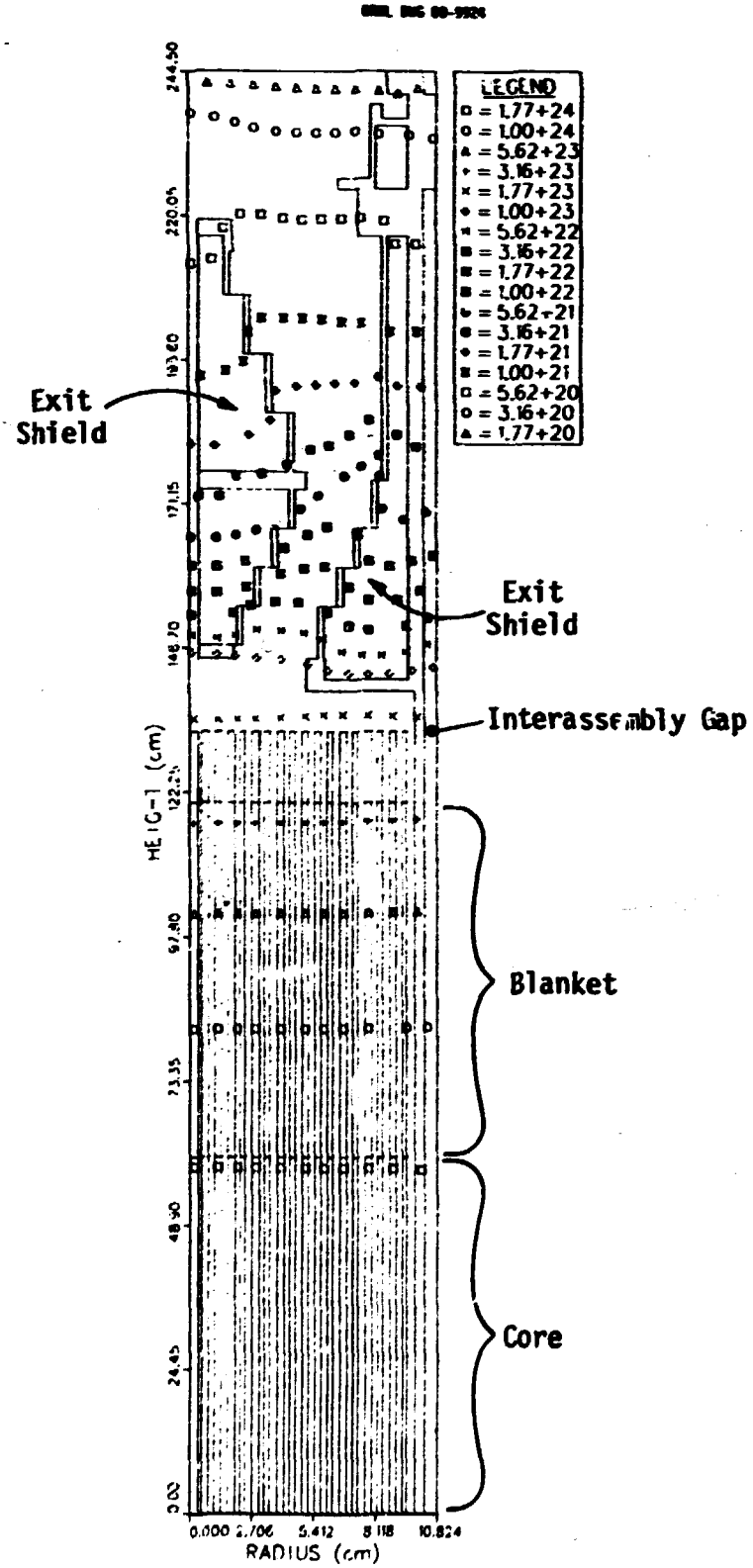

Fig. 6. Isoplot of the 24 full-power-year total neutron fluence in a heterogeneous cell mockup of the Upflow GCFR upper core regions.

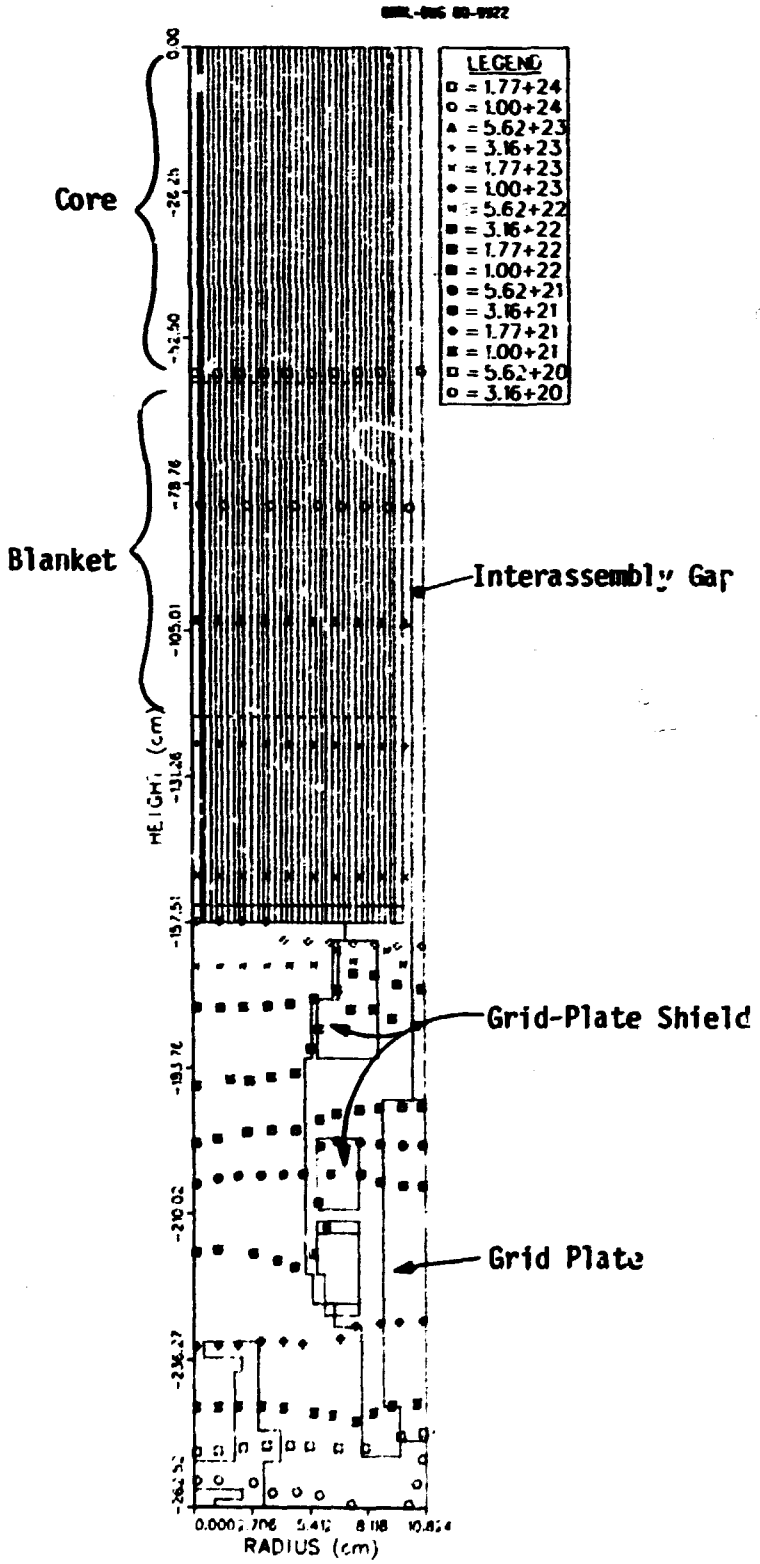

Fig. 7. Isoplot of the 24 full-power-year total neutron fluence in a heterogeneous cell mockup of the Upflow GCFR lower core regions.

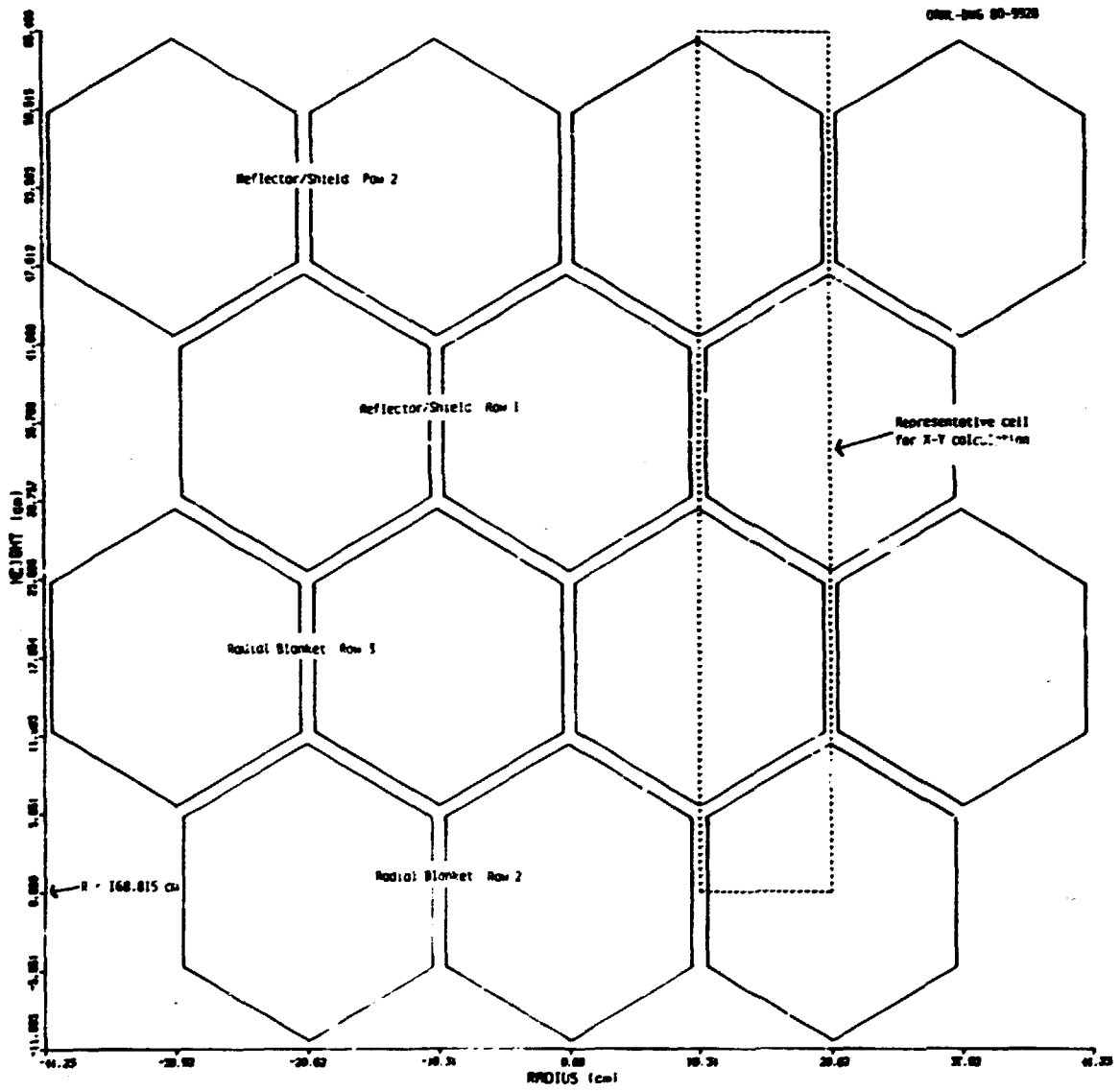

Fig. 8. Layout of a portion of the radial blanket and reflector shield regions showing a representative cell for an X-Y radial calculation.

Figures 9 and 10 show isoplots of the total 24 full-power-year neutron fluence within the heterogeneous and homogeneous cells, respectively. The heterogeneous calculation shows jumps in the flux where interassembly gaps are encountered, whereas the homogeneous calculation shows smoother flux curves at the subassembly interfaces. The fluence at the outer boundary of the reflector shields is nearly the same for both cases. There are, however, some large streaming corrections within certain energy ranges. For neutron energies above 0.1 MeV, the correction

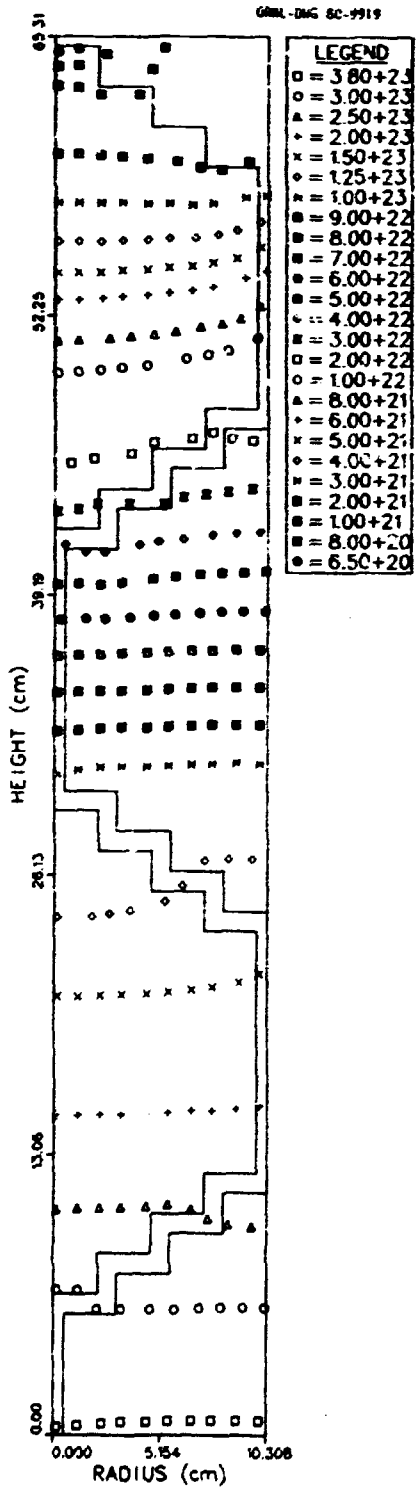

Fig. 9. Isoplot of the 24 full-power-year total neutron fluence in an X-Y heterogeneous cell mockup of the Upflow GCFR radial regions.

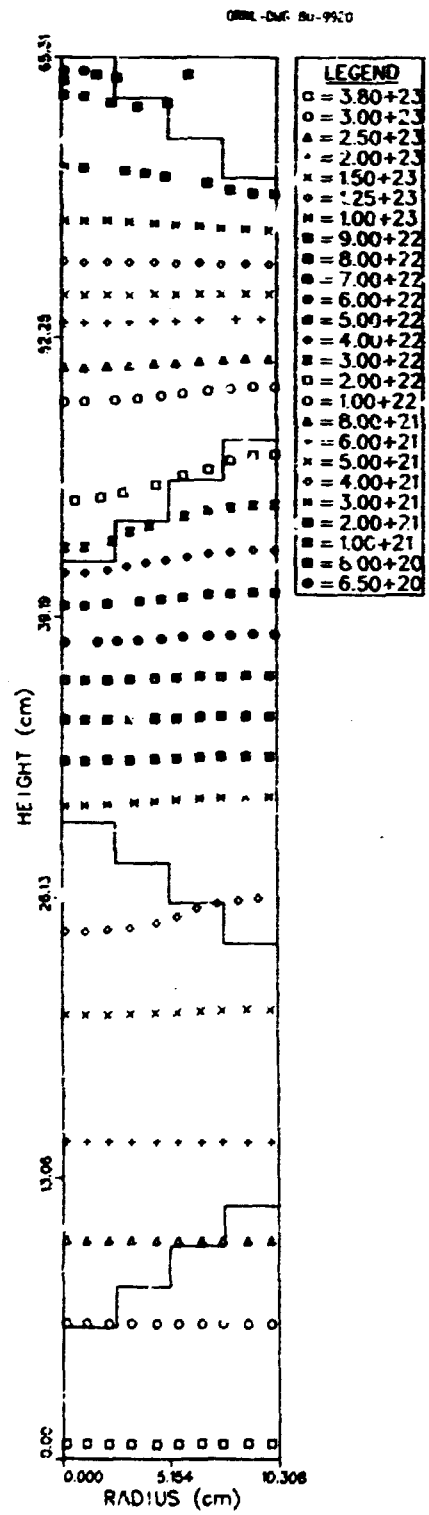

Fig. 10. Isoplot of the 24 full-power-year total neutron fluence in an X-Y homogeneous cell mockup of the Upflow GCFR radial regions.

factors range from 1.025 to 1.083. For intermediate neutron energies (2.38 eV < E < 0.1 MeV), the correction factors range from 1.088 to 216.2. In the thermal neutron energy range, the correction factors increase drastically, ranging from 2.39×10^3 to 6.84×10^6. For gamma rays, the correction factors range from 1.004 to 1.161, with the most important groups having correction factors of 1.05 or less. The maximum fluence along the top edge of the plot is 1.26×10^{21} cm^{-2} for the heterogeneous case (Fig. 9) and 1.07×10^{21} cm^{-2} for the homogeneous case (Fig. 10). The core barrel, which lies just outside the reflector shield region, might see a fluence on the order of 1.2×10^{21} cm^{-2}. As stated before, since the core barrel will be cooled with inlet plenum gas, the 10^{22} cm^{-2} neutron fluence limit rather than the 10^{21} cm^{-2} limit applies. Considerable margin is thus available for calculational uncertainty.

5. SHIELDING CALCULATIONS

5.1 Mid-Level Regions

Much of the shielding calculation for the mid-level regions was performed during the source calculation described under section 4.2.1. Also the cell streaming calculations under sections 4.2.2 and 4.2.3 may be considered mid-level region calculations. An additional calculation was performed for the mid-level radial regions outside the reflector shields to include the effects of radial streaming of radiation in the interassembly gaps. The full geometry calculations were performed with DOT-IV using 76 groups, S_8 symmetric quadrature (48 directions), and P_3 cross sections.

The two-dimensional mockup for the mid-level regions is shown in Fig. 11. As stated in section 2, the mockup was based on the shielding design shown in Fig. 1. Shown in Fig. 12 superimposed on a similar drawing are isocontours of the total 24 full-power-year neutron fluence, starting at 10^{24} cm^{-2} near the core center and ending at 10^{13} cm^{-2} in the PCRV. With respect to the radiation constraints, it shows only that the fluence in the core barrel would be borderline at about 10^{21} cm^{-2}

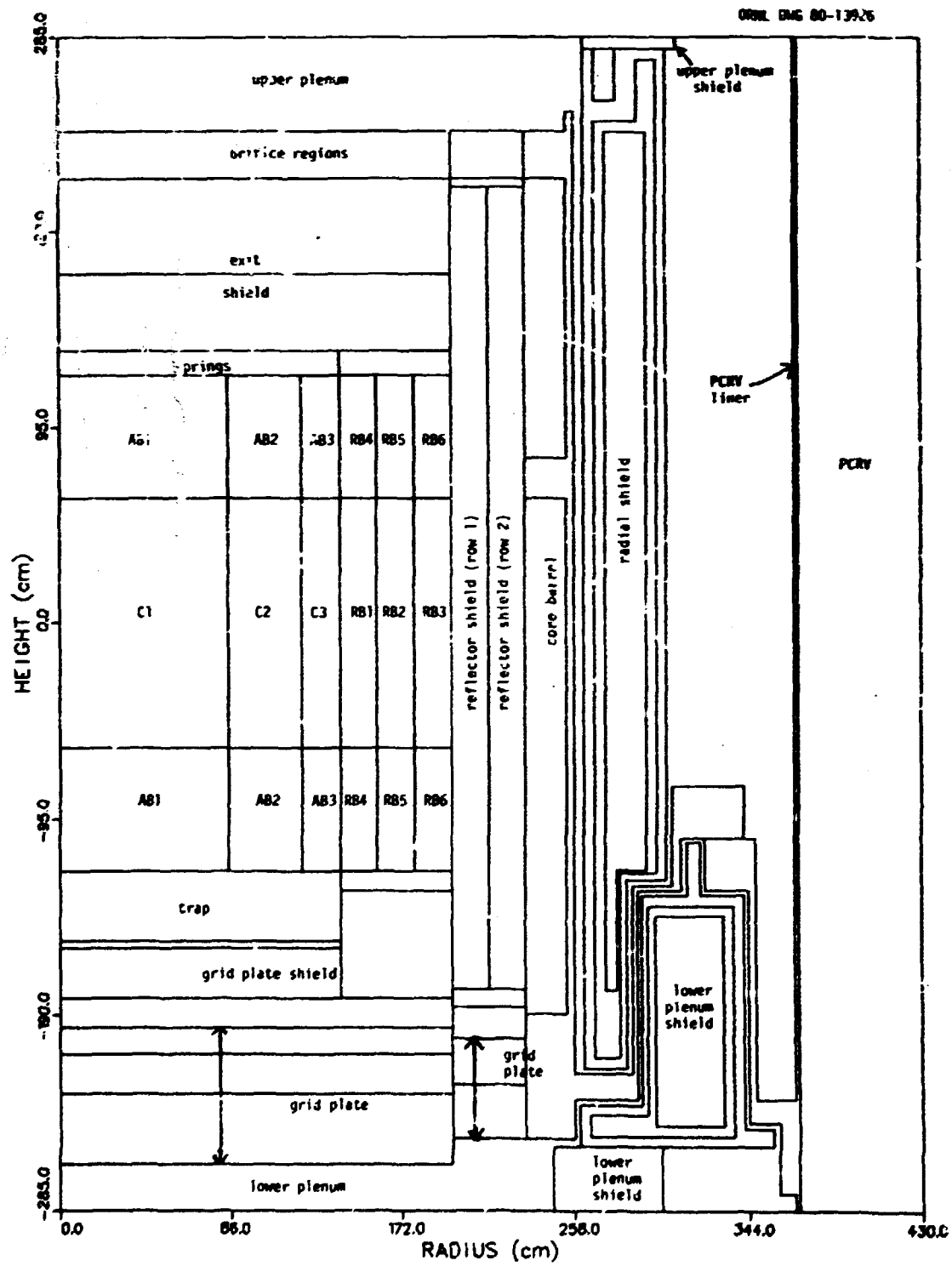

Fig. 11. Plot of the 2-D zone layout for the Conceptual Upflow GCFR mid-level region calculation.

unless the core barrel is cooled by inlet plenum gas, allowing a fluence limit of 10^{22} cm^{-2}. The fluence in the liner is well below the 10^{19} cm^{-2} constraint. While the fluence in the core barrel as shown in Fig. 12 is barely below the 10^{21} cm^{-2} high temperature (T > 550°C) constraint, neutron streaming effects push the fluence about 15% above the constraint at the core midplane. The neutron fluence isoplot for the mid-level radial regions beyond the reflector-shield region is shown in Fig. 13. These results include the effects of radial radiation streaming. The portion of the core barrel where the high temperature constraint is exceeded extends from about 30 cm below the core midplane to 30 cm above it. The high values near the grid plate (height = -190 cm) are due to larger streaming correction factors for thermal neutrons in that region and are probably not real since the streaming correction factors were determined for the core mid-plane and are not particularly valid for thermal neutrons streaming in boronated regions not of similar makeup

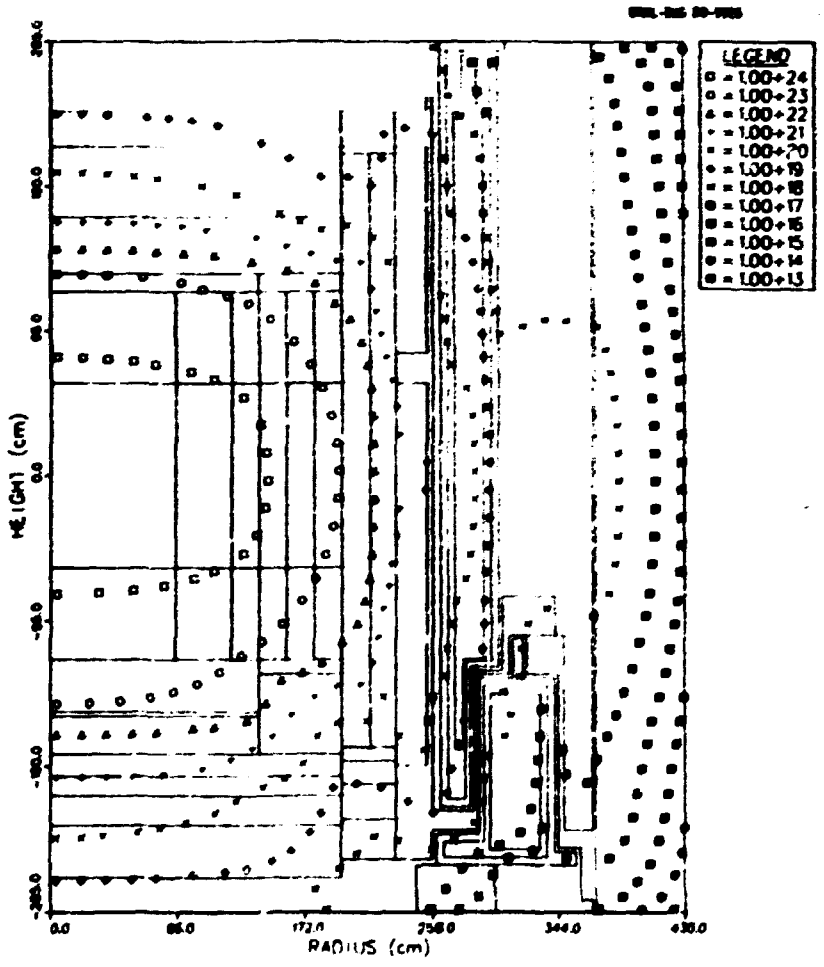

Fig. 12. Isoplot of the 24 full-power-year total neutron fluence (cm^{-2}) in the mid-level regions of the upflow GCFR.

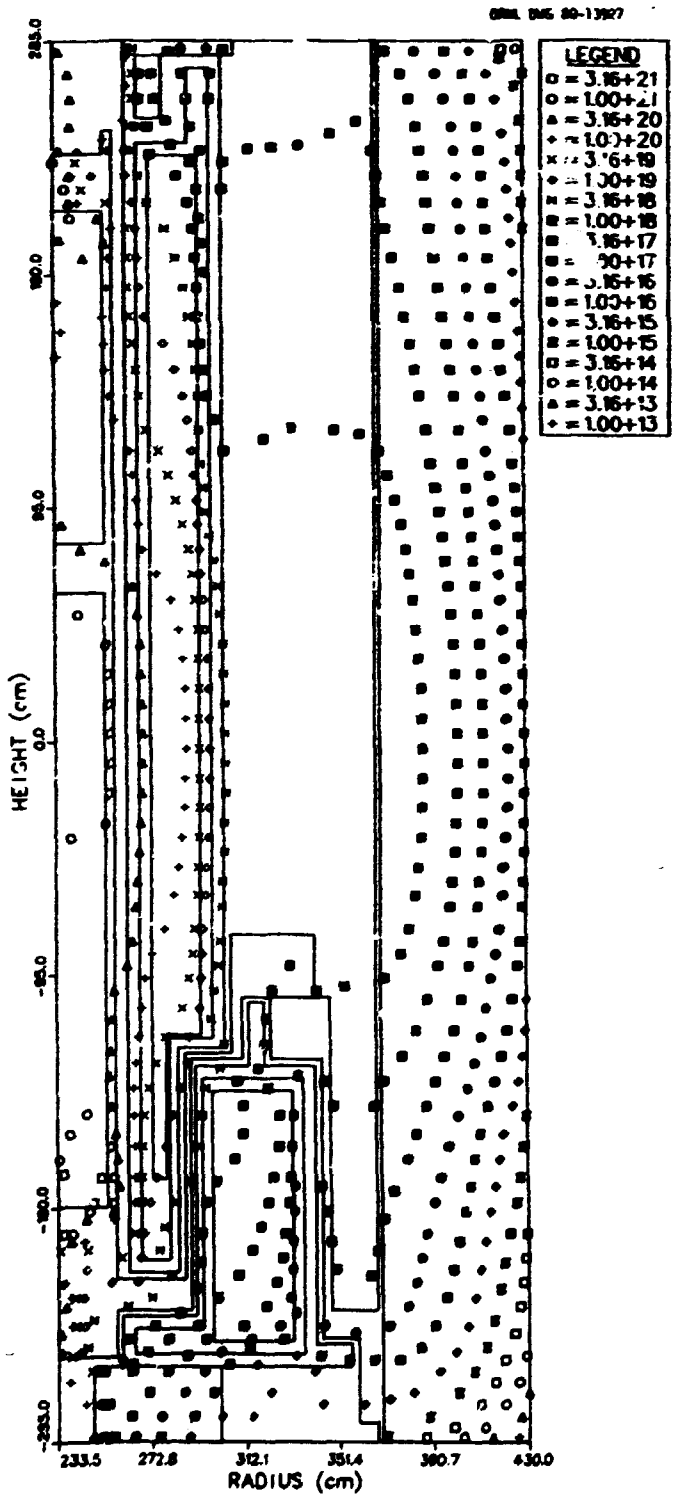

Fig. 13. Isoplot of the streaming-corrected 24 full-power-year total neutron fluence (cm^{-2}) in the Conceptual Upflow GCFR mid-level radial regions.

as the core midplane. The maximum fluence in the PCRV liner is 2.47 x 10^{18} cm^{-2} (a factor of 4 below the constraint) up from the 2.03 x 10^{18} cm^{-2} (a factor of 5 below the constraint) obtained before correction for radial streaming. The effect of radiation streaming through gaps in the radial shield are to be obtained from the ORNL/TSF Shield Heterogeneity Experiment. The effect is not expected to be a factor of 4.

The 24 full-power-year tissue dose for mid-level regions beyond the reflector-shield region is shown in Fig. 14. It is seen from the figure that the 10^9 rd constraint on the dose to the lubricant for the innermost vertical tendon, which is located 45.7 cm from the liner (or near R = 415 cm) has not been exceeded. As a matter of fact, the maximum dose to the tendon lubricant is a factor of 8 below the constraint. Since the lubricant was not tissue, several organic lubricants were studied to determine the degree of difference between the tissue response and that of an organic lubricant. The flux spectrum at the tendon position was folded with the kerma factors for the several lubricants, and it was found that the kerma doses differed by at most 11%, with the tissue kerma dose always being higher. For this particular spectrum, the tissue kerma dose was about 65% of the total dose. Thus, the use of the tissue dose response function factors a reasonable amount of conservatism into the tendon lubricant dose. The lubricants examined were chosen to be representative of the Visconorust 2889 lubricant selected by GAC.[12] Visconorust 2889 is a product of the Viscosity Oil Company of Chicago, and its composition is considered proprietary.

The effect of including fission-product gamma rays in the calculation was examined by comparing the gamma-ray heating rates in stainless steel 316. Figures 15 and 16, respectively, show plots of the total and the fission-product gamma-ray heating in SS316. It is seen that the fission product gamma-ray heating is only 10% of the total in the core and is negligible in the core barrel and beyond. Thus, a factor of two increase in the fission-product gamma-ray source, as indicated in section 4.2.1, should not have a great impact on the shield design.

The Equivalent Fission Fluence for Graphite Damage (EFFGD) is plotted in Fig. 17. The EFFGD is well below the minimum constraint in all graphite regions, being greater than a factor of 100 below it in the radial shield.

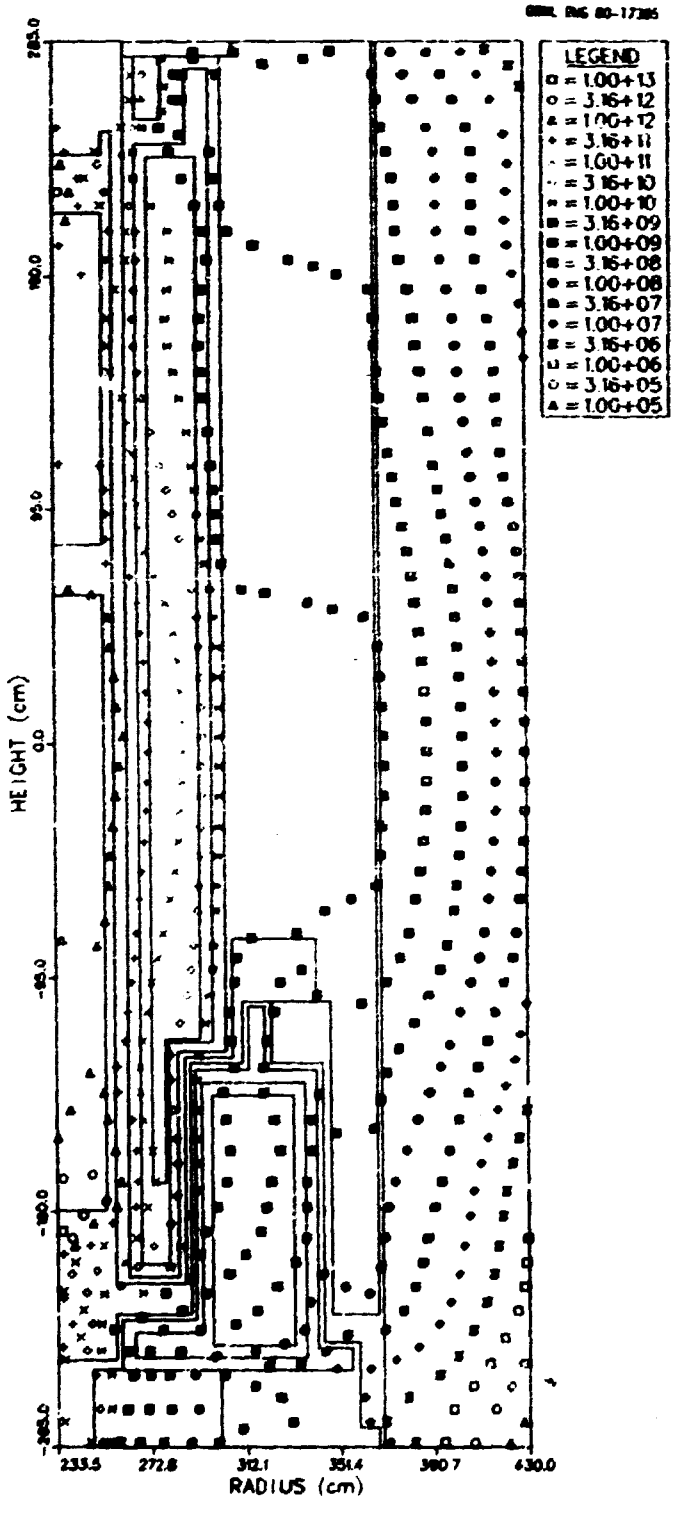

Fig. 14. Isoplot of the streaming-corrected 24 full-power-year total tissue dose (rd) in the Conceptual Upflow GCFR mid-level radial regions.

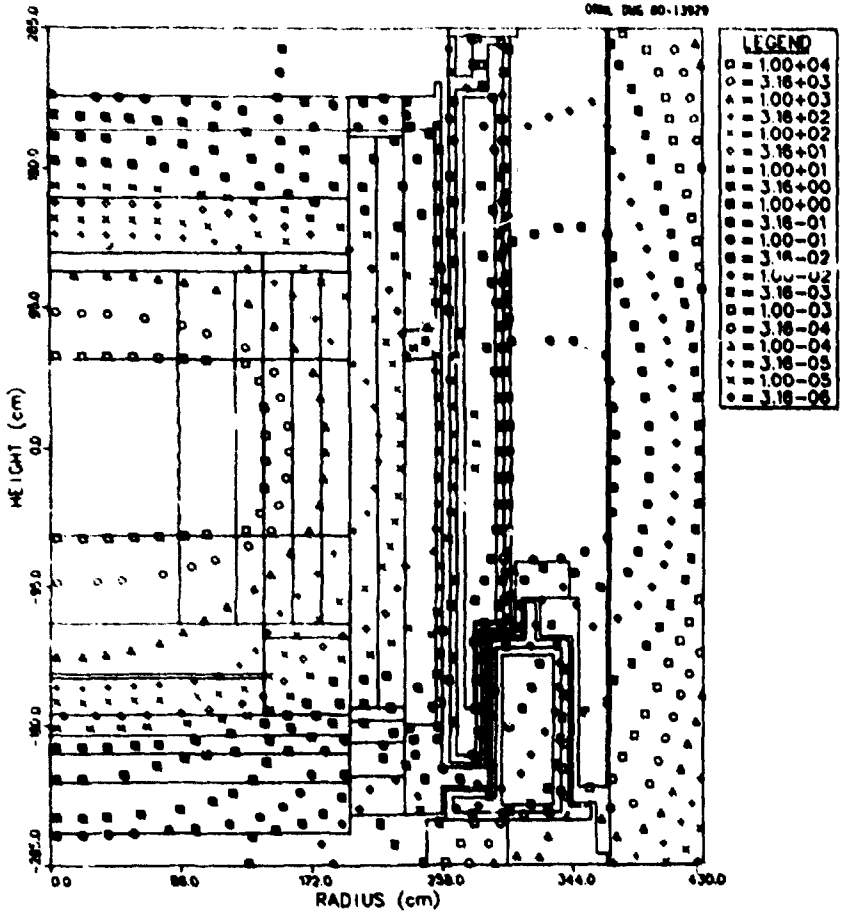

Fig. 15. Isoplot of the total gamma-ray heating (mW/cm^3) in SS316 in the Conceptual Upflow GCFR mid-level regions.

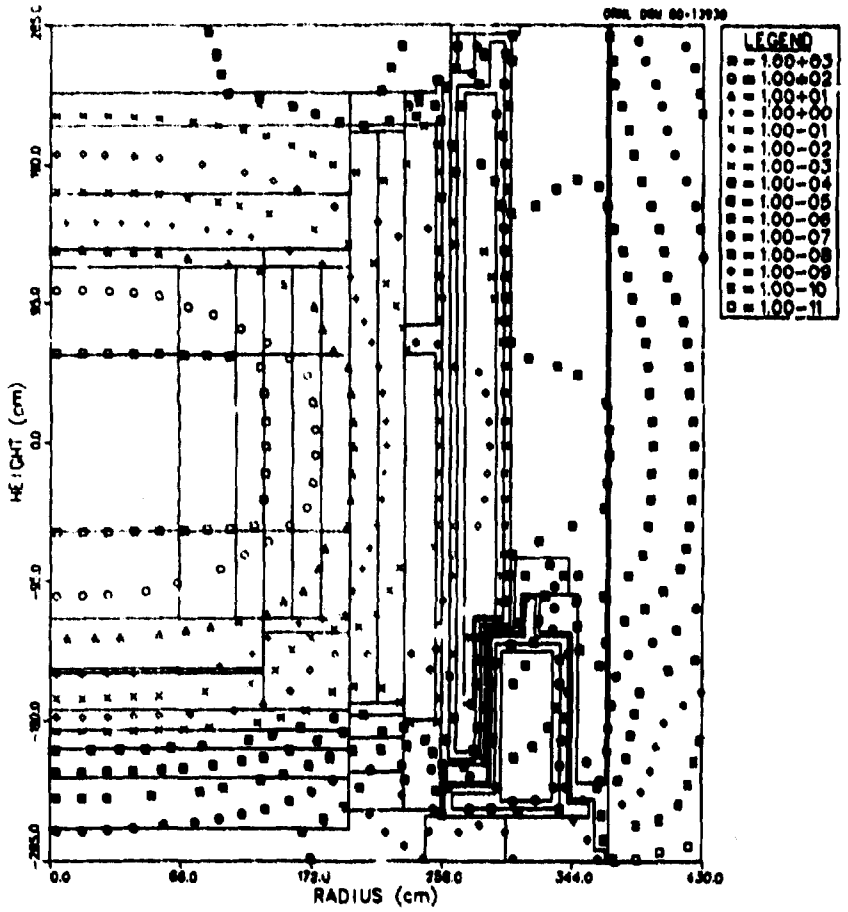

Fig. 16. Isoplot of the heating (mW/cm^3) in SS316 in the Conceptual Upflow GCFR mid-level regions due to fission product gamma-rays.

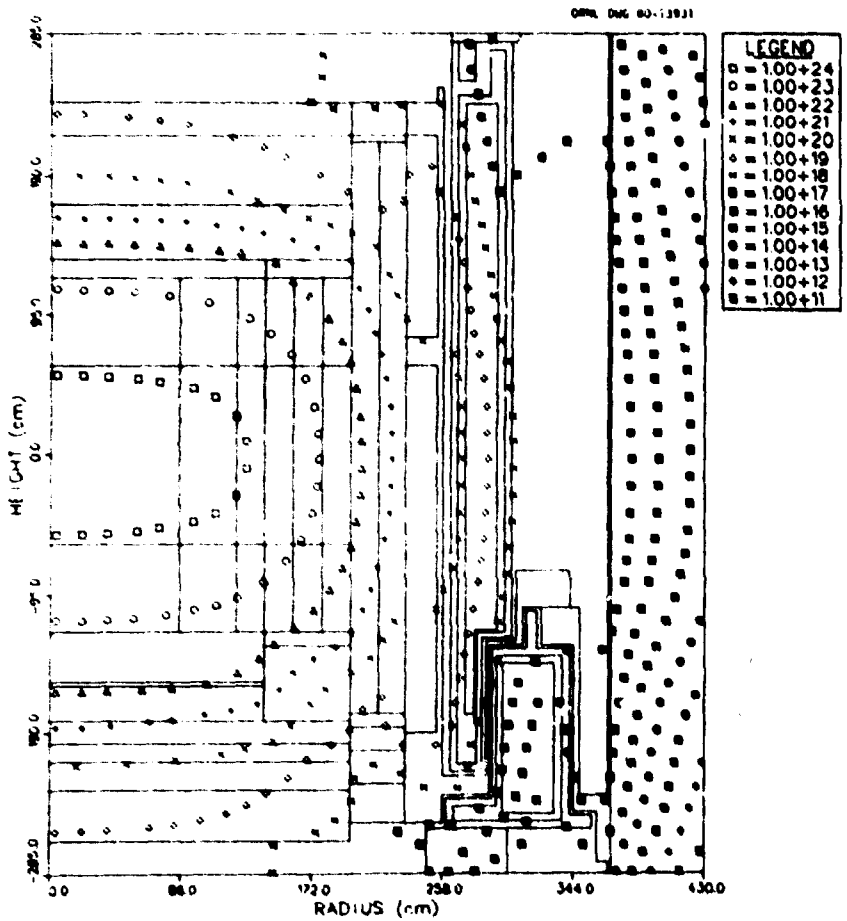

Fig. 17. Isoplot of the equivalent fission fluence for graphite damage (cm^{-2}) in the Conceptual Upflow GCFR mid-level regions.

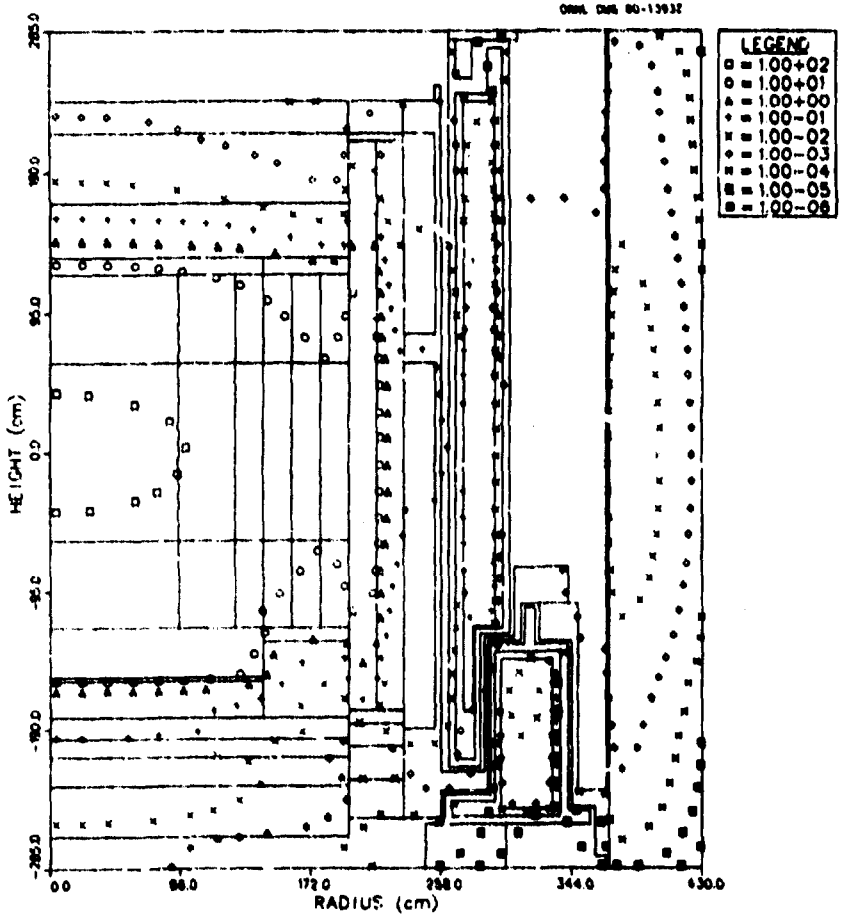

Fig. 18. Isoplot of the annual percent absorption of B^{10} in the Conceptual Upflow GCFR mid-level regions.

The rate at which B^{10} is burned out by neutron absorption in percent of initial concentration per year is shown in Fig. 18 for the full geometry mockup and in Fig. 19 for a radial cell mockup of the upflow GCFR mid-level regions. The results assumed the rate of burnup was proportional to the initial concentration rather than the concentration at a given time. The results are reasonably exact for curves showing burnups of 10% per year or less. The 100% per year burnup calculated based on the first assumption corresponds to only about 63% per year burnup based on the second, more correct assumption. The B^{10} absorption was averaged over the C + B_4C reflector shield region of Fig. 19 leading to an average burnup of 1.74% per year. Figure 19 indicates that the B^{10} burns out of the reflector shield at rates of 0.1% to 21.5% per year. The 21.5% per year burnup in Fig. 19 actually corresponds to a burnup of 19.3% per year. Nevertheless, the burnup can be quite significant over portions of the reflector shield. Because of the burnup of B^{10}, the shield will lose some of its effectiveness against low energy neutrons. Thus, as determined by sensitivity analysis in a previous study,[1] the radiation levels in the PCRV and liner will increase as a result. While an average 2% per year burnup may not result in significant increases in those radiation levels, burnups averaging greater than 5% per year should give rise to noticeable increases in the radiation levels in the PCRV and liner. The previous sensitivity case indicated that a 1% decrease in the B^{10} concentration in the reflector shield would result in a 2.84% increase in the neutron flux in the PCRV liner. With this same sensitivity, the average yearly burnup of 1.74% in the reflector shield would result in a 4.94% increase yearly in the neutron flux in the liner. The increase is small when compared to the factor of 4 margin between the maximum fluence in the liner and the design constraint.

Helium production at various points in the mid-level regions was calculated for threshold and full-energy range (n,α) reactions in naturally occurring and transmuted components of stainless steel 316. An initial B^{10} concentration of five atomic parts per million was assumed for SS316. The points at which the helium production was calculated are shown on a 2-D plot of the mid-level regions in Fig. 20. The helium production at the points numbered as shown in Fig. 20 is

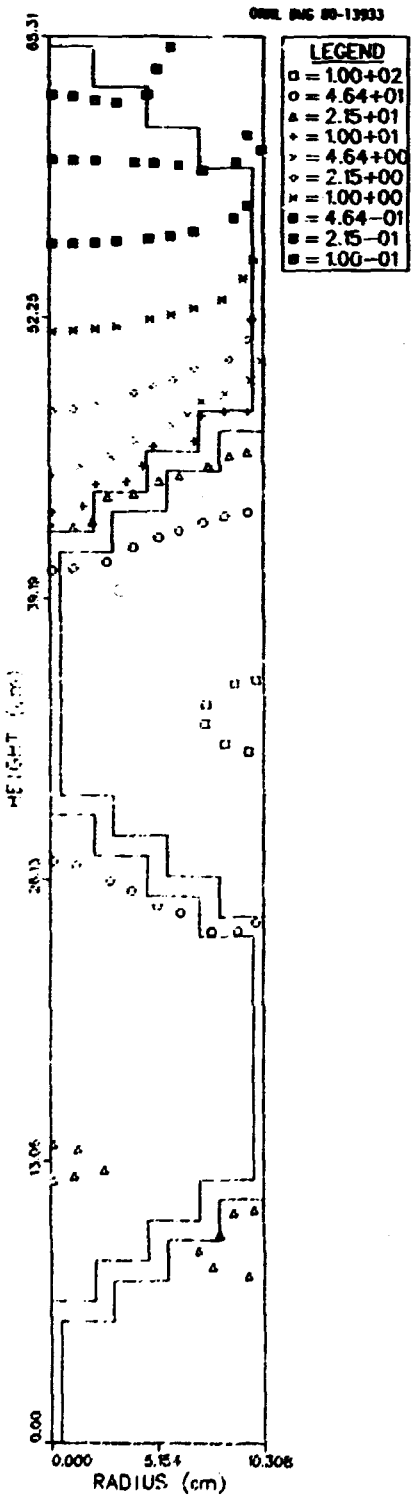

Fig. 19. Isoplot of the X-Y cell calculated annual percent absorption of B^{10} at the core mid-plane of the Conceptual Upflow GCFR mid-level regions.

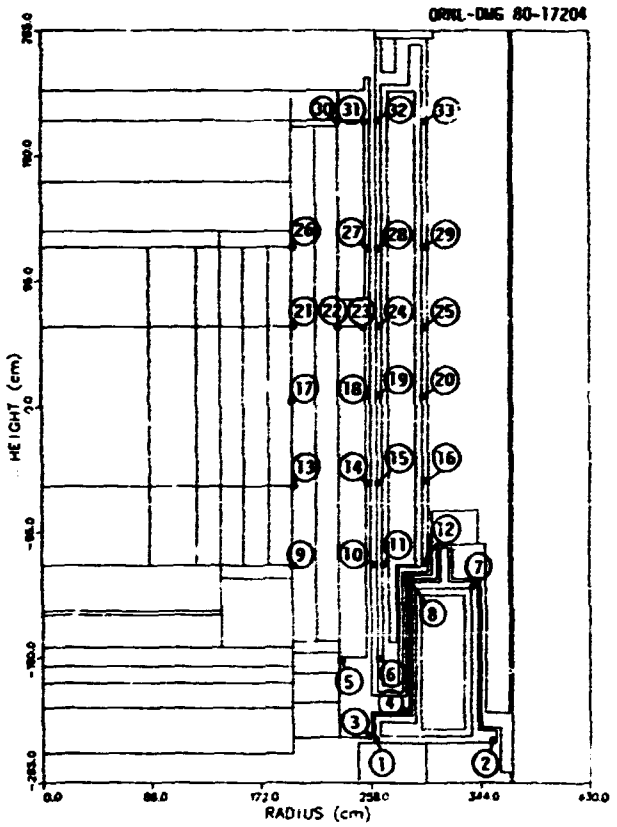

Fig. 20. Locations of points in the Conceptual Upflow GCFR mid-level regions at which helium production was calculated.

shown in Table 1 for seven time periods in effective full-power-years (EFPY). These times range from 3 to 150 EPFY's. The constraint placed on the helium production (see Fig. 5) was that the helium concentrations in upper plenum structural steels should be less than 1 atomic part per million (APPM). As seen from Table 1, since the helium production at points near the upper plenum (points 30-33) is well below 1 APPM, the helium concentration in the upper plenum structural steels should also be well below the 1 APPM constraint over the expected 24-EFPY lifetime of the reactor. The core subassembly and reflector shield assembly duct walls, on the other hand, would experience helium concentrations above 1 APPM since values at the reflector shield/blanket interface (points 13, 17, and 21) are above 1 APPM after 3 EFPY's. Since the fuel cycle length is 381 full-power-days and each subassembly on the average resides in the core for 3 full cycles[13] (blanket subassemblies remain 6 full cycles or longer), the core subassemblies can be expected to experience

Table 1. Helium Concentration* (Atomic Parts per Million) at Various Locations in the Conceptual Upflow GCFR Mid-Level Regions

Position	Time (effective full-power years)						
	3	6	9	30	60	90	150
1	2.58241E-06	5.16482E-06	7.74723E-06	2.58241E-05	5.16483E-05	7.74726E-05	1.29121E-04
2	8.26075E-08	1.65215E-07	2.47823E-07	8.26076E-07	1.65215E-06	2.47823E-06	4.13038E-06
3	3.93900E-06	7.87600E-06	1.18140E-05	3.93900E-05	7.87602E-05	1.18140E-04	1.96901E-04
4	3.06837E-07	6.13674E-07	9.20511E-07	3.06837E-06	6.13674E-06	9.20512E-06	1.53419E-05
5	6.37443E-04	1.27493E-03	1.91247E-03	6.37656E-03	1.27579E-02	1.91439E-02	3.19303E-02
6	2.77252E-04	5.54512E-04	8.31778E-04	2.77283E-03	5.54634E-03	8.32054E-03	1.38710E-02
7	1.08867E-06	2.17733E-06	3.26600E-06	1.08867E-05	2.17733E-05	3.26599E-05	5.44332E-05
8	6.19593E-05	1.23919E-04	1.85879E-04	6.19605E-04	1.23924E-03	1.85890E-03	3.09830E-03
9	1.81909E-01	3.60746E-01	5.36717E-01	1.70411E 00	3.25640E 00	4.78041E 00	8.04152E 00
10	1.23621E-03	2.47257E-03	3.70910E-03	1.23692E-02	2.47544E-02	3.71555E-02	6.20057E-02
11	8.89148E-04	1.77839E-03	2.66772E-03	8.89562E-03	1.78004E-02	2.67145E-02	4.45702E-02
12	1.70288E-05	3.40576E-05	5.10865E-05	1.70289E-04	3.40579E-04	5.10872E-04	8.51463E-04
13	1.18449E 00	2.29912E 00	3.35812E 00	1.18291E 01	3.03462E 01	5.58032E 01	1.19749E 02
14	3.81828E-03	7.63772E-03	1.14583E-02	3.82356E-02	7.65887E-02	1.15060E-01	1.92357E-01
15	2.58502E-03	5.17072E-03	7.75710E-03	2.58808E-02	5.18298E-02	7.78469E-02	1.30086E-01
16	5.56427E-05	1.11285E-04	1.66928E-04	5.56416E-04	1.11281E-03	1.66918E-03	2.78184E-03
17	1.93295E 00	3.73884E 00	5.57280E 00	2.37573E 01	6.67348E 01	1.21877E 02	2.47455E 02
18	5.67328E-03	1.13490E-02	1.70272E-02	5.68434E-02	1.13933E-01	1.71270E-01	2.86691E-01
19	3.78355E-03	7.56850E-03	1.13549E-02	3.78990E-02	7.59394E-02	1.14122E-01	1.90913E-01
20	7.11394E-05	1.42276E-04	2.13414E-04	7.11368E-04	1.42270E-03	2.13400E-03	3.55640E-03
21	1.07541E 00	2.07910E 00	3.04544E 00	1.04005E 01	2.59501E 01	4.74592E 01	1.02477E 02
22	4.55158E-03	9.10507E-03	1.36605E-02	4.56019E-02	9.13954E-02	1.37382E-01	2.29934E-01
23	3.53236E-03	7.06593E-03	1.06007E-02	3.53781E-02	7.08779E-02	1.06500E-01	1.78112E-01
24	2.26446E-03	4.52940E-03	6.79493E-03	2.26664E-02	4.53814E-02	6.81452E-02	1.13820E-01
25	4.92451E-05	9.84900E-05	1.47735E-04	4.92441E-04	9.84859E-04	1.47725E-03	2.46198E-03
26	2.10829E-01	4.17473E-01	6.20255E-01	1.95579E 00	3.72806E 00	5.49409E 00	9.40043E 00
27	8.69281E-04	1.73962E-03	2.60802E-03	8.69548E-03	1.73969E-02	2.61043E-02	4.35368E-02
28	6.02178E-04	1.20439E-03	1.80664E-03	6.02333E-03	1.20501E-02	1.80804E-02	3.01512E-02
29	2.76796E-05	5.53591E-05	9.30385E-05	2.76792E-04	5.53573E-04	8.30346E-04	1.38386E-03
30	1.61293E-04	3.22590E-04	4.83889E-04	1.61307E-03	3.22648E-03	4.84014E-03	8.06844E-03
31	1.49192E-04	2.98386E-04	4.47584E-04	1.49202E-03	2.98426E-03	4.47672E-03	7.46231E-03
32	8.02799E-05	1.60560E-04	2.40841E-04	8.02826E-04	1.60571E-03	2.40866E-03	4.01475E-03
33	1.00054E-05	2.00107E-05	3.00160E-05	1.00053E-04	2.00104E-04	3.00154E-04	5.00249E-04

*Due to threshold and (n,α) reactions in SS316 elemental components and (n,α) reactions through the transmutation of Ni^{58}. The initial B^{10} concentration in SS316 was assumed to be 5 atomic parts per million.

helium concentrations above 1 APPM during their residence in the reactor. The coolant temperature range through the core is expected to be 300-550°C.

Isoplots of additional activities for the mid-level regions are given in Appendix A.

It was mentioned earlier that the model for the mid-level region calculation was based on the GCFR shielding design shown in Fig. 1. In this design, the radial shield consisted of a 20.32-cm-thick graphite layer sandwiched between 5.08-cm-thick layers of boronated graphite and stainless steel. In the design of Fig. 2, the boronated graphite layer has been subdivided into an outer 2.54-cm-thick layer of graphite surrounding a 2.54-cm-thick layer of boronated graphite. The effects on radiation levels in the PCRV and liner due to the change to the new design were estimated using 1-D cylindrical ANISN[14] calculations. It was found that the total neutron flux in the liner increased 29%; the E > 0.1 MeV neutron flux decreased 0.8%; the intermediate neutron flux increased 38%; and the thermal neutron flux increased 46%. Thus, the effect of replacing a portion of the boronated graphite with graphite is to allow more low energy neutrons to penetrate the shield and reach the liner and PCRV. The dose rate at the tendon increased 12% while the maximum heating in the PCRV increased 16%. Even with these significant increases in the flux and dose levels in the PCRV and liner, the radiation levels still remain well below the constraints.

5.2 Upper Plenum Shield

The modelling for the upper plenum shield calculation was based on the design shown in Fig. 2. A plot of the 2-D model used is shown in Fig. 21. The outlet coolant duct has been modeled as a 360-degree opening in the PCRV with a height equal to the diameter of the duct. The duct was also represented as being horizontal rather than slant as shown in Fig. 2.

The source for this calculation was a boundary source output from the mid-level region calculation and corrected for the effects of axial radiation streaming. The source plane was located at the top of the orifice region (base of plenum). The streaming correction factors were applied uniformly over the entire source plane, though they probably should have been limited to the region inside the core barrel.

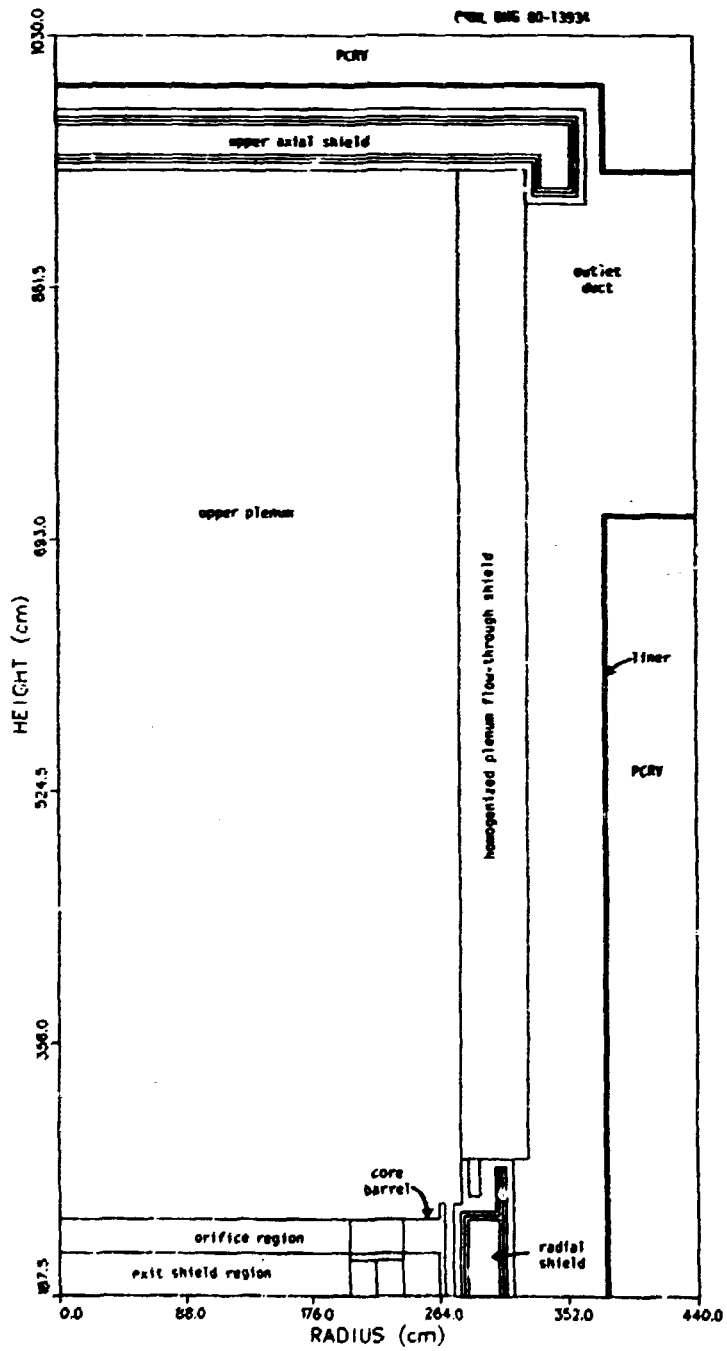

Fig. 21. Plot of the two-dimensional R-Z geometry used in the Conceptual Upflow GCFR upper region global calculation.

As with the mid-level region calculation, this calculation was performed using 76 groups, S_8 symmetric quadrature, and P_3 cross sections. The "weighted" flux extrapolation mode and the negative source fixup options were used, with the amount of fixup applied tapering off quite rapidly with decreasing neutron or gamma-ray energy.

One result of the calculation is shown in Fig. 22 which shows an isoplot of the 24 full-power-year neutron fluence in the upper plenum. The figure seems to indicate that the fluence constraint in the liner (10^{19} cm^{-2}) has been exceeded. However, as stated before, the streaming correction factors were applied uniformly over the entire source plane when they probably should have been restricted to regions inside the core barrel. The large streaming correction factors applied to the thermal neutron flux at the center of the reactor would not apply to regions beyond the radial blanket because of the more homogeneous nature of those regions. Thus, the apparent violation of the design constraint is probably not real but is the result of an overcorrection of the fluxes (the thermal fluxes in particular) in regions outside the core barrel. Since there appears to be streaming up the gap between the shield and the PCRV, the fluxes surrounding the gap probably were also influenced by the overcorrected source in the region. The fluxes at the inside radius of the plenum shield are greatly influenced by the source from the center of the reactor; hence, they more closely approximate the true fluxes in the upper plenum. Note that the fluence generally incident on the shield is about 3.2 x 10^{19} cm^{-2}, requiring a factor of 3.2 reduction to remain below the design constraint at the PCRV liner. As will be seen in a later section, the plenum shield design is capable of flux reductions of greater than a factor of 20. Consequently, the liner fluence constraint would not be exceeded.

Isoplots of additional activities are shown in Appendix B.

5.3 Lower Plenum Shield

As with the upper plenum shield analysis, the modelling for the 2-D calculation was based on the design shown in Fig. 2. The coolant duct was modelled in similar fashion and was also made horizontal as

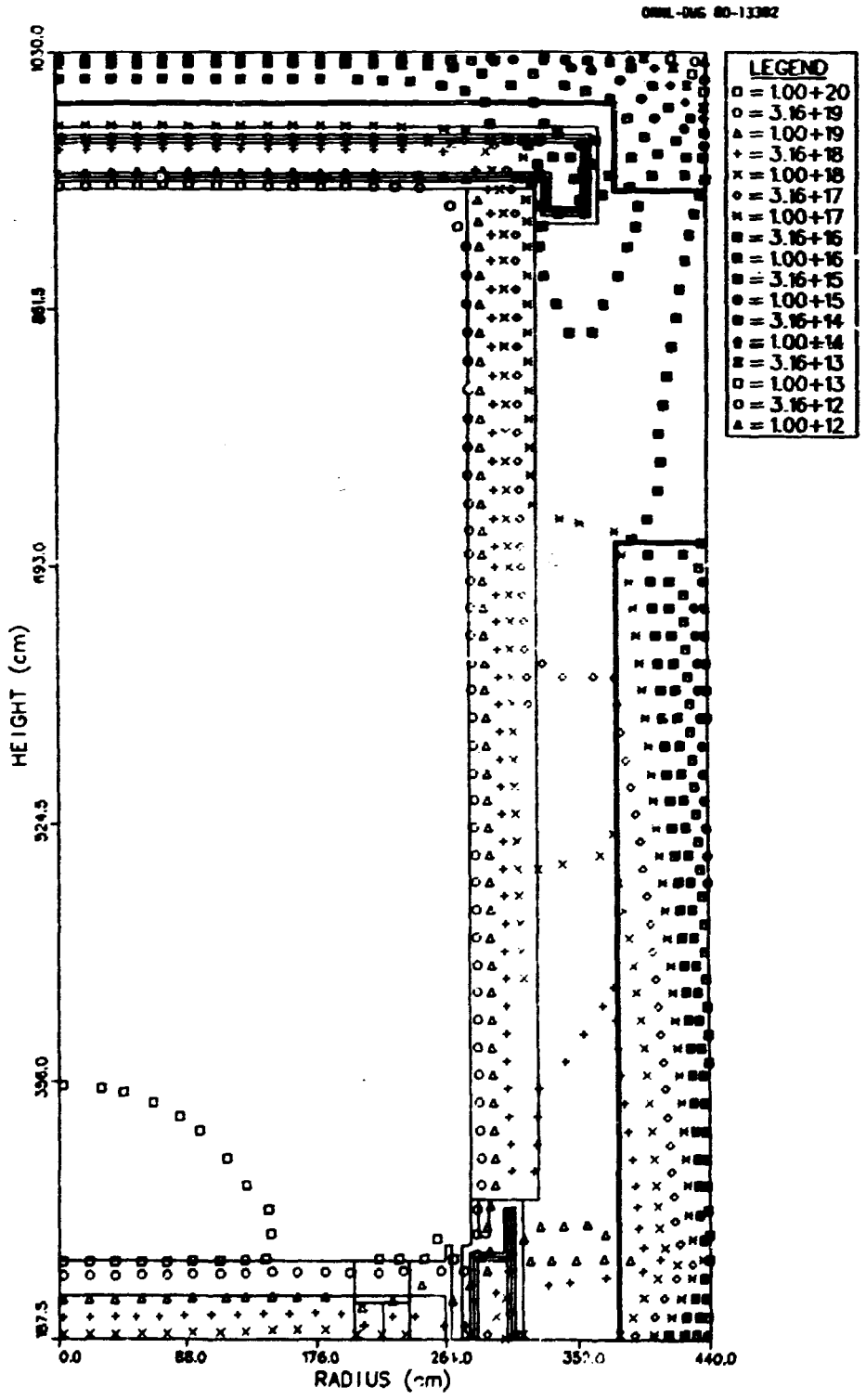

Fig. 22. Isoplot of the 24 full-power-year total neutron fluence in the Conceptual Upflow GCFR upper regions.

shown in Fig. 23. The streaming-corrected internal boundary source was located at the bottom of the grid plate (top of lower plenum). Again, the calculation used 76 groups, S_8 quadrature and P_3 cross sections and was performed in R-Z geometry with the two-dimensional discrete ordinates transport code, DOT-IV. This calculation also used the weighted flux extrapolation mode and the negative source fixup options.

In Fig. 24 an isoplot of the 24 full-power-year neutron fluence in the lower axial regions of the Conceptual Upflow GCFR is shown. It is first noted that even though the streaming correction factors were applied uniformly over the whole source plane, the region outside the plenum shield radius did not present a source on the outer side of the shield which overwhelmed that transmitted through the shield as was seen earlier in the upper plenum calculation. The major reason the source there was not so pronounced as that for the upper plenum is that in the lower regions the region between the radial shield and the PCRV liner is filled by an extension of the lower plenum shield, whereas the comparable region in the upper regions is not. The figure also shows the neutron fluence in the liner to be between 10^{17} and 10^{18} cm^{-2}, well below the design constraint of 10^{19} cm^{-2}. The maximum fluence at the inner radius of the lower plenum shield of 10^{20} cm^{-2} would require at least a factor of 10 reduction in the fluence to satisfy the design constraint for the liner. As stated earlier, all the plenum shield designs examined are capable of achieving even greater flux reductions.

The DOT-IV calculation for the lower plenum did not include the effects of fission in the depleted uranium (DU) regions of the core catcher. To determine these effects, three ANISN 1-D slab cases were run on mockups of the lower axial portion of the core catcher. The cases included: (1) all ^{238}U DU without fission (base case); (2) all ^{238}U DU with fission; and (3) 0.25% ^{235}U DU with fission. The third case was considered because it is near the concentration of ^{235}U in tailings from the enrichment process. (The Atomic Energy Commission considered a concentration of 0.22 weight percent (w/o) ^{235}U in its pricing formulas for enriching uranium.[15]) Also General Atomic Company[16] used a composition of 0.3 w/o ^{235}U in preliminary calculations of radiation heating rates within the core catcher.

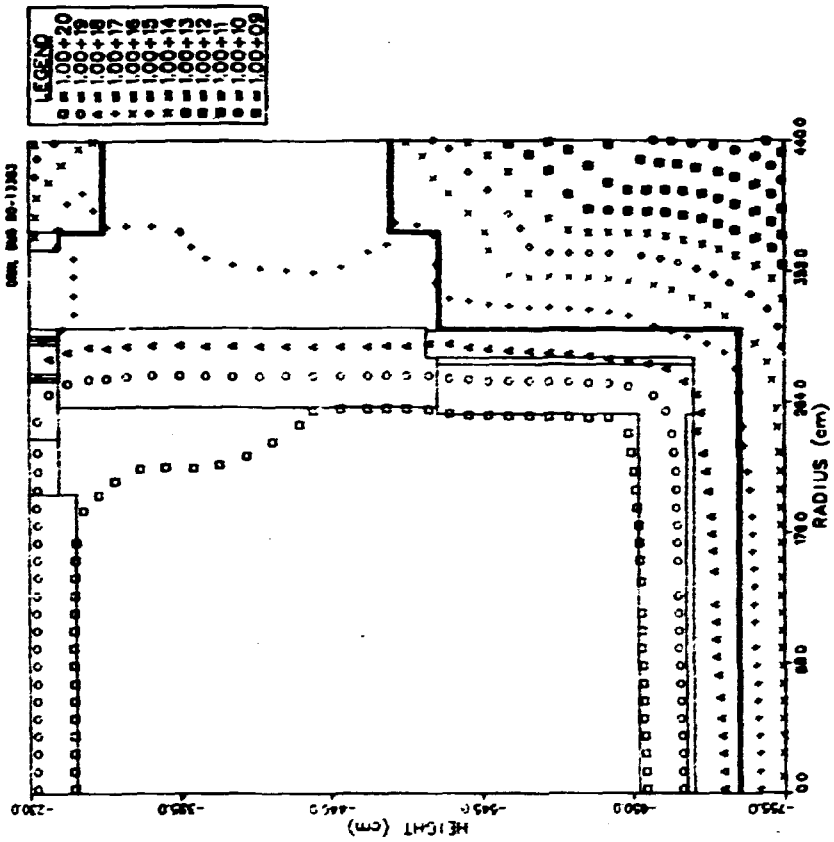

Fig. 24. Isoplot of the 24 full-power-year total neutron fluence in the Conceptual Upflow GCFR lower regions.

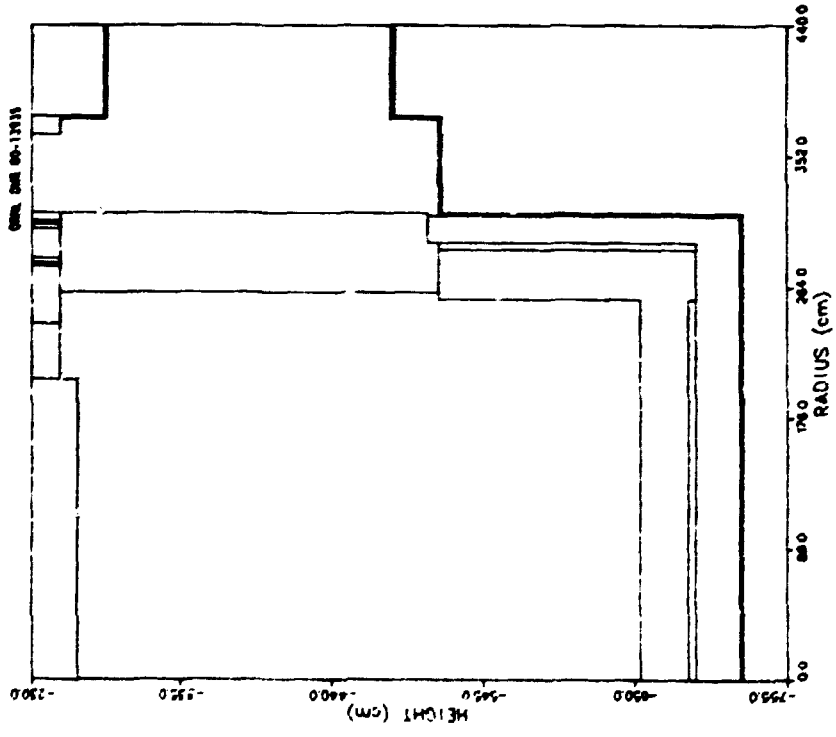

Fig. 23. Plot of the two-dimensional R-Z geometry used in the Conceptual Upflow GCFR lower region global calculation.

Several responses are compared for the three cases in Table 2. It can be noted that the fissions in a depleted uranium consisting of ^{238}U alone have little impact on responses except for the responses dominated by high energy neutrons (compare cases 1 and 2). There are two such responses listed in the table. The fissions in the ^{235}U show larger effects than the fissions in ^{238}U did. The total flux, the PCRV heating rate, and the intermediate and thermal neutron fluxes all show on the order of 10% or less difference between cases 1 and 3. The high energy fluxes, on the other hand, increased between one and two orders of magnitude. However, the flux levels in the PCRV liner for these energy ranges are low enough that increases of the order shown in Table 2 would result in a total fluence of 10^{16} cm^{-2} or less. Thus, the results of the ANISN 1-D slab cases do not indicate a need for additional shielding to reduce the fission source from the depleted uranium. The ANISN results indicate a maximum fission heating rate of 0.2 mW/cm^3 in the depleted uranium. When the ANISN responses for case 1 were compared with the DOT-IV responses (see Table 3), they were found to be higher by about 25% in the heating rates, 33% in the dose rate, and 45 to 55% in the neutron fluxes (the intermediate neutron flux was a notable exception, the ANISN result being only 23% higher). Thus a maximum fission heating rate of 0.16 mW/cm^3 in the depleted uranium might be expected.

Since the core catcher contained such a thick region of stainless steel (33 cm), an effort was made to determine if the fast neutron transport through the steel was being adequately calculated. To do this, reference was made to a report on a benchmark for neutron transport through iron and stainless steel.[17] A comparison was made between the neutron transmissions through 30.5 cm of stainless steel as determined from the experimental results and the ANISN calculation through the GCFR core catcher region. The incident spectra were quite different between the experiment and the GCFR. Of the $E > 0.0865$ MeV spectrum incident on the experimental configuration, 76% of the neutrons had energies greater than 0.907 MeV. On the other hand, only 1.2% of the GCFR $E > 0.0865$ MeV neutron source included neutrons with energies greater than 0.907 MeV. The two cases also differed in that the stainless steel

Table 2. Comparison of Responses Below the Conceptual Upflow GCFR Core Catcher Regions as a Function of the Depleted Uranium Composition

Response[a]	Case 1	Case 2 (R21)[b]	Case 3 (R31)[c]
Total neutron flux in PCRV liner	5.396+8	5.400+8(1.001)	5.944+8(1.102)
Maximum heating rate in PCRV	2.470-3	2.471-3(1.000)	2.683-3(1.086)
Dose rate 30 cm into PCRV	6.842+1	6.847+1(1.001)	7.622+1(1.113)
E > 1.0 MeV neutron flux in PCRV liner	8.994+3	1.226+4(1.363)	6.750+5(55.06)
E > 0.1 MeV neutron flux in PCRV liner	1.425+5	1.538+5(1.079)	2.427+6(15.78)
Intermediate neutron flux in PCRV liner	3.346+8	3.348+8(1.001)	3.719+8(1.111)
Thermal neutron flux in PCRV liner	2.049+8	2.050+8(1.000)	2.201+8(1.074)

[a] Flux units are $cm^{-2}.s^{-1}$ and heating rate units are mW/cm^3

[b] R21 = ratio of case 2 results to those for case 1

[c] R31 = ratio of case 3 results to those for case 1

Table 3. Comparison of ANISN and DOT-IV Calculated Responses in the Lower Axial Regions of the Conceptual Upflow GCFR

Response type	Calculated responses		Ratio: ANISN / DOT-IV
	DOT-IV	ANISN	
Total neutron flux ($cm^{-2}.s^{-1}$)	1.328+7	1.921+7	1.45
E > 1.0 MeV neutron flux ($cm^{-2}.s^{-1}$)	1.867+2	2.861+2	1.53
E > 0.1 MeV neutron flux ($cm^{-2}.s^{-1}$)	5.497+2	8.579+2	1.56
Intermediate neutron flux ($cm^{-2}.s^{-1}$)	5.064+5	6.271+5	1.23
E < 2.38 eV neutron flux ($cm^{-2}.s^{-1}$)	1.278+7	1.858+7	1.45
SS316 heating (mW/cm^3)	1.132-3	1.445-3	1.28
Concrete heating (mW/cm^3)	2.596-4	3.263-4	1.26
Total dose (rd)	1.473+7	1.953+7	1.33

slab for the experiment was unreflected while the GCFR steel slab was followed by depleted uranium and other regions.

For the E > 0.907 MeV neutrons, the experiment showed a factor of four smaller neutron transmission than did the GCFR design calculation. Both the experiment and the design calculation showed essentially the same transmission for the E > 0.0865 MeV neutrons. It thus appears that the calculations of neutron transport through the thick stainless steel region of the GCFR core catcher were adequate. Since the iron cross section minima are generally masked by the cross sections of the other steel components, it is felt that the neutron transmission was adequately calculated in energy ranges containing the principal iron minima.

Because of the regions following the stainless steel in the GCFR core catcher, the six-inch Bonner ball response, which gives a reasonable estimate of the total E > 0.4 eV neutron flux, was not very useful in assessing the neutron transmission through stainless steel. The design calculation showed a transmission of 0.059 while the experiment showed 0.0033, or a factor of 18 less. Of course, the spectra between the experiment and the GCFR were different and probably accounted for part of the difference in the transmissions. However, since the transmissions were obtained by taking ratios of six-inch Bonner ball count rates obtained from similar spectra, it is believed that the transmissions are reasonable. Thus, it would appear that the calculated responses in regions below the core catcher are conservative.

Isoplots of additional activities for the lower plenum regions are included as Appendix C.

5.4 Flow-Through Plenum Shield Slit Streaming

As described in section 2.0, the plenum shields are penetrated radially by coolant paths having one or two bends, thus allowing coolant to pass through while controlling neutron transmission through the shield. A preliminary analysis was done on several slit designs to aid in a decision on a final design. The preliminary and final analyses are described in the following sections.

5.4.1 Preliminary Flow-Through Shield Design Analysis

Four preliminary plenum shield designs for the lower plenum and one for the upper plenum were analyzed. The shield designs for the lower plenum included chevrons with coolant path widths of 5.08, 7.62, and 10.16 cm and a herringbone with a coolant path width of 5.08 cm. A chevron with a 5.08-cm coolant path width was considered for the upper plenum. All shields were assumed to have a thickness of 53.34 cm and an inner radius of 280.67 cm.

Calculations were done with the discrete ordinates code DOT-IV for cell mockups of all the shield designs and with the MORSE[18] Monte Carlo code for the 10.16-cm chevron and the 5.08-cm herringbone shield designs. In each case a 76 group structure (51 neutron and 25 gamma-ray groups) and a P_3 cross section expansion were used. In addition, the discrete ordinates calculation used a symmetric S_{12} quadrature set which contained 96 discrete directions. An upper plenum boundary source and a lower plenum one, both assumed to have a cosine distribution with respect to the surface normal, were obtained from the flux output from the previous shielding analysis.[1] The intent was to have relative spectra which would be representative of spectra in the upper and lower plena of the conceptual design.

The geometry mockup used in the DOT-IV calculations for the 10.16 cm chevron is shown in Fig. 25. The cell has been modeled in X-Y geometry and has undergone a transformation from the curvilinear cell of 7.5-degree periodicity to a rectangular cell by redistribution of materials The rectangular cell measured 40.2 cm by 53.34 cm, the latter dimension corresponding to the shield thickness. The former dimension was obtained by averaging the curvilinear cell dimensions on the inner and outer surfaces of the shield.

The geometry mockup used in the MORSE calculation for the 10.16 cm chevron is shown in Fig. 26. This mockup has the curvature of the shield built into it. Hence, if 48 of these mockups were placed end-to-end, they should form a complete circle. The periodic boundary conditions were simulated by moving the particle to the opposite boundary

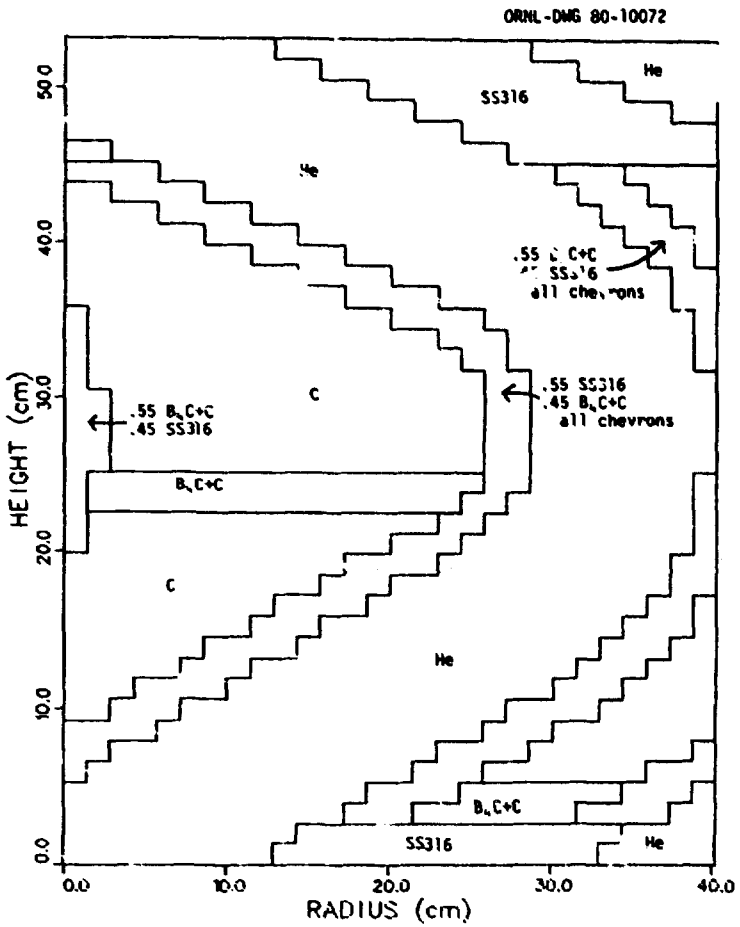

Fig. 25. Plot of the cell geometry model used in the DOT calculation for the 10.16 cm chevron plenum flow-through shield.

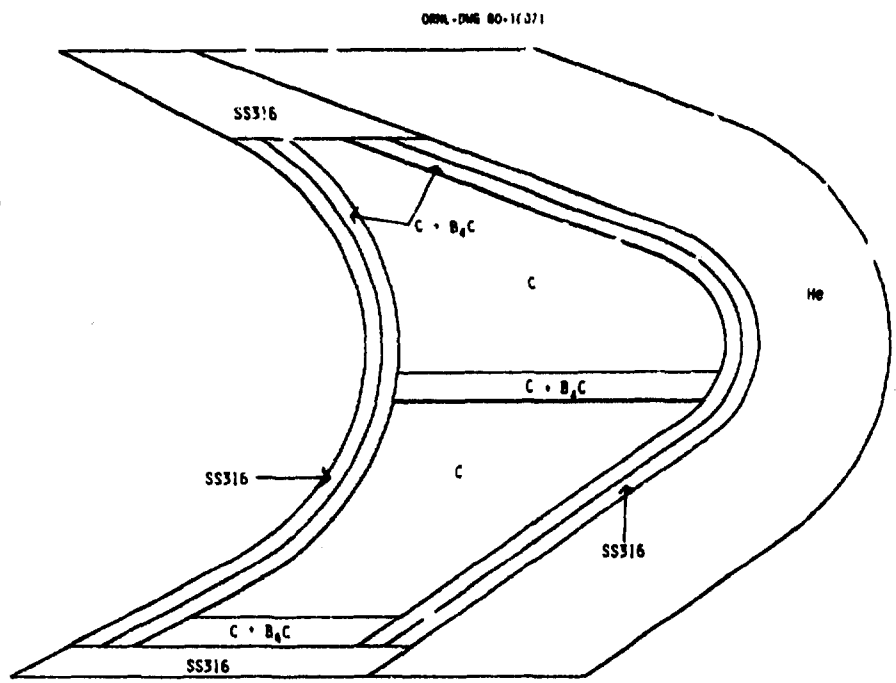

Fig. 26. Plot of the cell geometry model used in the MORSE calculation for the 10.16 cm chevron plenum flow-through shield. When models are placed end-to-end, they form a circular shield.

and performing the proper rotation of the direction vector to account for the curvature of the shield. A MORSE mockup for the 5.08-cm herringbone plenum shield design is shown in Fig. 27.

The primary reasons for these preliminary analyses were to determine the relative shielding effectiveness of the shields and to determine which designs were adequate to reduce the neutron fluence incident on the shield sufficiently so that the neutron fluence in the liner would not exceed the constraint of 10^{19} cm^{-2}. Previous results had shown a neutron fluence of 10^{18} cm^{-2} incident on the upper plenum shield and 10^{19} cm^{-2} incident on the lower plenum shield. Obviously, either of the shield designs would satisfy the liner neutron fluence constraint, since the fluences were already at or below the constraint. However, later changes made to the design led to increases in the flux levels in both the upper and lower plena.

The results of the DOT-IV discrete ordinates calculations are summarized in Table 4 which gives neutron transmission and flux reduction factors for homogeneous and heterogeneous cell mockups of the plenum shield designs. The factors for the homogeneous shield mockups should be indicative of the flux reduction one should see in a global calculation of the plenum shields. For the upper plenum with its 5.08-cm chevron design, Fig. 22 shows a flux reduction factor of at least 316 in the vicinity of the coolant duct. This factor is only one-third that shown for the homogeneous cell mockup in Table 4, partially because of the streaming up the gap between the plenum shield and the PCRV liner (see Fig. 22) and partially because of neutron backscattering from radial regions beyond the plenum shield. Also the plenum shield in Fig. 22 is 7.6 cm thinner than that of Table 4. The calculated fluence for the 7.62-cm chevron in the lower plenum was shown in Fig. 24. From that figure it is seen that the global calculation with the homogenized shield gives a flux reduction factor between 100 and 1000; but, like the upper plenum calculation results, the lower plenum flux reduction factor from the global calculation is probably lower than that from the homogeneous cell calculation for similar reasons, except for shield thickness.

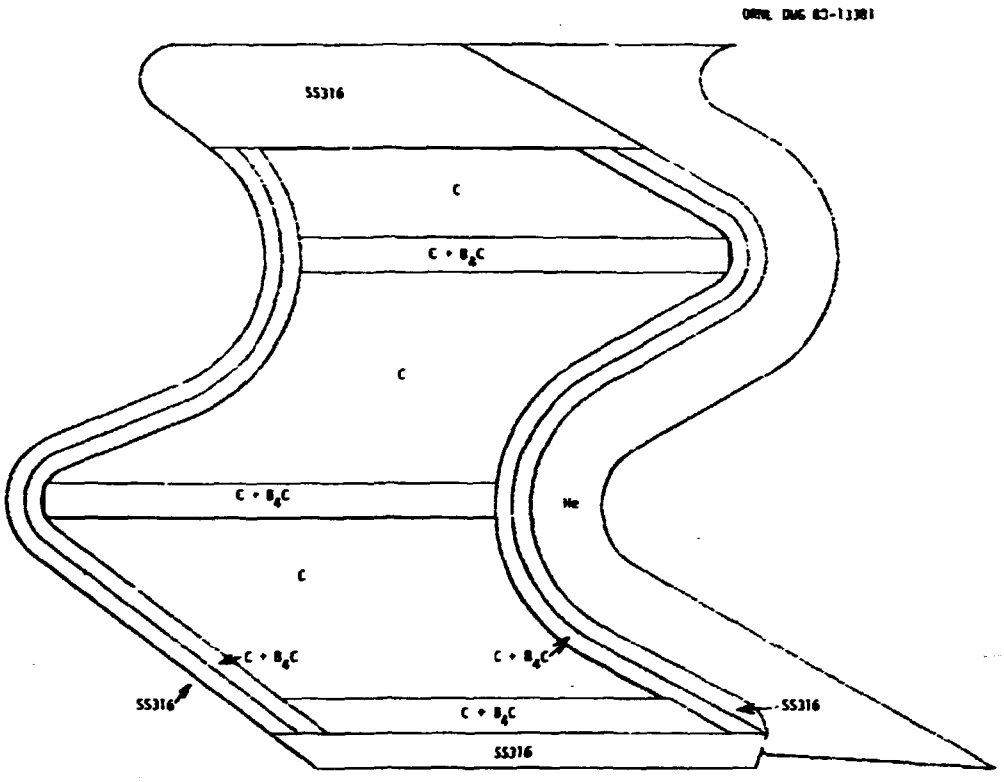

Fig. 27. Plot of the cell geometry model used in the MORSE calculation of the 5.08-cm herringbone design plenum flow-through shield.

It is noted from Table 4 that the flux reduction factors for the chevron designs range from 44 to 88 and that the herringbone shield is probably twice as effective as the chevron shield with the equivalent coolant flow-through path thickness.

MORSE results for the 10.16-cm chevron shield are compared with DOT results in Table 5. Two sets of MORSE results were obtained: (1) results based on the explicit mockup of the steel and B_4C liners surrounding the coolant passage and (2) results based on a mockup in which the steel and B_4C liners surrounding the coolant passage were homogeneously mixed. The first case is referred to as the "discrete liners" case while the second is referred to as the "mixed liners" case. The mixed liners case mockup more closely resembles the DOT-calculation mockup. Note that for the discrete liners case the MORSE-calculated neutron transmission factor is 24% higher than the DOT-calculated one.

Table 4. Discrete Ordinates Calculated Neutron Transmission and Flux Reduction Factors for Several Upflow GCFR Plenum Shield Configurations

Shield type	Transmission factors		Flux reduction factors*	
	Heterogeneous shield	Homogeneous shield	Heterogeneous shield	Homogeneous shield
Lower plenum				
10.16-cm chevron	.0225	.0043	44.4	233
7.62-cm chevron	.0158	.0017	63.4	591
5.08-cm chevron	.0114	-	87.9	-
5.08-cm herringbone	.0064	.0006	155	1620
Upper plenum				
5.08-cm chevron	.0149	.0011	67.1	947

*Reciprocals of the transmission factors

Table 5. Neutron and Gamma-Ray Transmission Factors* for the 10.16-cm Chevron Shield

Type	Method	
	Discrete ordinates (DOT)	Monte Carlo (MORSE)
Neutron	.0225	.0279 ± 9%
Gamma-ray	.1229	.1188 ± 11%
Total	.0341	.0384 ± 7%

*Based on the ratio of the leakage from the outer face of the shield to the incident source.

The flux reduction factor (35.8) which is the reciprocal of the transmission factor would be about 81% of the DOT-calculated flux reduction factor (44.4). The gamma-ray transmission factor is slightly higher for DOT than for MORSE. The factor is greatly influenced by the neutron flux distribution within the shield. The discrete mockup of the B_4C liner in MORSE significantly lowered the thermal neutron leakage from the central graphite region into the steel liner region. This in turn lowered the gamma-ray production in the steel liner and subsequently the gamma-ray leakage from the shield. The higher MORSE-calculated neutron transmission also means less gamma-ray production in the shield and thus less leakage from the shield.

The MORSE mixed liners case gave a neutron transmission factor which was in better agreement with the DOT-calculated transmission factor than was that for the MORSE discrete liners case. Also the MORSE to DOT gamma-ray transmission ratio is more consistent with the MORSE to DOT neutron transmission ratio. The total transmission ratio remained essentially the same. It is clear that the manner of mocking up the B_4C and steel liners does impact the leakage from the shield.

The herringbone calculation was a bit more difficult for MORSE than was the 10.16 cm chevron calculation. Unlike the 10.16-cm chevron, the leakage from the herringbone shield is dominated by multiply-collided particles. Also, the narrower coolant path causes less penetration into the shield and larger statistical uncertainties in the calculated leakage. The MORSE transmission factor was only 1/3 of the DOT one when an analog scoring procedure was used. A last flight boundary crossing estimator was implemented in MORSE along with biasing within the coolant path. These results compared more favorably with the DOT results as shown in Table 6. The neutron-transmission agreement is excellent between MORSE and DOT while the MORSE gamma-ray transmission is about 30% below the DOT-calculated transmission. While some underprediction of the radiation transmission down the third leg of the coolant path could be expected with DOT due to its discrete directions, the excellent comparison of neutron transmission indicates that DOT calculated the transmission with reasonable precision.

Table 6. Comparison of MORSE and DOT Transmission Factors for the 5.08-cm Herringbone Shield

	Transmission factors		Ratio: MORSE / DOT
	DOT	MORSE	
Neutron	.0065	.0069 ± 12%	1.06
Gamma-ray	.1214	.0832 ± 9%	0.69
Total	.0198	.0157 ± 7%	0.79

Isoplots of the DOT-calculated total flux are shown for the five cases analyzed in Figs. 28-32. The source plane is at the top of the figure in each case. The right and left boundaries have periodic conditions, and the lower boundary has a vacuum condition. The streaming down the coolant paths is evident. However, at the left side of each figure it appears that there is streaming through the shield material. This is actually due to neutrons streaming down the first leg of the coolant path and continuing into the shield. This results in some short-circuiting of radiation from the first leg of the coolant path, through the shield, and into the exit of the coolant path. For the chevrons the effect seems to be more pronounced with the smaller coolant paths. For the herringbone the effect is even more pronounced, because the third leg of the coolant path is nearly lined up with the first leg of an adjacent one to the left. The main route of travel for neutrons which leak from the shield would thus appear to be down the first leg of the coolant path, straight ahead through the shield material, and out the third leg of an adjacent coolant path.

The incident and emergent flux spectra for the five cases are compared in Figs. 33-37. The emergent fluxes have been multiplied by the approximate total neutron flux reduction factor in order to place the two spectra on the same scale. For the 10.16-cm and 7.62-cm chevrons, the emergent flux spectra appear to be relatively harder than the incident spectra. For the others, the emergent flux spectra have been downgraded in energy. Particularly noticeable energy degradation occurred in the 0.1 MeV to 0.5 MeV energy range in the 5.08-cm chevron calculations.

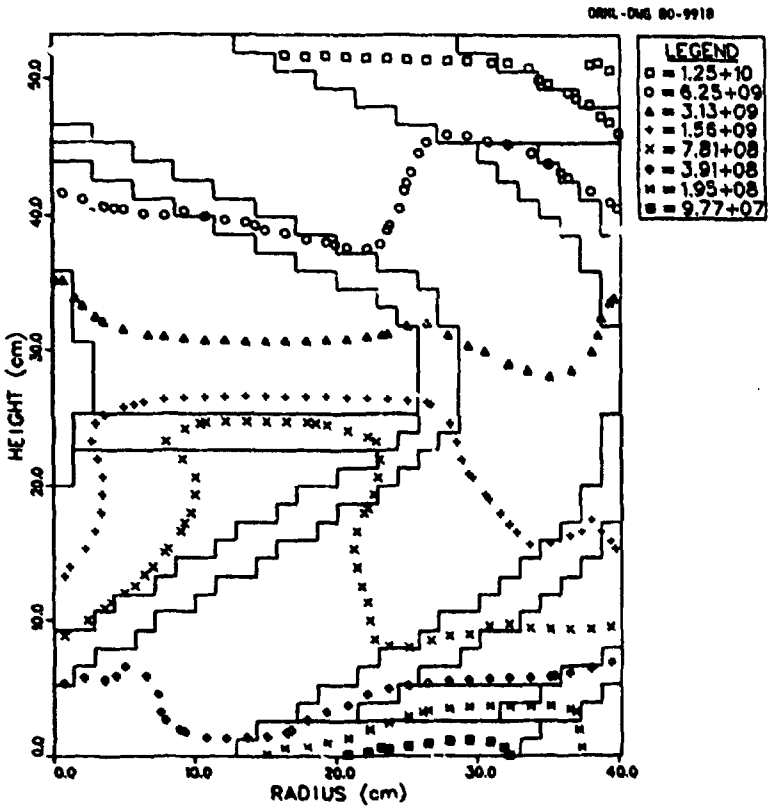

Fig. 28. Isoplot of the total neutron flux in a 2-D X-Y mockup of the 10.16-cm chevron lower plenum flow-through shield.

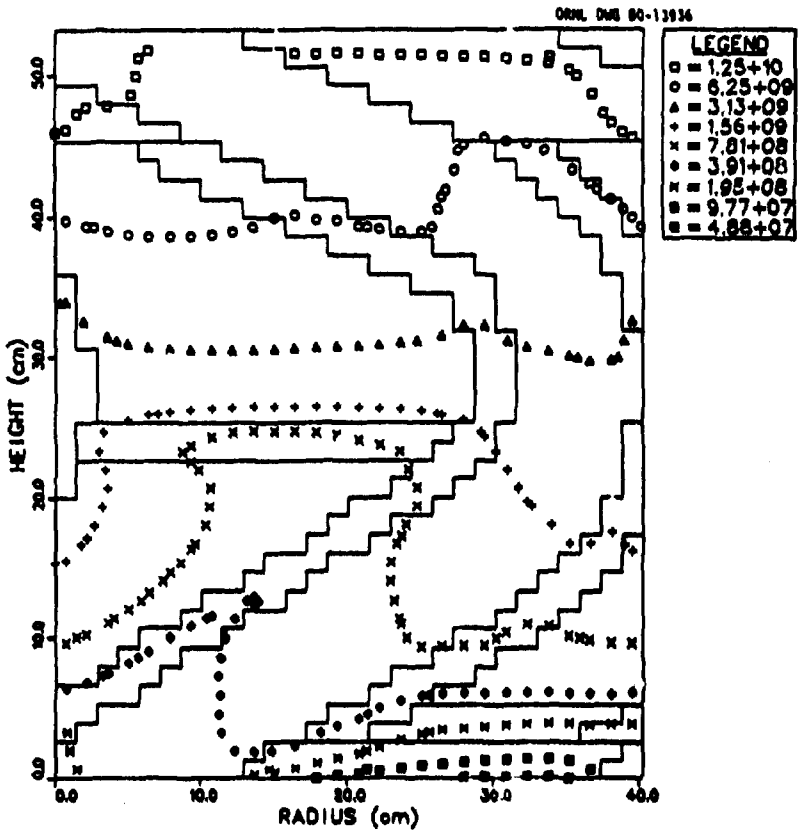

Fig. 29. Isoplot of the total neutron flux in a 2-D X-Y mockup of the 7.62-cm chevron lower plenum flow-through shield.

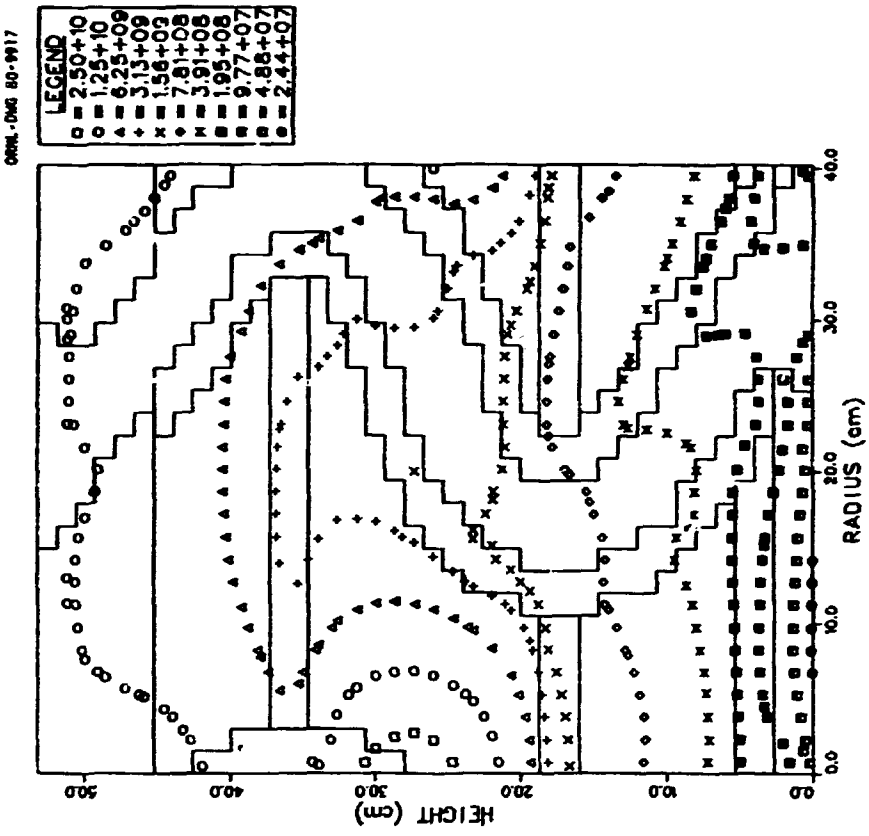

Fig. 31. Isoplot of the total neutron flux in a 2-D X-Y mockup of the 5.08-cm herringbone lower plenum flow-through shield.

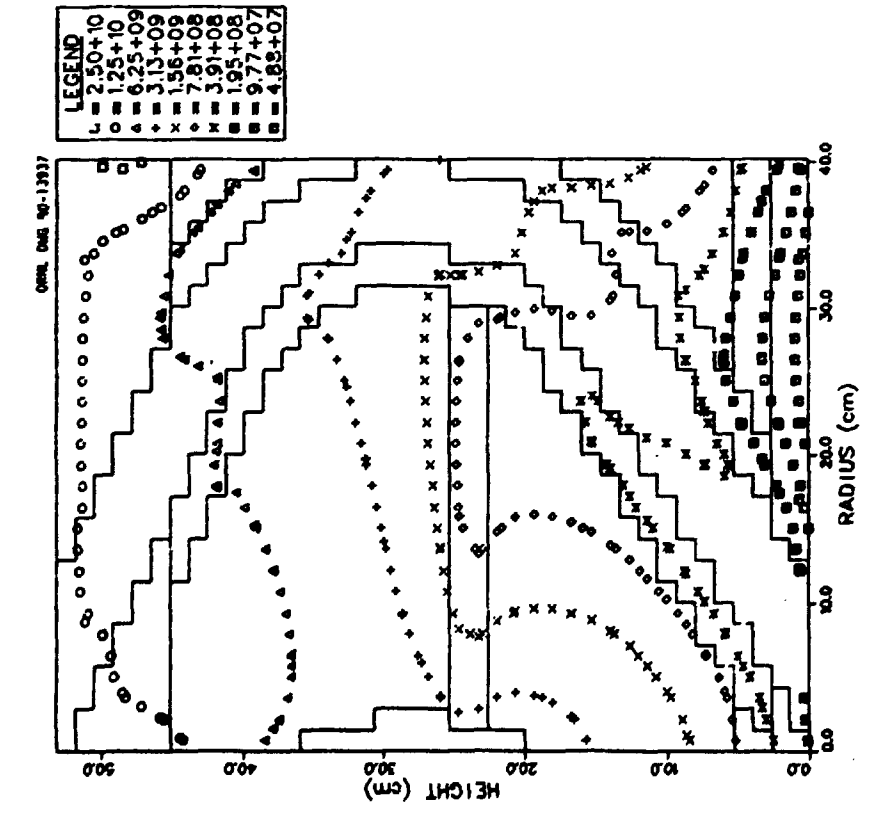

Fig. 30. Isoplot of the total neutron flux in a 2-D X-Y mockup of the 5.08-cm chevron lower plenum flow-through shield.

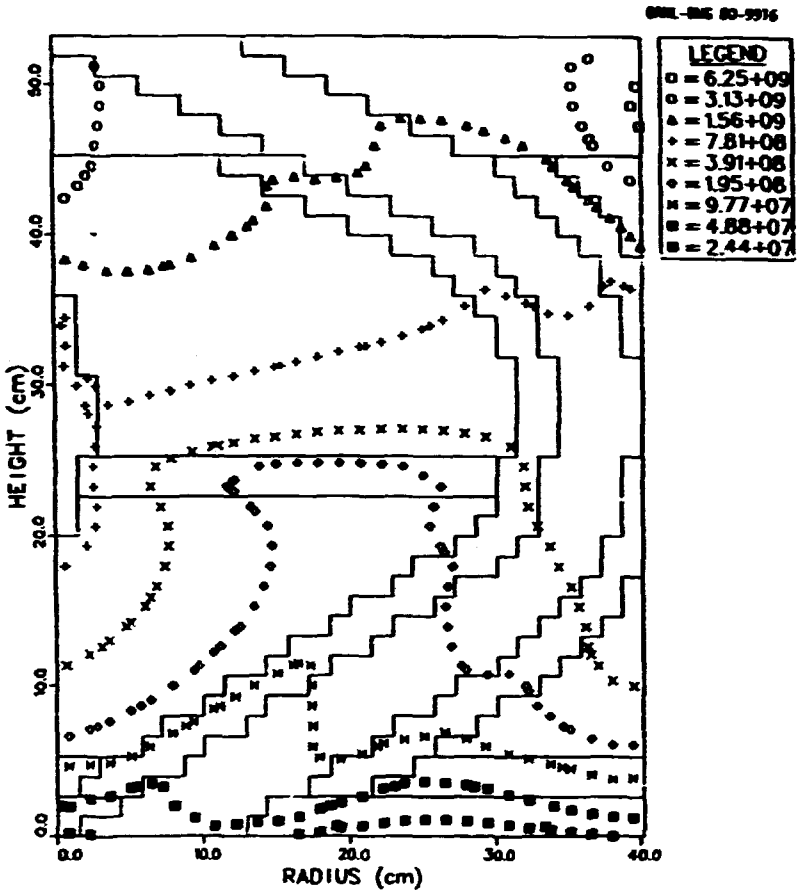

Fig. 32. Isoplot of the total neutron flux in a 2-D X-Y mockup of the 5.08-cm chevron upper plenum flow-through shield.

The conclusion from the preliminary analysis of the plenum flow-through shields was that given the maximum flux likely to be in either plenum, and the previous relationship of the maximum flux in the plenum to the flux incident on the shield, any of the shield designs would be more than adequate to limit the neutron fluence to the PCRV liner to less than the constraint of 10^{19} cm^{-2}.

5.4.2 Final Flow-Through Shield Design Analysis

The final plenum flow-through shield design analysis was begun following General Atomic Company's selection of their plenum shield designs (5.08-cm chevron for the upper plenum and 7.62-cm chevron for the lower plenum). The homogeneous compositions of the shields were determined for use in the upper (section 5.2) and lower (section 5.3)

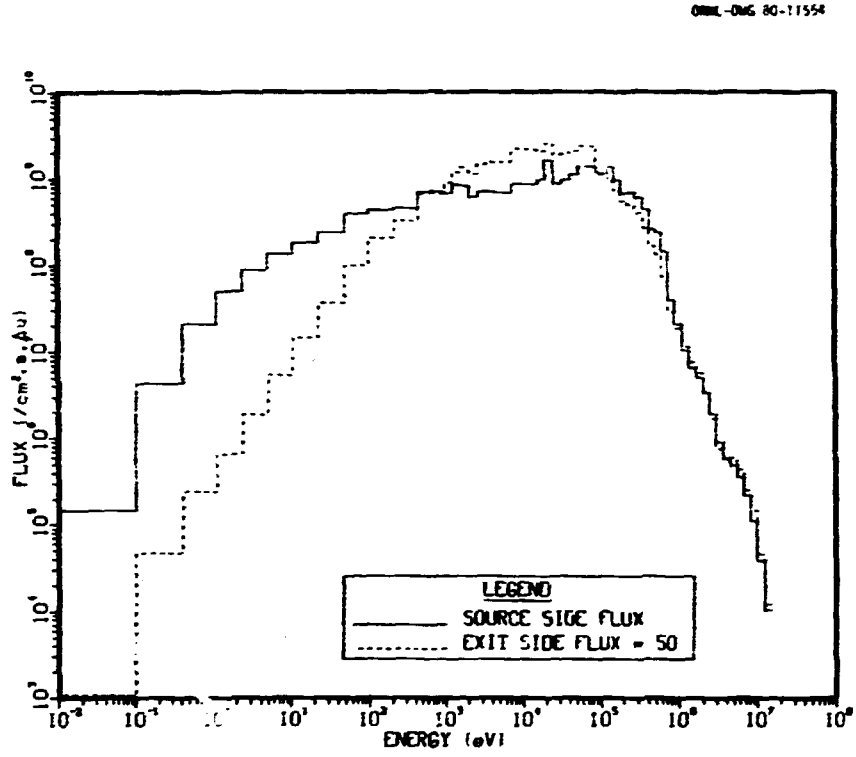

Fig. 33. Comparison of incident and transmitted neutron flux spectra per unit lethargy for the 10.16-cm chevron lower plenum flow-through shield.

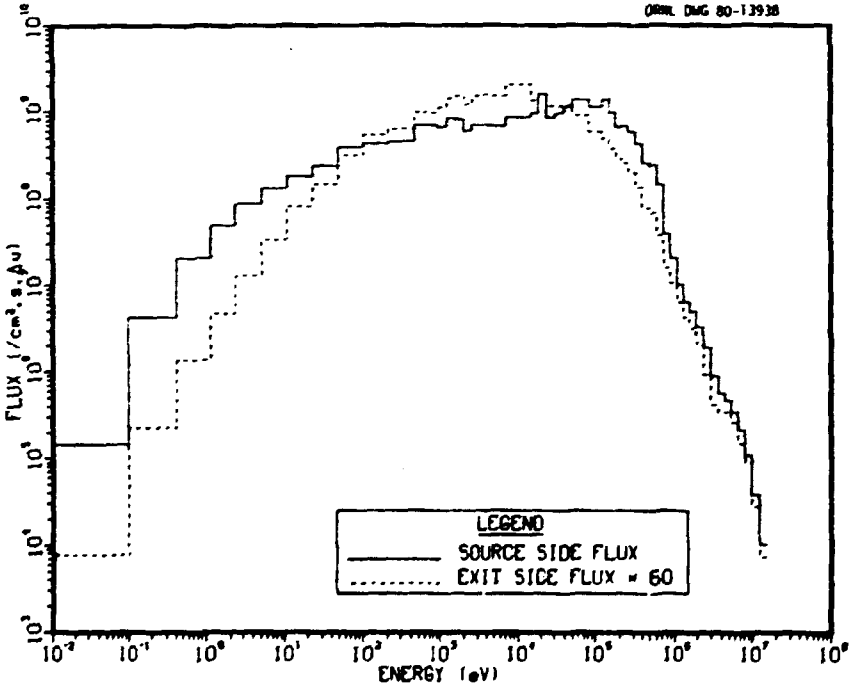

Fig. 34. Comparison of the incident and transmitted neutron flux spectra per unit lethargy for the 7.62-cm chevron lower plenum flow-through shield.

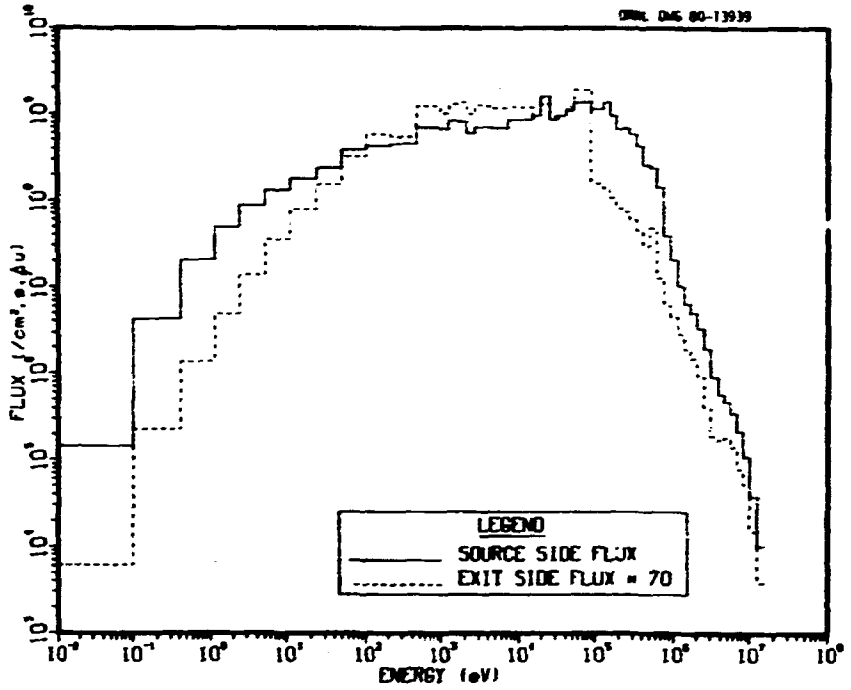

Fig. 35. Comparison fo the incident and transmitted neutron flux per unit lethargy for the 5.08-cm chevron lower plenum flow-through shield.

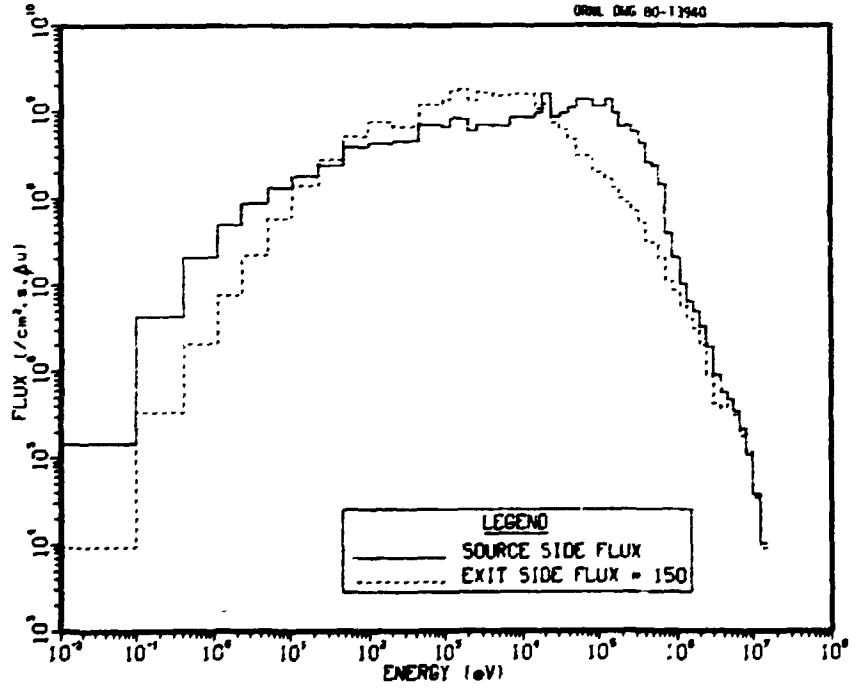

Fig. 36. Comparison of the incident and transmitted neutron flux spectra per unit lethargy for the 5.08-cm herringbone lower plenum flow-through shield.

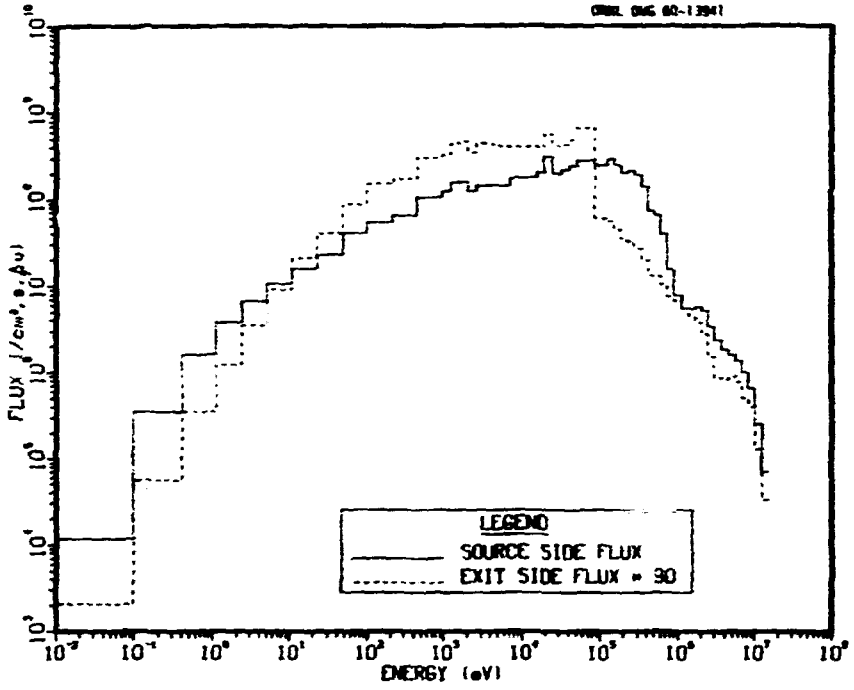

Fig. 37. Comparison of the incident and transmitted neutron spectra for the 5.08-cm chevron upper plenum flow-through shield.

plenum shield global calculations. From the global calculations were obtained external boundary sources for the cell streaming calculations. The global calculations used S_8 symmetric quadrature (48 directions), while the cell streaming calculations used S_{12} symmetric quadrature (96 directions). Hence the boundary flux from the global calculation had to be converted to an equivalent boundary source having S_{12} quadrature. The quadrature change was performed with the FACT[19] code with conversions of the boundary sources from DOT-IV format to FACT format and vice-versa being performed by auxiliary codes written by the user. The fluxes were averaged over the portion of the plenum shield at the coolant duct level (entry duct for the lower plenum and exit duct for the upper plenum). The fluxes were again averaged over the $\Omega_Z = \eta$ component of the direction vector and transformed from an R-Z system to an X-Y system for the local calculations. The group structure and the cross section expansion order were the same as before.

The upper and lower plenum shield DOT 2-D cell geometries are shown in Figs. 38 and 39, respectively. The length of the axis labeled

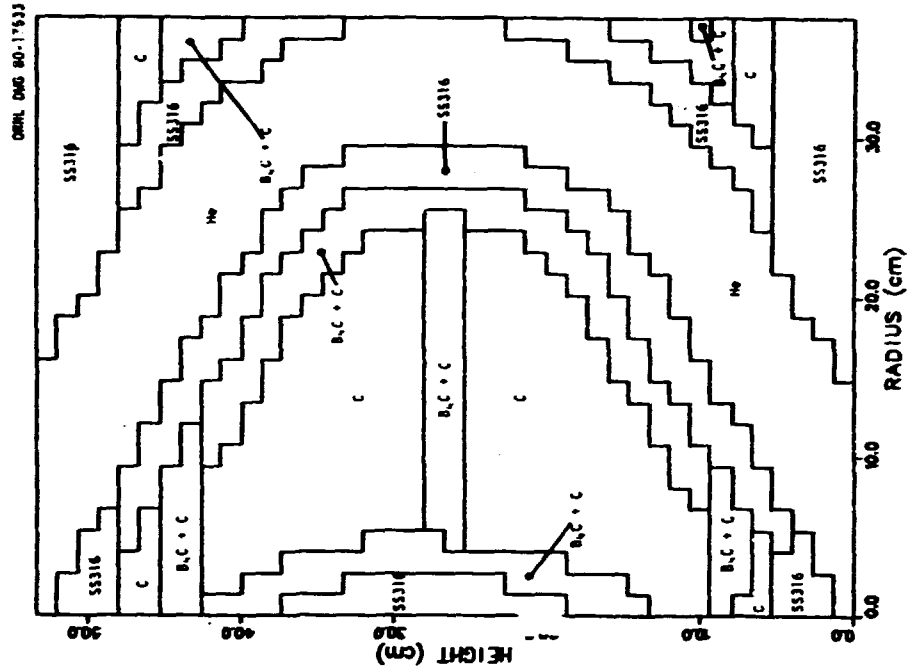

Fig. 39. Plot of the 2-D heterogeneous cell geometry for the Upflow GCFR lower plenum flow-through shield.

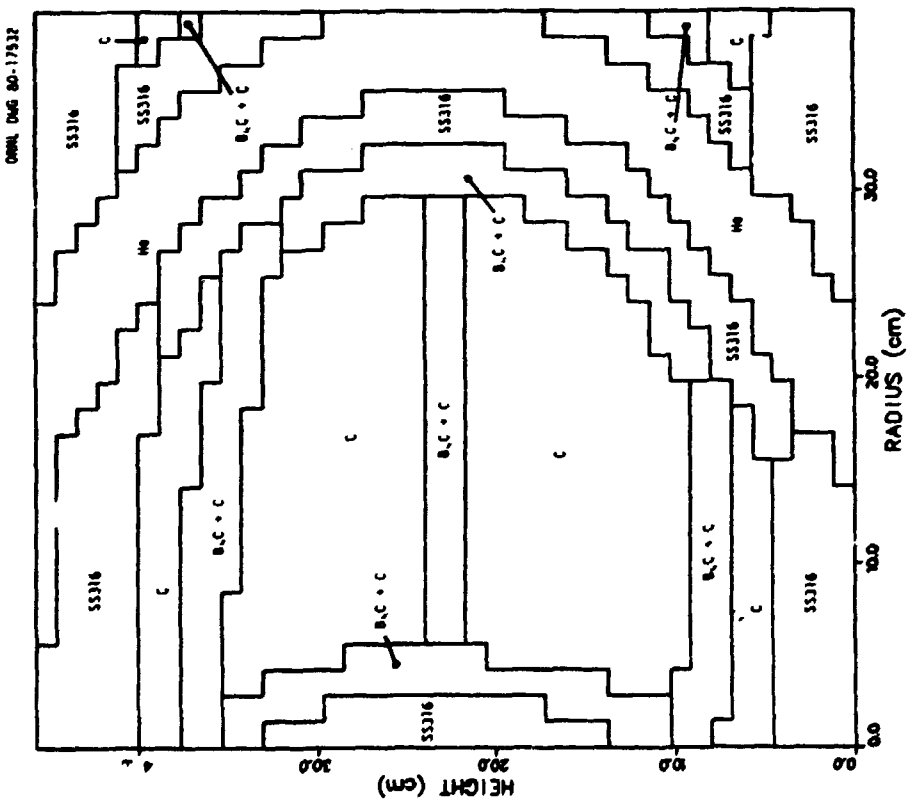

Fig. 38. Plot of the 2-D heterogeneous cell geometry for the Upflow GCFR upper plenum flow-through shield.

"RADIUS" was determined by averaging the arc lengths along the inner and outer surfaces of the shield for the 7.5 degree arc defining a unit cell. This dimension for the lower plenum shield is smaller than that for the upper plenum shield due to the smaller average radius for the lower plenum shield. As before, the cell has been made rectangular, and curved and slanted portions of the geometry have been stepped in order to do the 2-D DOT analysis. A density factor has been applied to each spatial mesh cell to account for displacement of material when the curved region boundaries were approximated by stepped boundaries. Periodic boundary conditions were applied to both sides; a vacuum boundary condition was applied to the bottom boundary and an external boundary source was placed at the top boundary of the geometry.

The DOT-calculated neutron transmission and flux reduction factors for heterogeneous cell mockups of the GCFR upper and lower plenum flow-through shields are shown in Table 7. When the results of Table 7 are compared with those in Table 4, it is noted that the new transmission factors (Table 7) are higher than the old ones (Table 4) in both plenums. The transmission factor increased 52% in the upper plenum and 108% in the lower plenum. Part of the reason for the increase in the upper plenum is that the new shield is only 45.7-cm thick compared to a 53.3-cm-thick shield for the results in Table 4. The influence of the differences in the source spectra on the neutron transmission is uncertain. For the lower plenum, the shield thickness is the same as before, hence differences in source spectra and the internal makeup of the shields must be responsible for the increases in the neutron transmission.

Figures 40 and 41 show isoplots of the 24 full-power-year total neutron fluences for the upper and lower plena, respectively. The results are similar to those obtained in the preliminary analysis (see Figs. 35 and 37). Neutron fluences on the inside and outside surfaces of the upper plenum shield are estimated to be 3.29×10^{19} cm^{-2} and 5.57×10^{17} cm^{-2}, respectively. The corresponding fluences for the lower plenum are 9.77×10^{19} cm^{-2} and 2.31×10^{18} cm^{-2}, respectively. The ratio of the flux incident to that exiting the shield is around

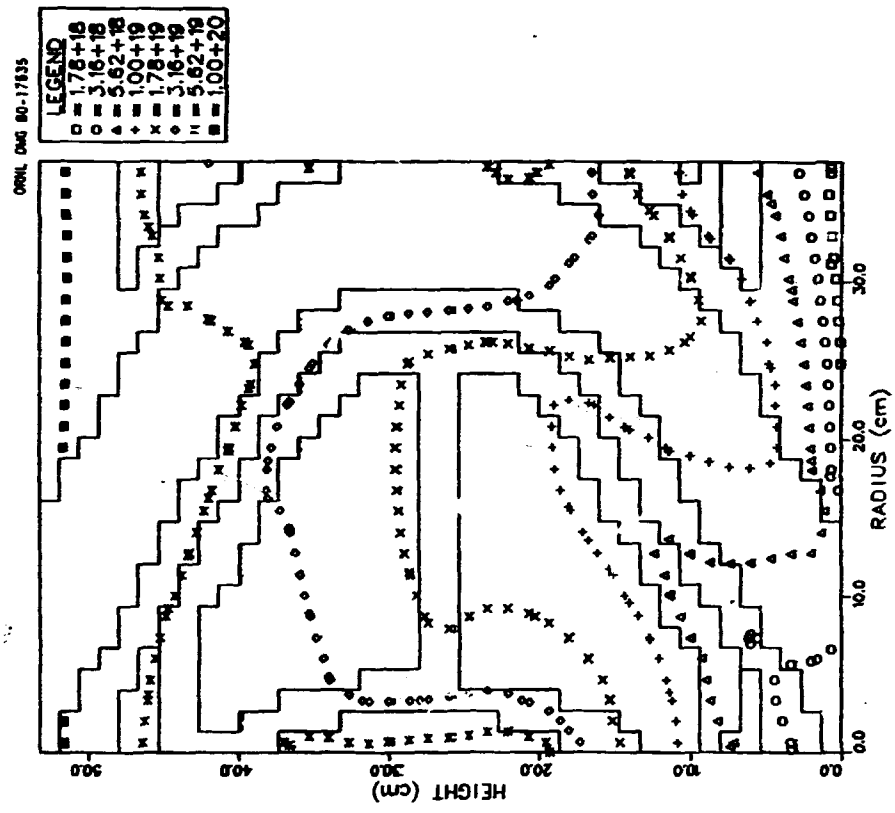

Fig. 41. Isoplot of the 24 full-power-year total neutron fluence in a heterogeneous cell mock-up of the Upflow GCFR lower plenum flow-through shield.

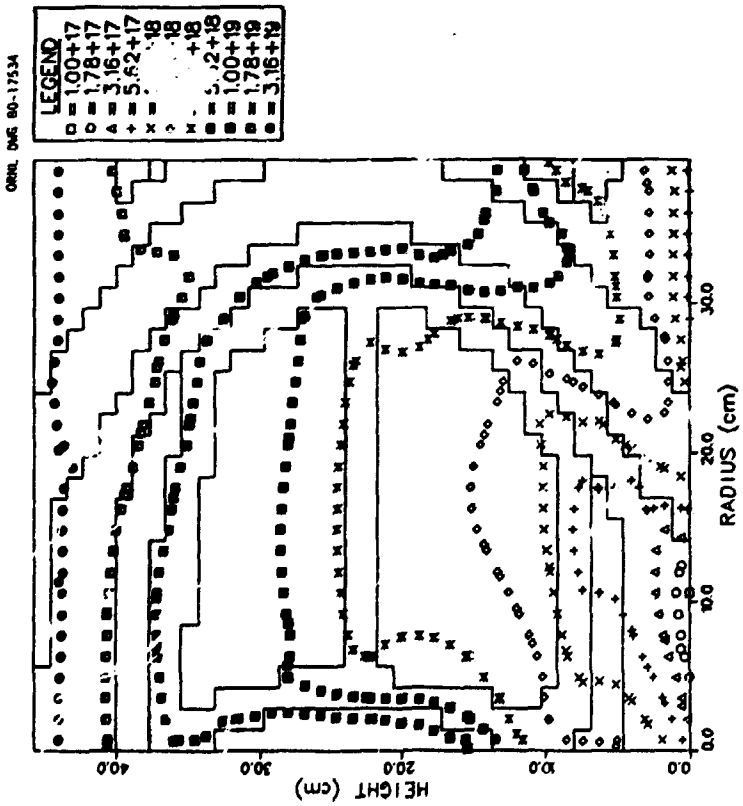

ig. 40. Isoplot of the 24 full-power-year total neutron fluence in a heterogeneous cell mockup of the Upflow GCFR upper plenum flow-through shield.

Table 7. DOT-Calculated Neutron Transmission and Flux Reduction Factors for the GCFR Plenum Flow Through Shields*

Shield type	Location	Neutron transmission factor	Neutron flux reduction factor
5.08-cm chevron	upper plenum	0.0227	44.0
7.62-cm chevron	lower plenum	0.0328	30.5

*Factors are based on the ratio of the neutron leakage from the shield to the source incident on the shield.

59 for the upper plenum shield and 42 for the lower plenum shield. As can be seen by comparing these results with those of Table 7, the true flux reduction factors are about one third larger than those based on the ratio of the leakage to the source. Without including the effects of neutron backscatter from the PCRV, it would appear that the upper plenum shield would leave the total fluence in the PCRV liner at least a factor of 18 below the design constraint of 10^{19} cm^{-2}, while the lower plenum shield would leave a smaller factor of 4 margin. Both shields are very adequate in their shielding effectiveness.

The spectra of the incident and exit neutron flux are compared in Figs. 42 and 43 for the upper and lower plenum shield, respectively. The exit flux has been multiplied in each case by 100 to make it on the order of the incident flux. This figure of 100 is a factor of 1.7 times the exit to incident flux ratio indicated earlier for the upper plenum shield and a factor of 2.4 times that for the lower plenum shield. For the upper plenum shield, the incident flux spectrum in Fig. 42 appears to be somewhat softer than that used for the preliminary analysis of the shield as shown in Fig. 37. The newly calculated emergent flux spectrum, while also appearing to be softer than before, does have the sharp transition in the spectrum at 0.1 MeV as was previously observed in the preliminary analysis. A little more structure in the new spectrum is observed for the region between 1 and 100 keV. As with the upper plenum,

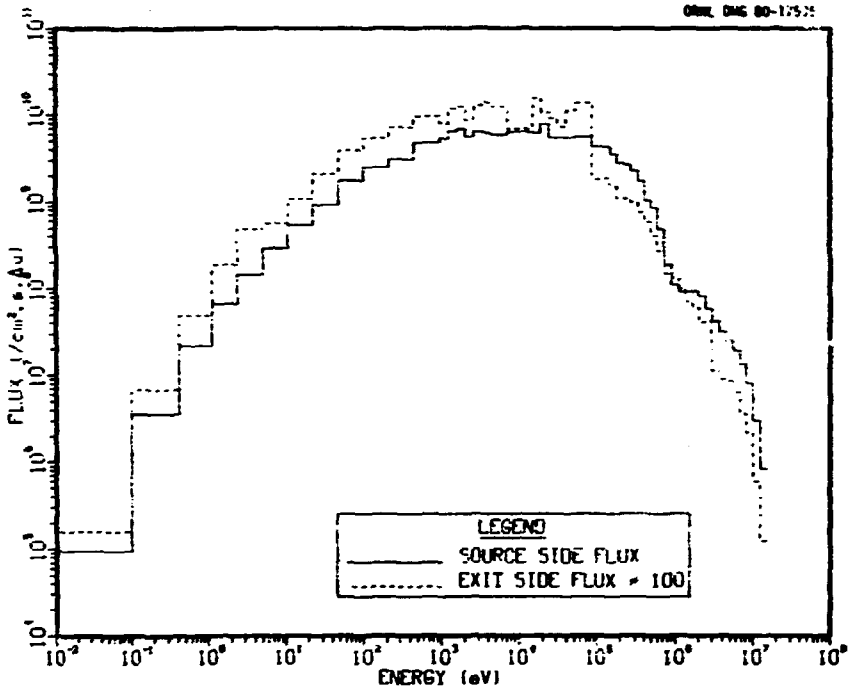

Fig. 42. Comparison of the neutron fluxes incident on and exiting from the GCFR upper plenum flow-through shield.

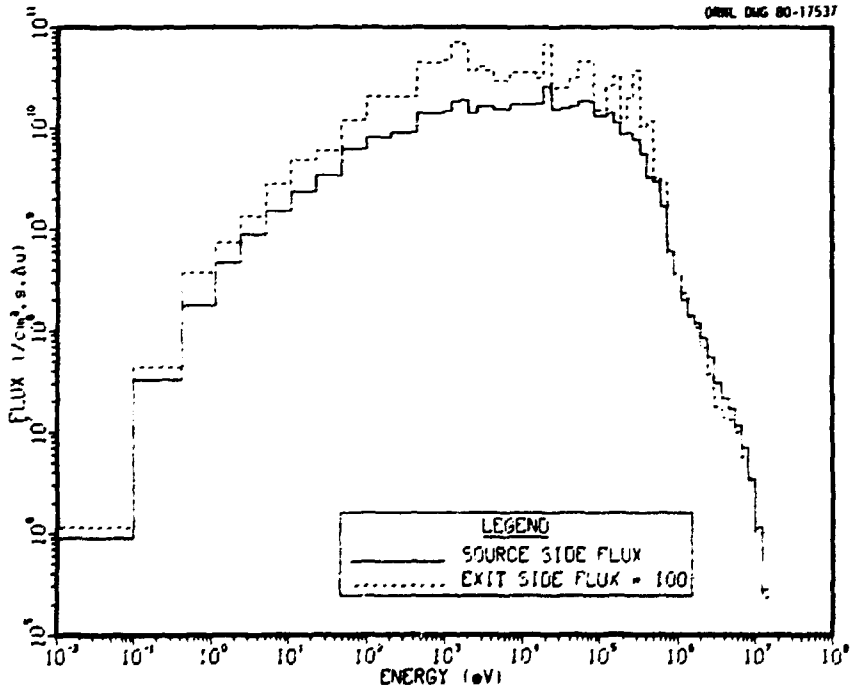

Fig. 43. Comparison of the neutron fluxes incident on and exiting from the GCFR lower plenum flow-through shield.

the new lower plenum incident and emergent flux spectra (Fig. 43) both appear to be slightly softer than those calculated in the preliminary analysis (Fig. 34). Like before, the calculated emergent spectrum for the 7.62-cm chevron shield does not show the sharp transition in the spectrum at 0.1 MeV as was observed for the 5.08-cm chevron shield for both plena in the preliminary analysis and for the upper plenum in the final analysis. Additionally, much more structure is observed in the emergent spectrum in the region between 1 and 500 keV than was seen in Fig. 34. This might have been influenced by the separate mockup of the boronated graphite and steel liners surrounding the coolant channel as contrasted with the mixing of those liners in the preliminary analysis.

Following the heterogeneous cell calculation for the lower plenum shield, a boundary source based on these cell results was created on the exit face of the plenum shield, and the calculation was continued into the lower duct and PCRV regions. The calculation was performed with DOT-IV in X-Y geometry at the axial midplane of the lower duct. The calculation used 76 groups (51 neutron and 25 gamma-ray), S_8 symmetric quadrature (48 directions), and P_3 cross section expansion. The geometry for this calculation was oriented differently from that for the cell calculation. Whereas the Y-axis went through the shield and toward the duct in the cell calculation, it was perpendicular to the duct in the follow on calculation. The duct region was modeled with the length of the Y-axis equal to the combined widths of eight of the chevron cell mockups. Both Y boundaries were reflected to account for the equal source strength along a ring around the plenum shield. The boundary flux over the original fine mesh in the plenum shield cell calculation was reduced to a boundary flux averaged over five intervals per cell; and with periodic repetition of the cell boundary flux, the internal boundary source for the duct calculation was created.

Since the coolant paths through the flow-through shield were not parallel to the coolant duct axis, one could not expect a symmetric angular flux distribution about normal to the shield outer surface. Instead, the flux distribution should be peaked about the centerline of the coolant flow-through path. This can be clearly seen in Fig. 44,

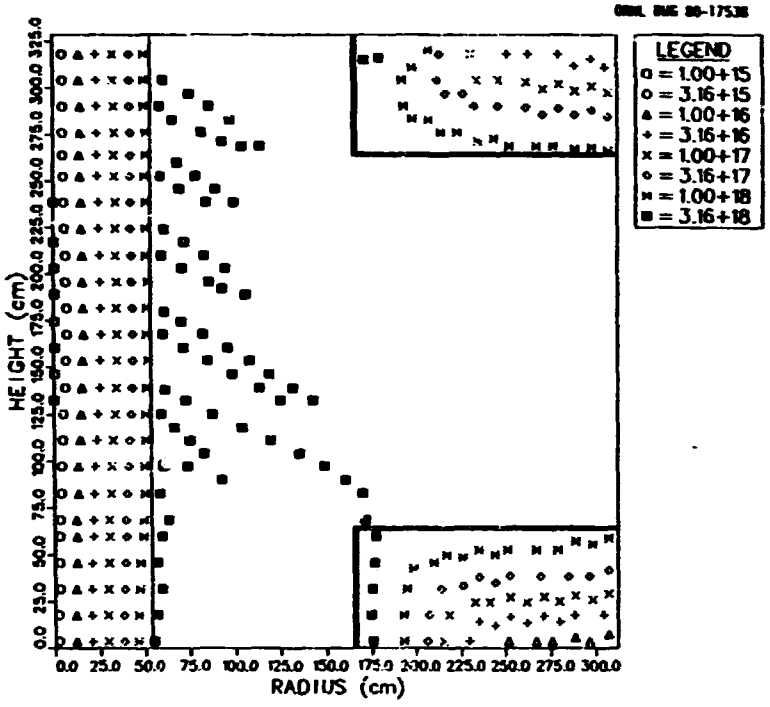

Fig. 44. Isoplot of the 24 full-power-year total neutron fluence (cm^{-2}) in the upflow GCFR inlet coolant duct region.

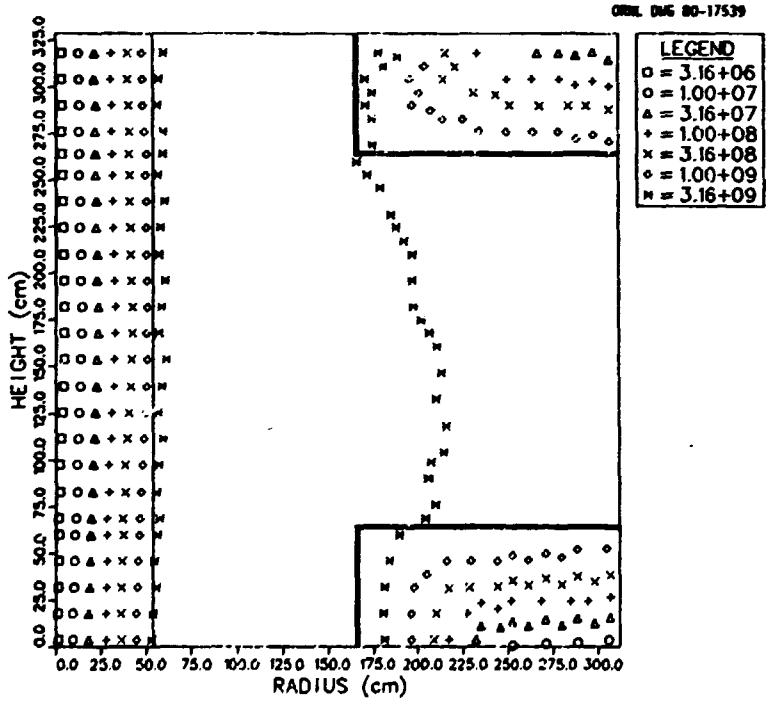

Fig. 45. Isoplot of the total neutron flux (cm^{-2}, s^{-1}) in the upflow GCFR inlet coolant duct region.

which shows an isoplot of the 24 full-power-year total neutron fluence in the vicinity of the main coolant inlet duct. The contours plotted for the 3.16×10^{18} cm^{-2} level show several spikes off the outer face of the plenum shield (at left in Fig. 44) which are angled in the direction of the coolant flow through channels. The figure shows that the fluence in the liner is at least 3.16×10^{18} cm^{-2}, with the possibility of a higher level. Upon examining the 2-D calculated fluence array and using linear interpolation to estimate a value on the inner surface of the liner, it was found that the maximum fluence in the liner was 5.5×10^{18} cm^{-2}. This would mean less than a factor of 2.0 margin between the maximum fluence in the liner and the design constraint for the liner. While the maximum fluence at the source surface appears to be 3.16×10^{18} cm^{-2}, this is not the maximum value due to the low-energy neutron flux buildup in the PCRV.

An isoplot of the total neutron flux is shown in Fig. 45. The strong variation in the total flux near the source plane as seen in Fig. 44 would have been missed completely with the plot shown in Fig. 45. The constant factor applied to the total flux to obtain the total fluence, not being a power of 10, does not result in the same contours being generated for both the total flux and total fluence unless the levels to be plotted are specified with the conversion factor in mind. Figure 45 does show that the total flux contours become smoother away from the source surface. Similar contours are observed in the PCRV.

The total 24 full-power-year neutron and gamma-ray dose isoplot is shown in Fig. 46. The 10^9 rd level is seen to extend well into the PCRV due to transport down the inlet coolant duct. However, the dose level drops exponentially as one moves away from the side of the duct. The maximum dose received at any prestressing tendon would depend on the proximity of the tendon to the coolant duct. Certainly, if a tendon abutted the duct it would experience the maximum allowable dose. At about 45 cm from either section of the liner the maximum dose appears to be about 3×10^8 rd or about a factor of 3 below the design constraint.

Other neutron flux plots are included in Appendix D.

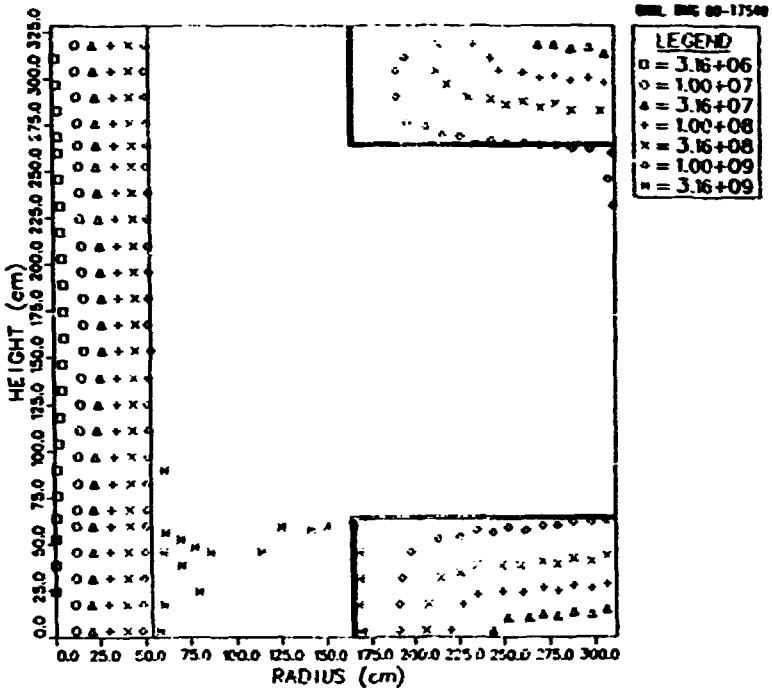

Fig. 46. Isoplot of the 24 full-power-year total neutron and gamma-ray dose (rd) in the Upflow GCFR inlet coolant duct region.

6. REMAINING ISSUES

It is believed that the major parameters have already been considered in previous shielding calculations. However, the combination of the effects of several parameters which have not been studied might be enough to raise some radiation levels above the corresponding design constraints.

One parameter not studied is thermal neutron upscattering in graphite and the PCRV. Since the inclusion of upscattering tends to raise the thermal flux level above that with no upscattering considered, there should be an increase in the total neutron fluence in the PCRV liner and an increase in the dose to the tendon lubricant. The upscattering effect could be quite substantial.

A second item not considered is the change in the water content of the PCRV near the liner as a function of time. With reduced water

content in the PCRV, fast neutrons will penetrate a greater distance into the PCRV and could greatly increase the dose to the tendon lubricant.

A third item not considered is the effect of the liner cooling tubes on the dose to the tendon lubricant. The tubes would mainly serve as a source for high energy capture gamma-rays which could make large contributions to the dose to the tendon lubricant. The water within the cooling tubes may also serve as a neutron thermalizer which could enhance the iron capture gamma rays.

Finally, an evaluation needs to be made of the neutron source for several operating conditions (burnup, control rod position, etc) and of the uncertainties in the calculated fluxes and responses.

7. SUMMARY

Results from the analysis of the GCFR Conceptual Shielding Configuration III have been presented. The results included the effects of prompt neutrons and gamma rays from fission as well as the effects of gamma-rays from fission products. Several activities (flux, dose, radiation heating, reaction rate) were calculated and examined in the light of the design constraints placed on the particular activity. In most cases it was found that the maximum calculated activities were reasonably well below the design limits. It was found that the neutron fluence in the core barrel would exceed the design constraint without the proposed solution of cooling it with inlet plenum gas, a solution which effectively raises the design constraint by a factor of 10. The total neutron fluence in the grid plate was within 30% of the design constraint. Other calculated activities were generally well below the constraints, enough so that calculational and data uncertainties would not cause the adjusted calculated activity to exceed the design constraint. It was also noted that in two instances where boundary sources were corrected for radiation streaming, the follow on calculation indicated that the total neutron fluence exceeded the constraint in either the PCRV liner or the core barrel. It was explained that the fluences were probably not indicative of the true fluences, but were the result

of an overcorrection for thermal neutron streaming in the region (streaming correction factors for the core mid-plane and axial centerline were applied in peripheral regions also).

Work on the preliminary and final analyses of the plenum flow-through shields was presented. Calculations were performed by discrete ordinates and Monte Carlo on cell mockups of the flow-through shields. The results indicated the shield designs reduced the neutron fluence by factors of 30 or better while only a factor of 3 was needed in the upper plenum, and a factor of 10 was needed in the lower plenum. It was clear that each of the shield designs was very effective in reducing the neutron fluence incident on it, such that the fluence in the PCRV liner would be within the acceptable limit.

Finally, a list of items which should be considered before completion of the shield design was presented. The items are aimed at determining the maximum value for a particular activity in a given region. They are also aimed at reducing the sources of uncertainty in the calculated activities.

REFERENCES

1. C. O. Slater, E. T. Tomlinson, L. R. Williams, "Analysis of the Initial Shielding Design for the Upflow Gas-Cooled Fast Reactor (GCFR)," ORNL/TM-7246 (May 1980).

2. GA Internal Correspondence: R. G. Perkins to C. J. Hamilton, "Shielding Core Model C," October 10, 1979.

3. Letter from C. A. Rouse to C. O. Slater, October 9, 1979. Included preliminary plenum flow-through shield designs.

4. Letter from C. A. Rouse to C. O. Slater, December 14, 1979. Included preliminary conceptual shielding configuration III design information.

5. Letter from C. A. Rouse to C. O. Slater, Jan. 18, 1980. Included GA drawing of the overall conceptual shielding configuration III design.

6. Letter from C. A. Rouse to C. O. Slater, May 5, 1980. Included information on the selected designs for the upper and lower plenum flow-through shields.

7. Letter from C. A. Rouse to C. O. Slater, May 14, 1980. Included a revised conceptual shielding configuration III design.

8. Project staff, "Gas-Cooled Fast Breeder Reactor Quarterly Progress Report for the period Feb. 1, 1979 through April 30, 1979," General Atomic Company Report GA-A15406, May 1979.

9. W. A. Rhoades, D. B. Simpson, R. L. Childs, and W. W. Engle, Jr., "The DOT-IV Two-Dimensional Discrete Ordinates Transport Code with Space-Dependent Mesh and Quadrature," ORNL/TM-6529 (Jan. 1979).

10. O. W. Hermann, "ORIGEN-S" in "SCALE: A Modular Code System for Performing Standardized Computer Analyses for Licensing Evaluation," (to be published).

11. S. Glasstone and M. C. Edlund, The Elements of Nuclear Reactor Theory, D. Van Nostrand Company, Inc., 1952.

12. M. T. Simnad, "Shielding and Control Materials for the Gas-Cooled Fast Breeder Reactor," General Atomic Company Report GA-A14478, December 1977.

13. Project Staff, "Gas-Cooled Fast Breeder Reactor Quarterly Progress Report for the Period August 1, 1979 through October 31, 1979, General Atomic Company Report GA-A15628 (November 1979).

14. W. W. Engle, Jr., "A User's Manual for ANISN: A One-Dimensional Discrete Ordinates Transport Code with Anisotropic Scattering," Union Carbide Nuclear Division Report K-1693 (March 1967).

15. M. Benedict, Nuclear Chemical Engineering, McGraw-Hill Book Company, Inc., New York, 1957.

16. Project Staff, "Gas-Cooled Fast Breeder Reactor Quarterly Progress Report for the Period May 1, 1978 Through July 31, 1978, General Atomic Company Report GA-A15054, August 1978.

17. R. E. Maerker and F. J. Muckenthaler, "Final Report on a Benchmark Experiment for Neutron Transport Through Iron and Stainless Steel, ORNL-4892 (April 1974).

18. M. B. Emmett, "The MORSE Monte Carlo Radiation Transport Code System," ORNL-4972 (February 1975).

19. M. L. Gritzner, W. W. Engle, Jr., W. A. Rhoades, D. R. Vondy, and and L. R. Williams, "FACT: A Computer Code to Process the Neutron and Gamma Angular Flux and Fold Regular and Adjoint Results on a Coupling Surface for Response Analysis," draft report.

Appendix A

Isoplots of Additional Activities for the Conceptual Upflow GCFR Mid-Level Regions

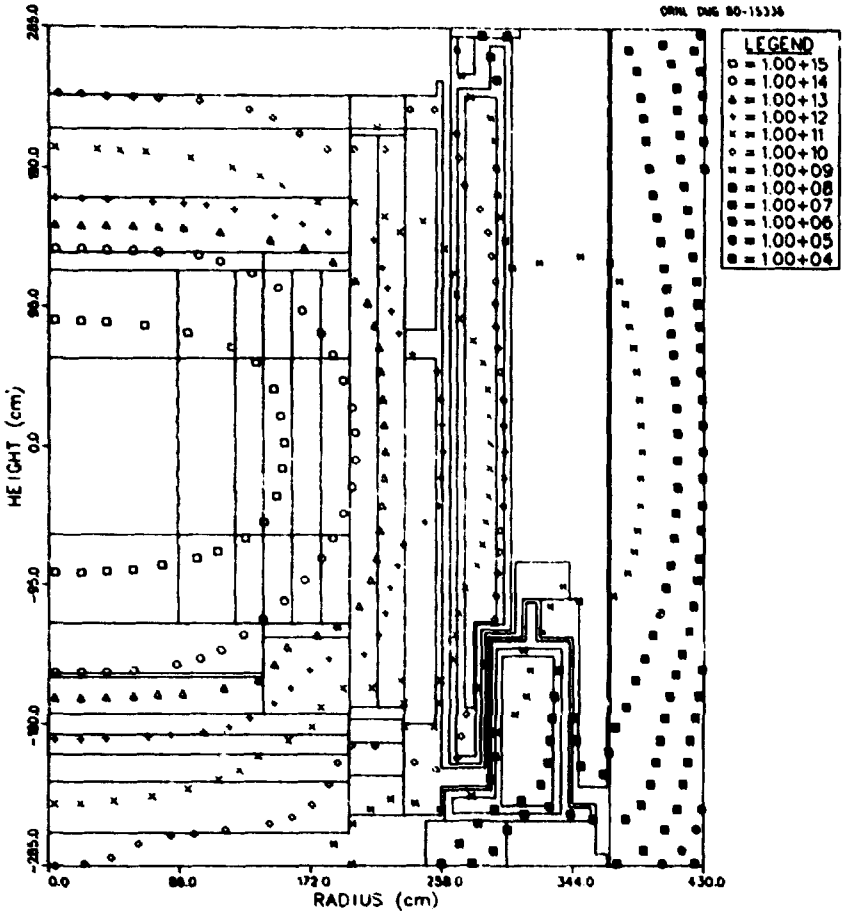

Fig. A-1. Isoplot of the total neutron flux ($cm^{-2} \cdot s^{-1}$) in the Conceptual Upflow GCFR Mid-level regions.

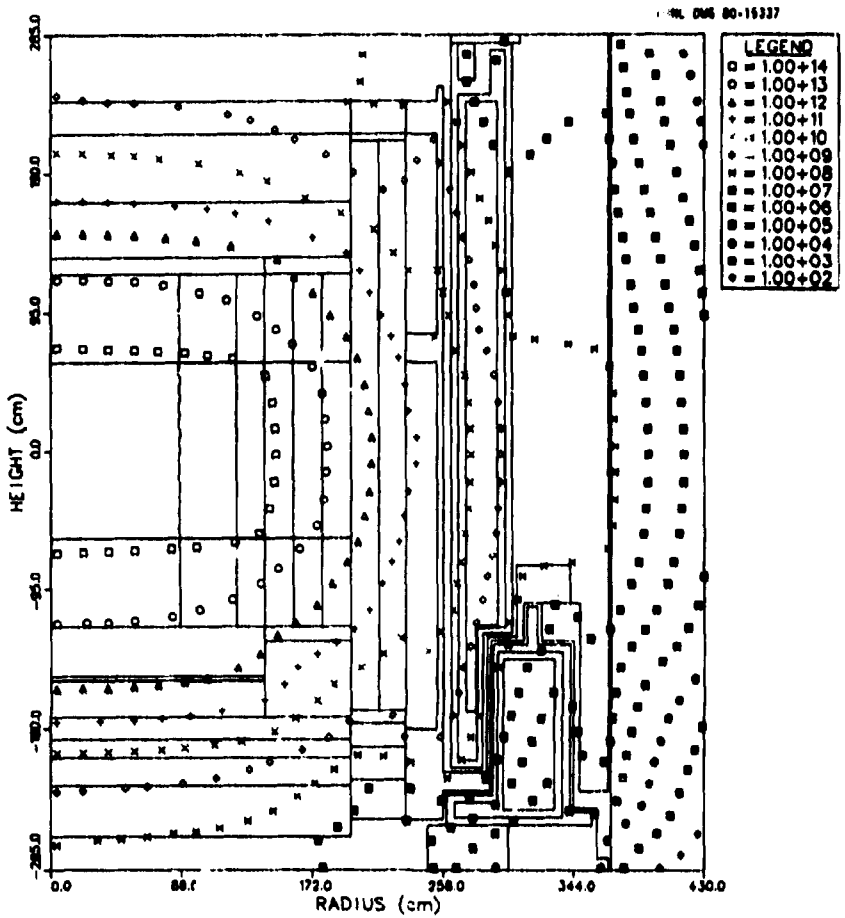

Fig. A-2. Isoplot of the fast (E > 1.0 MeV) neutron flux ($cm^{-2} \cdot s^{-1}$) in the Conceptual Upflow GCFR mid-level regions.

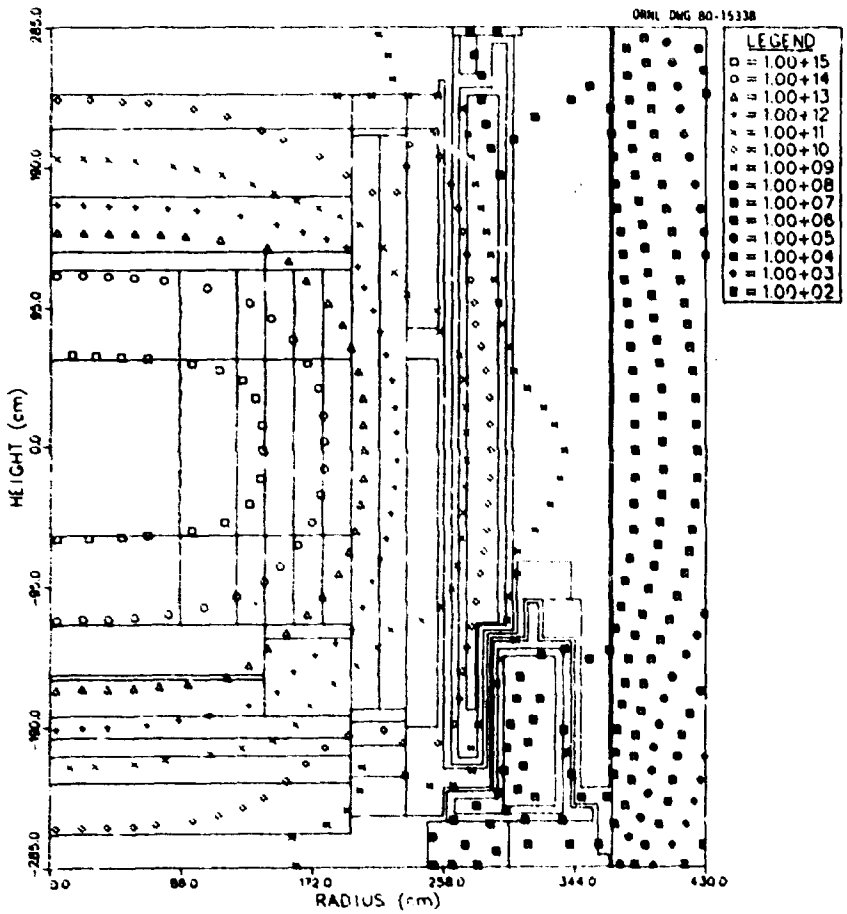

Fig. A-3. Isoplot of the fast (E > 0.1 MeV) neutron flux ($cm^{-2} \cdot s^{-1}$) in the Conceptual Upflow GCFR mid-level regions.

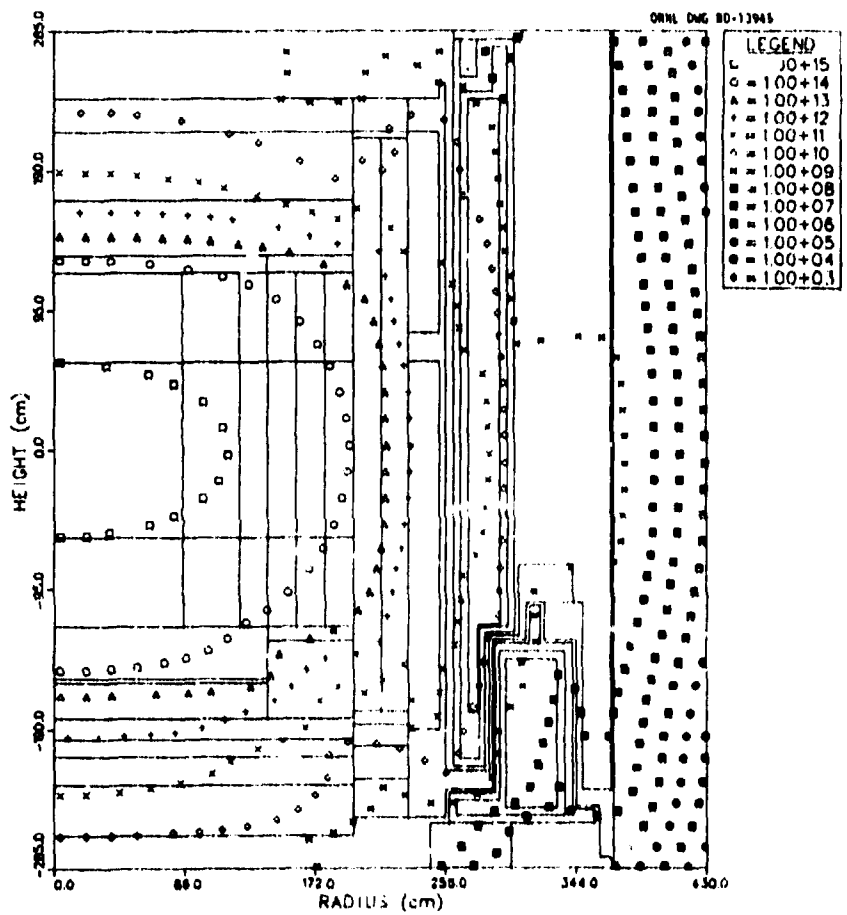

Fig. A-4. Isoplot of the intermediate (2.38 eV < E < 0.1 MeV) neutron flux ($cm^{-2} \cdot s^{-1}$) in the Conceptual Upflow GCFR mid-level regions.

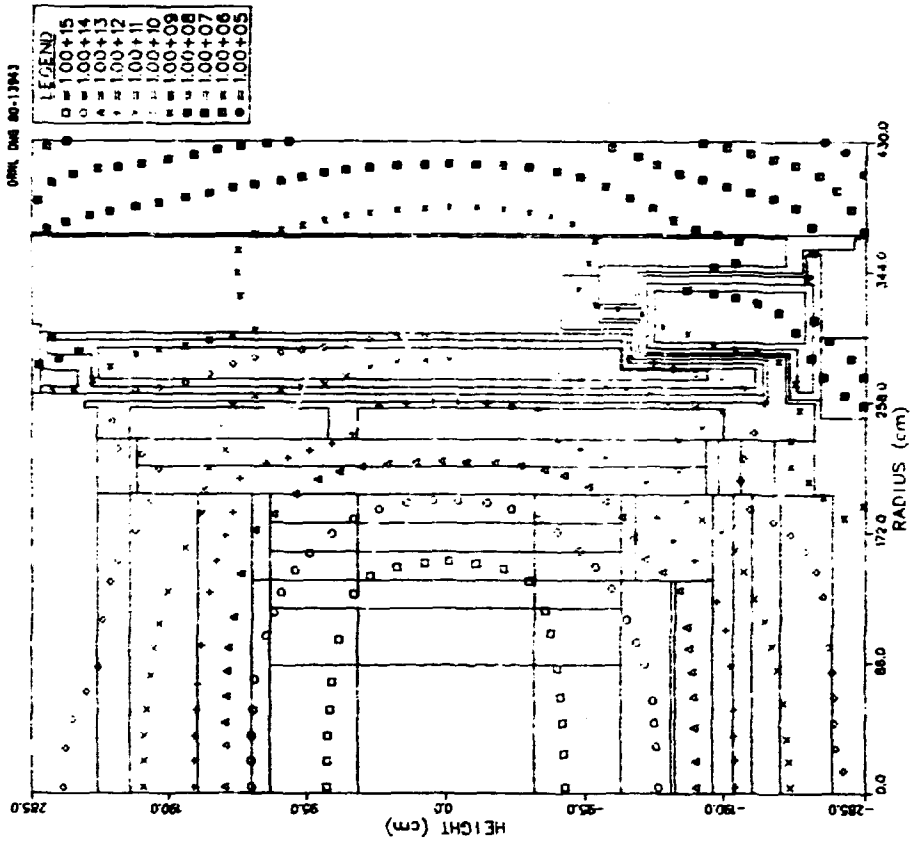

Fig. A-6. Isoplot of the total 24 full-power-year tissue dose (rd) in the Conceptual Upflow GCFR mid-level regions.

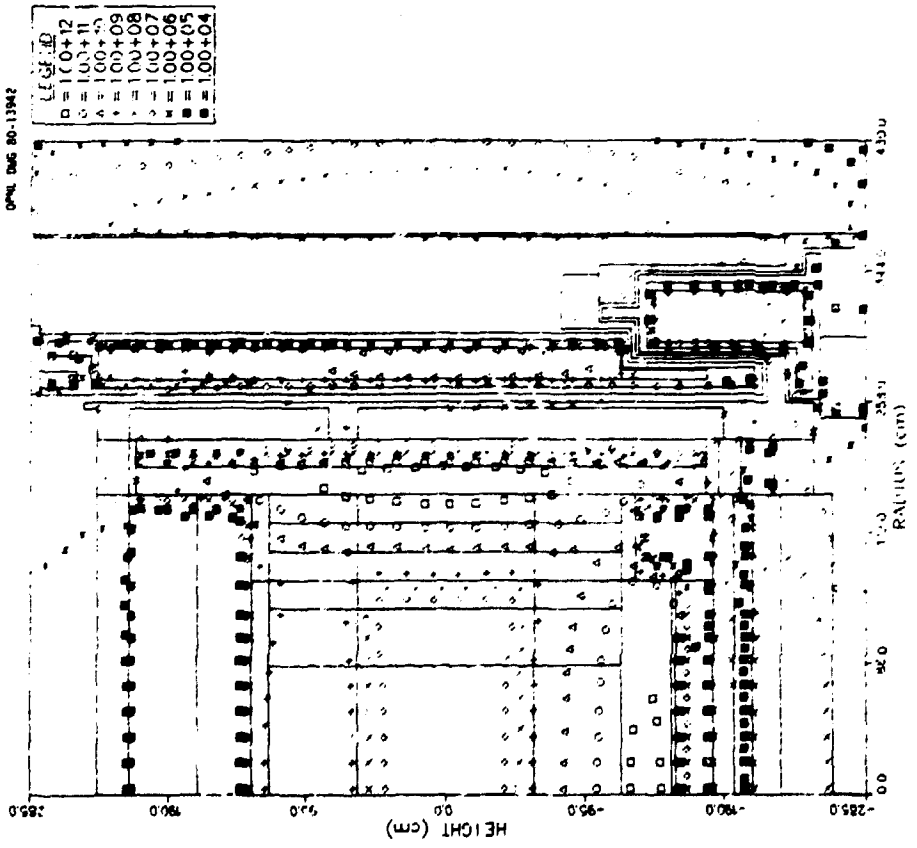

Fig. A-5. Isoplot of the thermal ($E < 2.38$ eV) neutron flux ($cm^{-2} \cdot s^{-1}$) in the Conceptual Upflow GCFR mid-level regions.

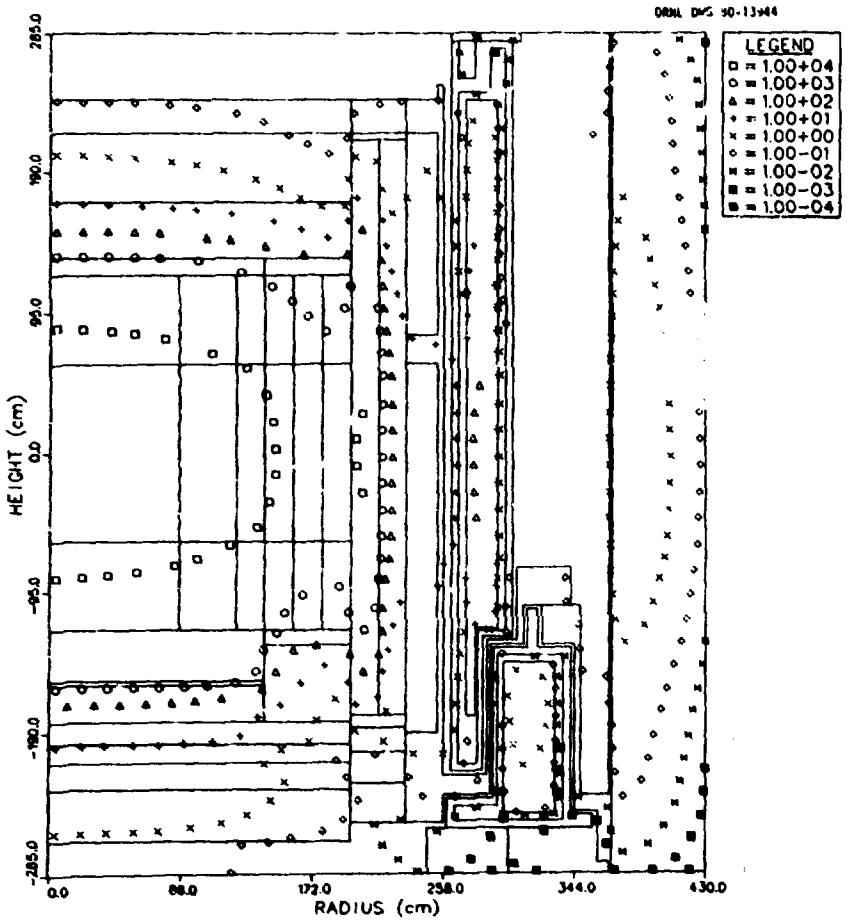

Fig. A-7. Isoplot of the total heating (mW/cm^3) in boronated graphite in the Conceptual Upflow GCFR mid-level regions.

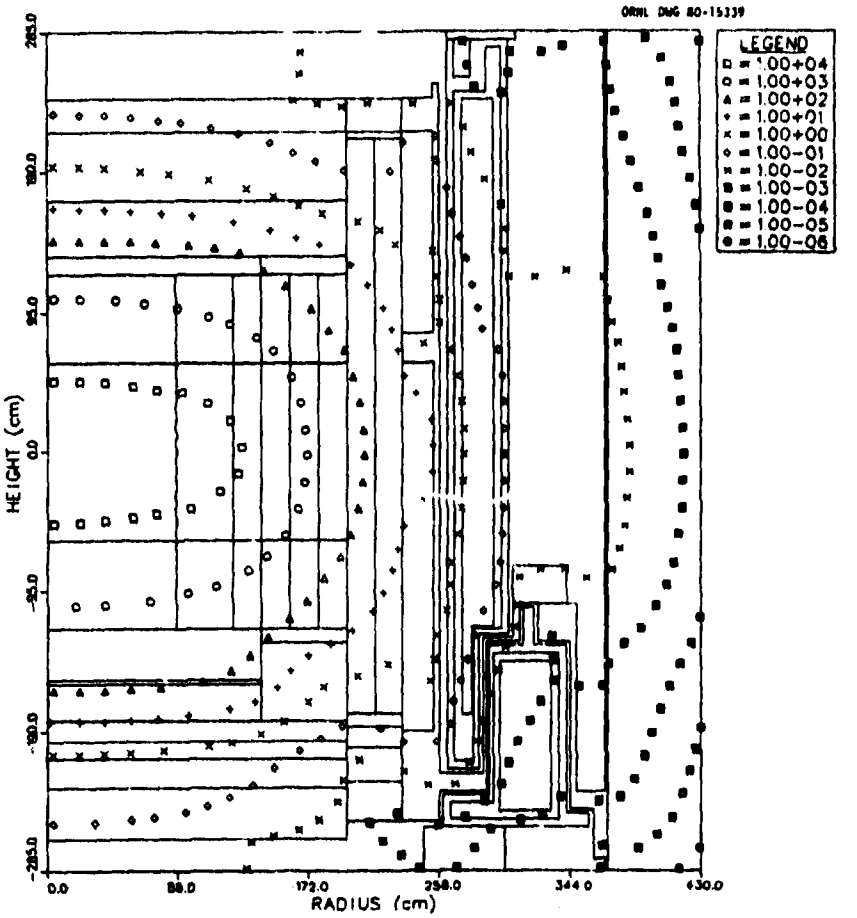

Fig. A-8. Isoplot of the total heating (mW/cm^3) in graphite in the Conceptual Upflow GCFR mid-level regions.

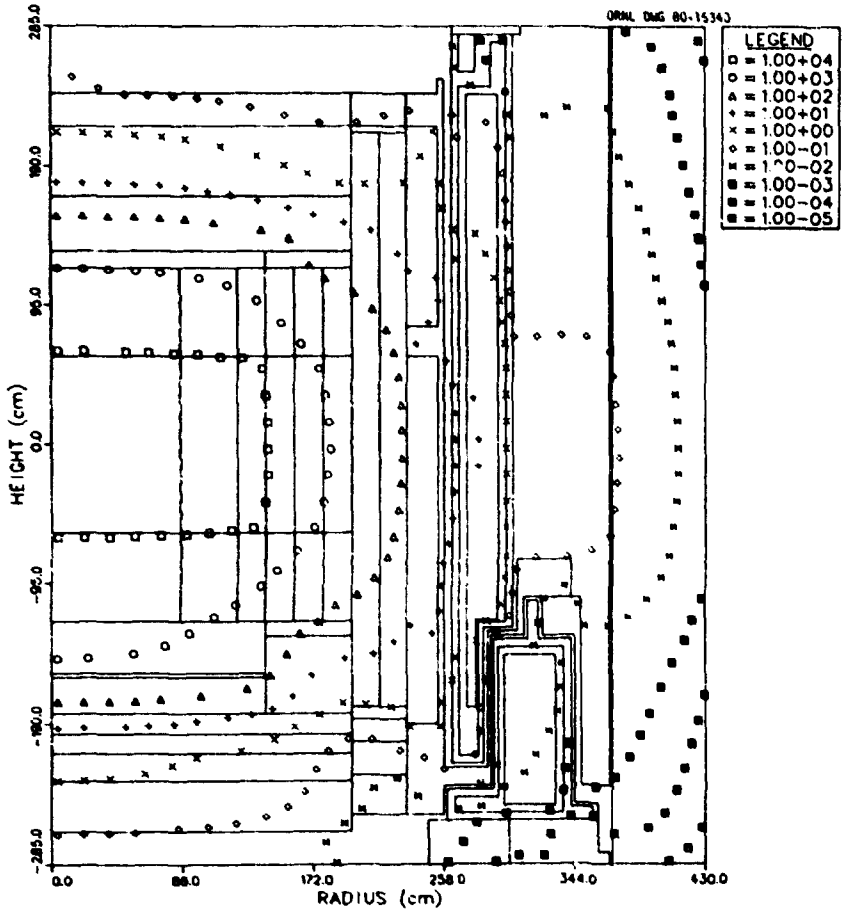

Fig. A-9. Isoplot of the total heating (mW/cm^3) in SS316 in the Conceptual Upflow GCFR mid-level regions.

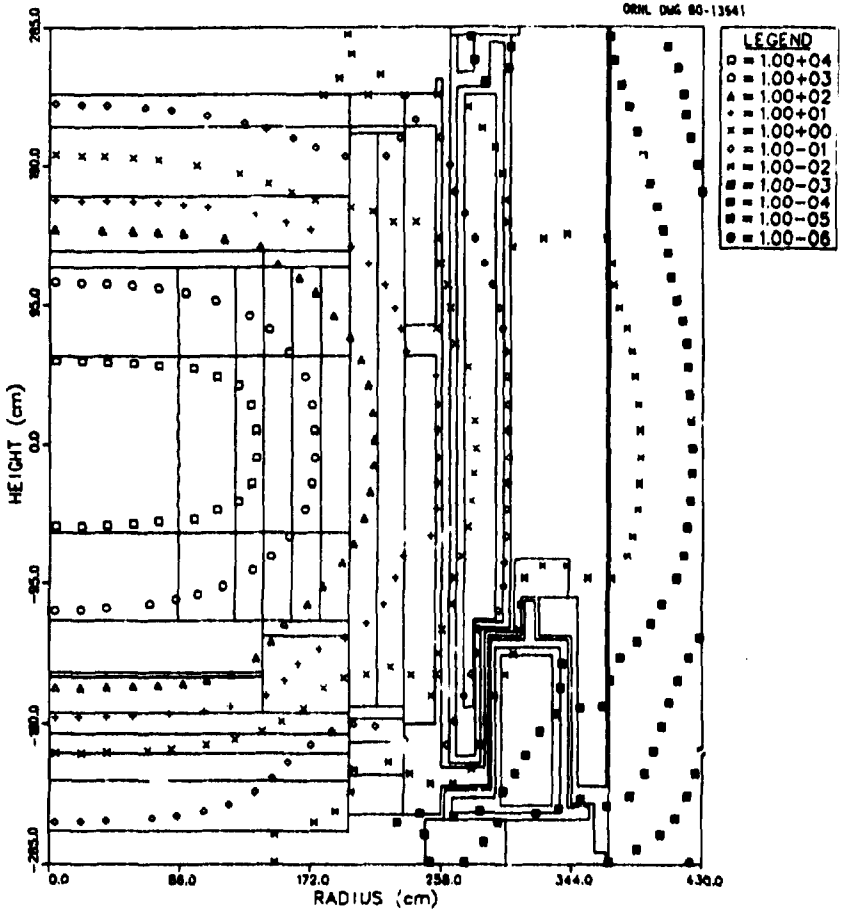

Fig. A-10. Isoplot of the total heating (mW/cm^3) in ordinary concrete in the Conceptual Upflow GCFR mid-level regions.

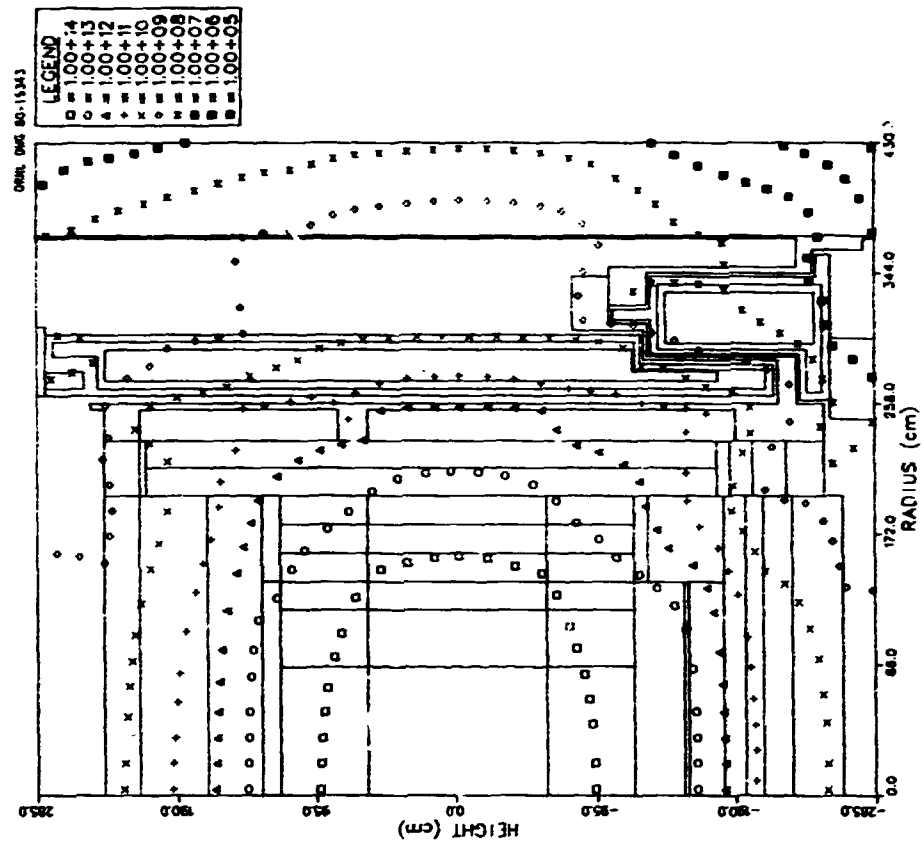

Fig. A-12. Isoplot of the total gamma-ray energy flux ($MeV \cdot cm^{-2} \cdot s^{-1}$) in the Conceptual Upflow GCFR mid-level regions.

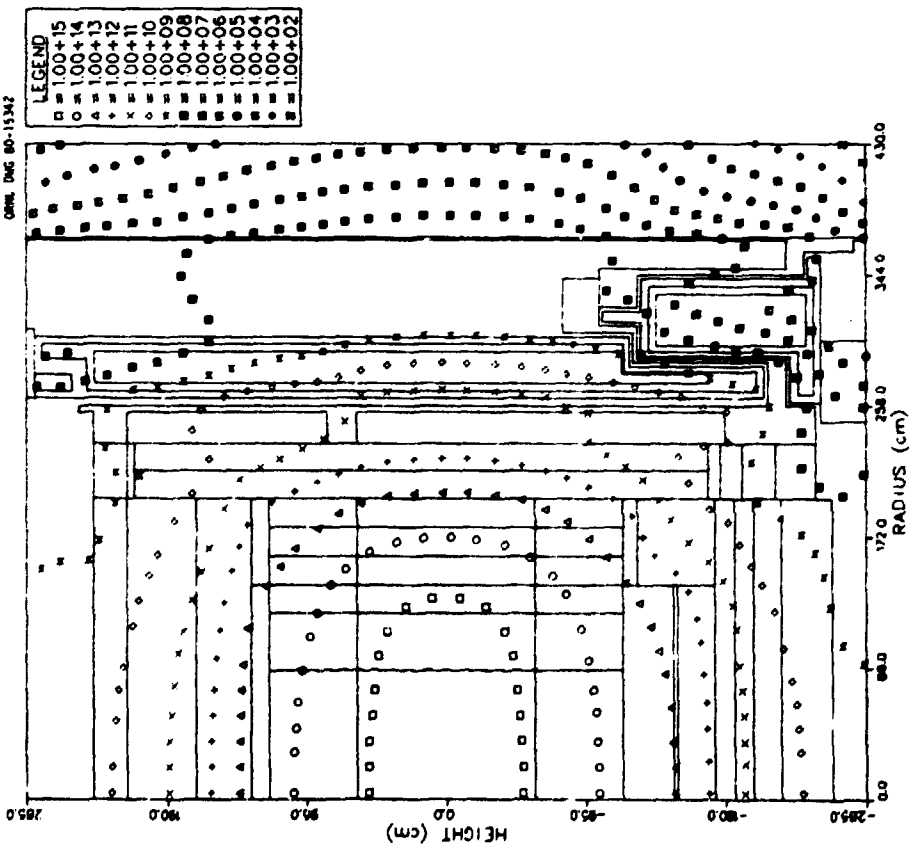

Fig. A-11. Isoplot of the total neutron energy flux ($MeV \cdot cm^{-2} \cdot s^{-1}$) in the Conceptual Upflow GCFR mid-level regions.

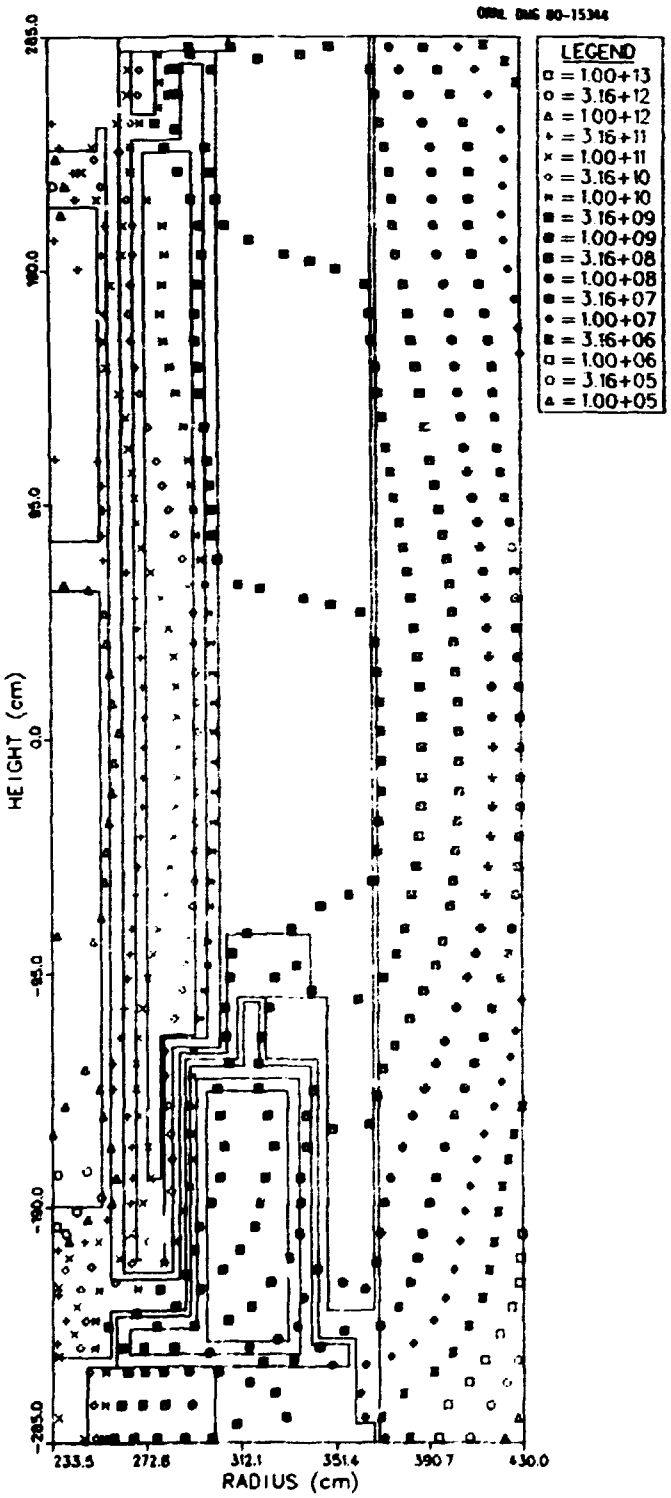

Fig. A-13. Isoplot of the streaming-corrected 24 full-power-year total tissue dose (rd) in the Conceptual Upflow GCFR mid-level regions.

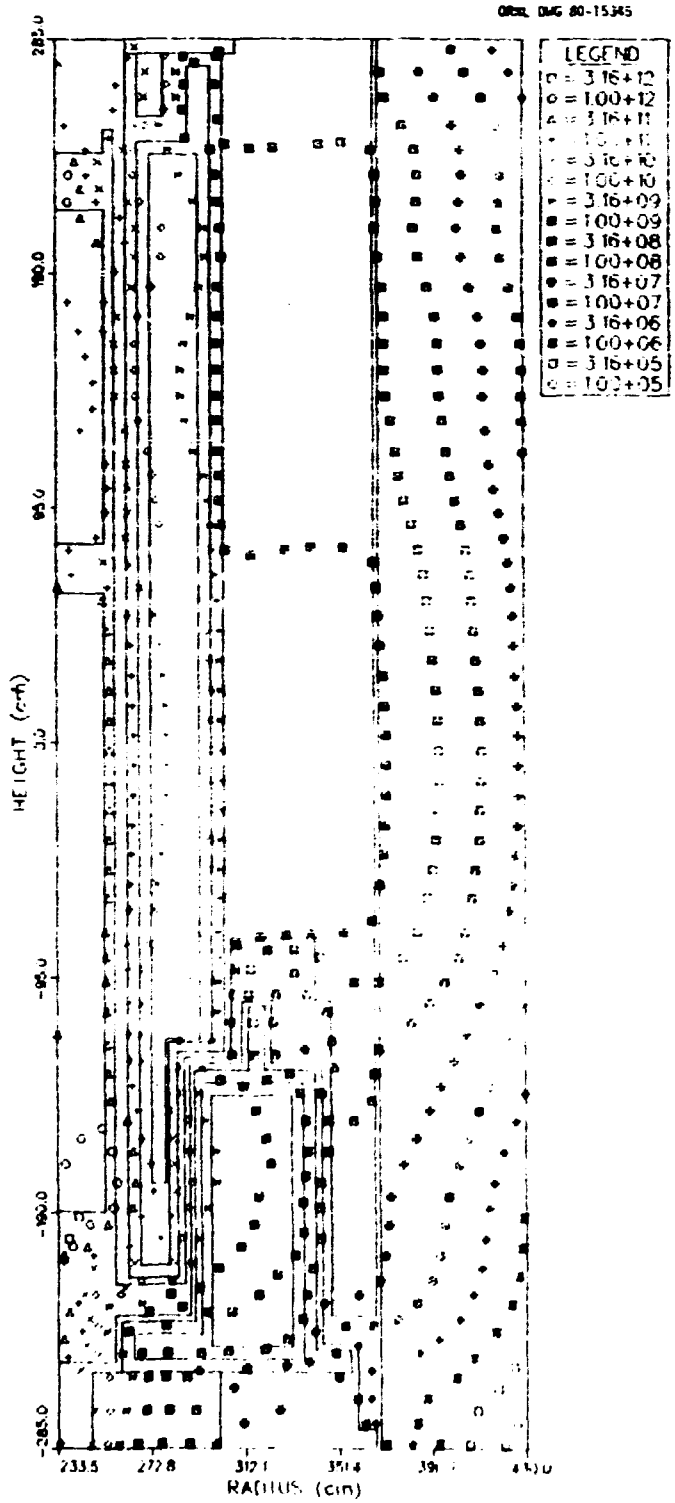

Fig. A-14. Isoplot of the streaming-corrected 24 full-power-year gamma-ray tissue dose (rd) in the Conceptual Upflow GCFR mid-level regions.

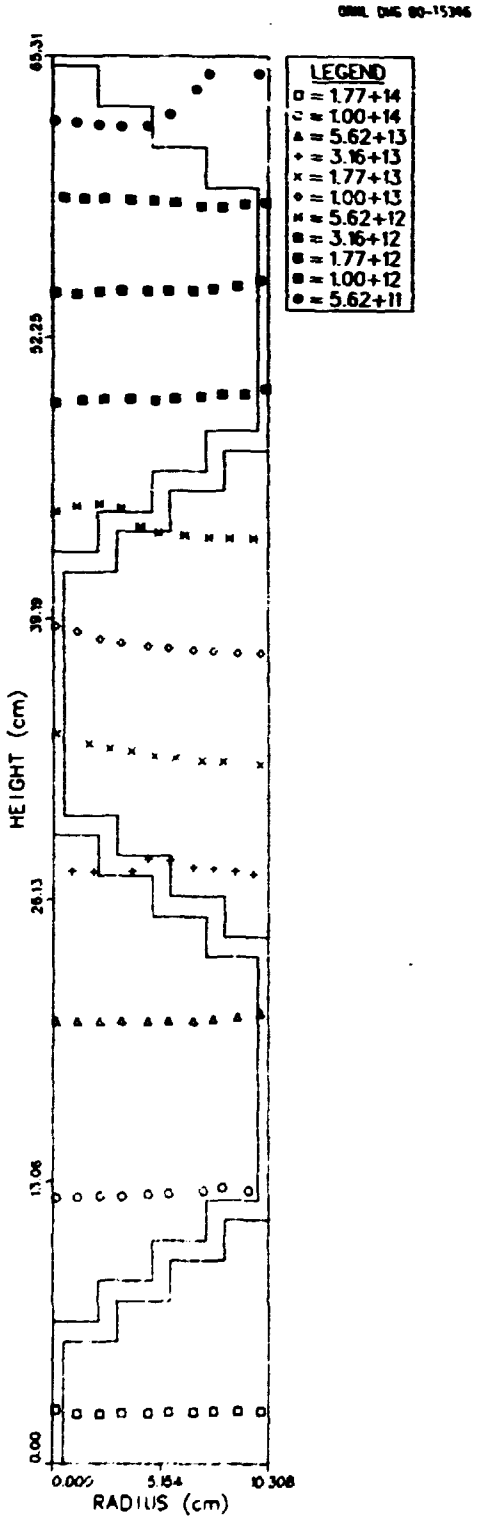

Fig. A-15. Isoplot of the fast (E > 0.1 MeV) neutron flux ($cm^{-2} \cdot s^{-1}$) in an X-Y heterogeneous mockup of the Conceptual Upflow GCFR mid-level radial regions.

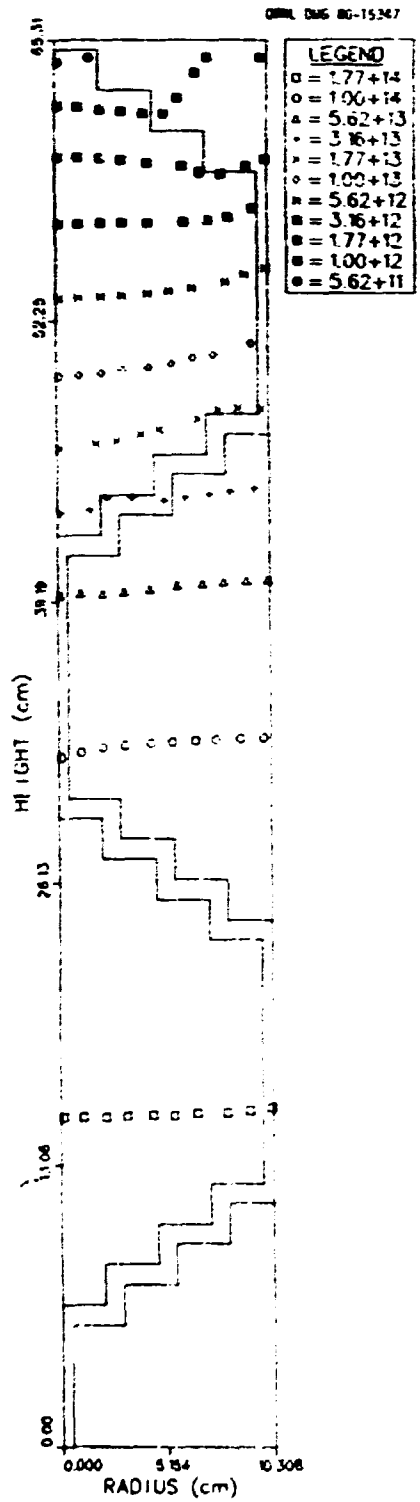

Fig. A-16. Isoplot of the intermediate (2.38 eV < E < 0.1 MeV) neutron flux ($cm^{-2} \cdot s^{-1}$) in an X-Y heterogeneous mockup of the Conceptual Upflow GCFR mid-level radial regions.

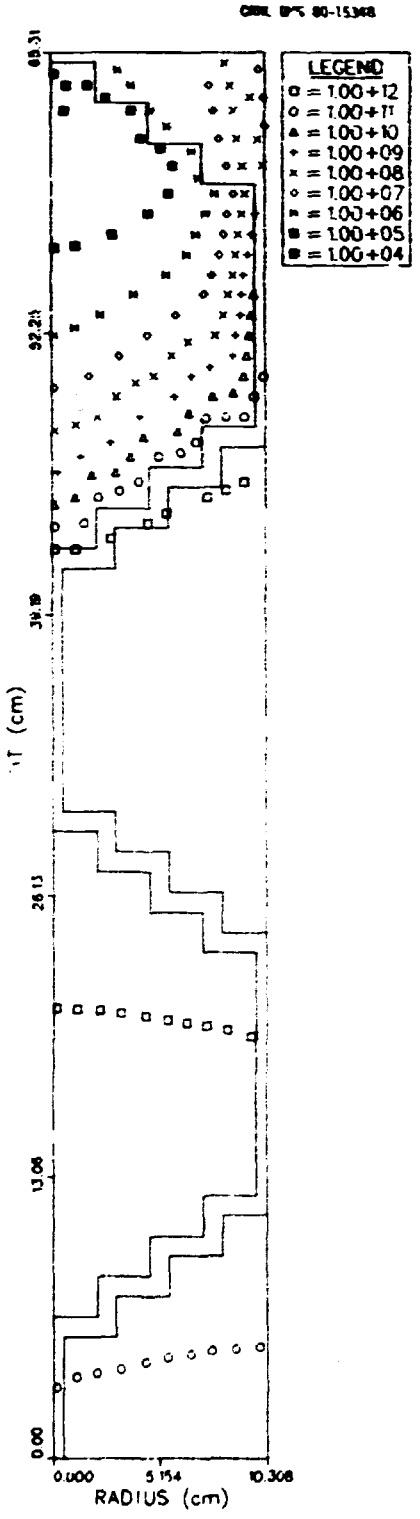

Fig. A-17. Isoplot of the thermal (E < 2.38 eV) neutron flux ($cm^{-2} \cdot s^{-1}$) in an X-Y heterogeneous mockup of the Conceptual Upflow GCFR mid-level radial regions.

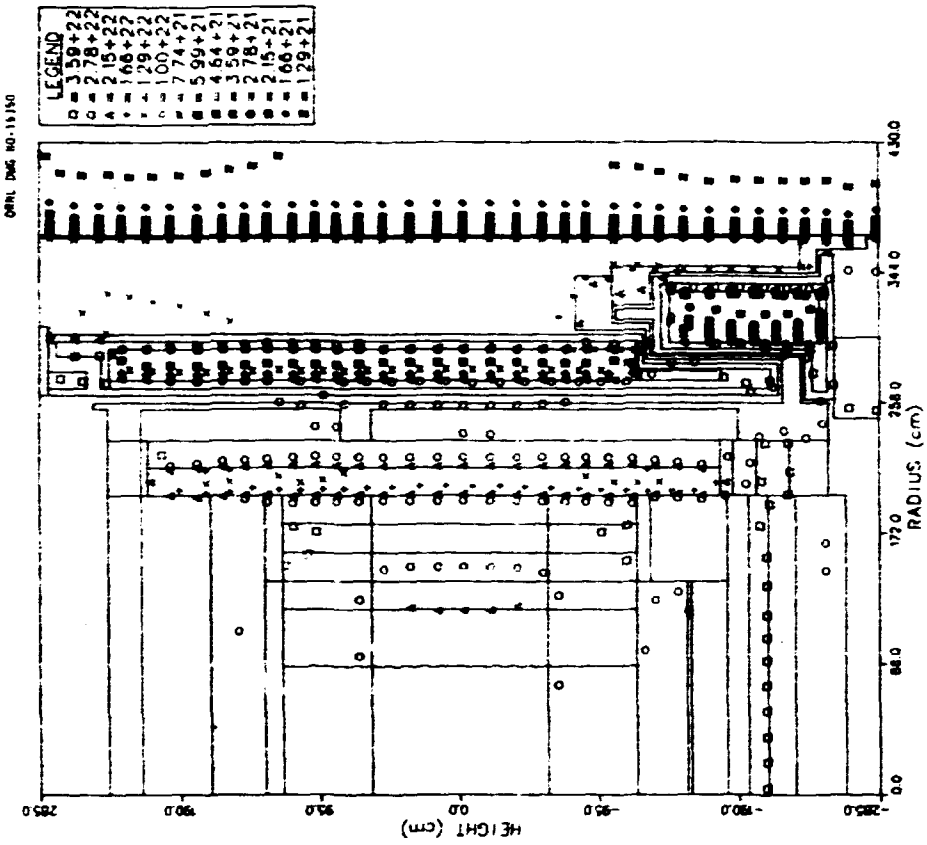

Fig. A-19. Isoplot of the permissible total neutron fluence for a 5% residual uniform elongation in SS316 in the Conceptual Upflow GCFR mid-level regions. (Results based on the conservative response function.)

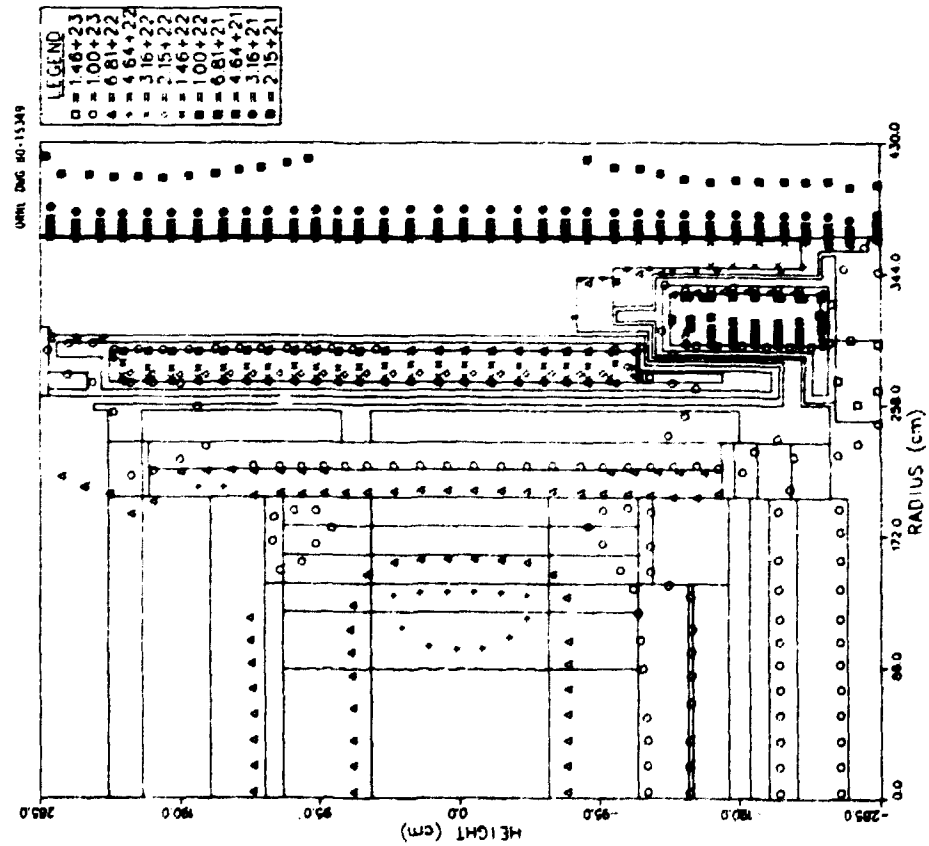

Fig. A-18. Isoplot of the permissible total neutron fluence for a 5% residual uniform elongation in SS316 in the Conceptual Upflow GCFR mid-level regions. (Results based on the nominal response function.)

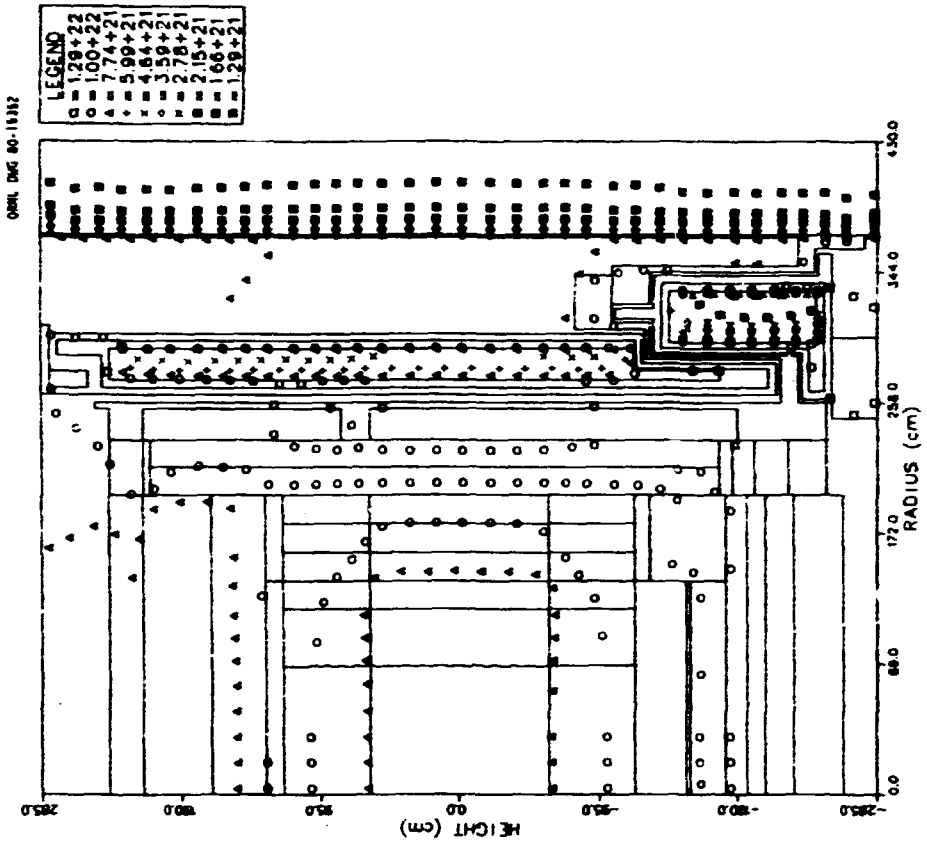

Fig. A-21. Isoplot of the permissible total neutron fluence for a 10% residual uniform elongation in SS316 in the Conceptual Upflow GCFR mid-level regions. (Results based on the conservative response function.)

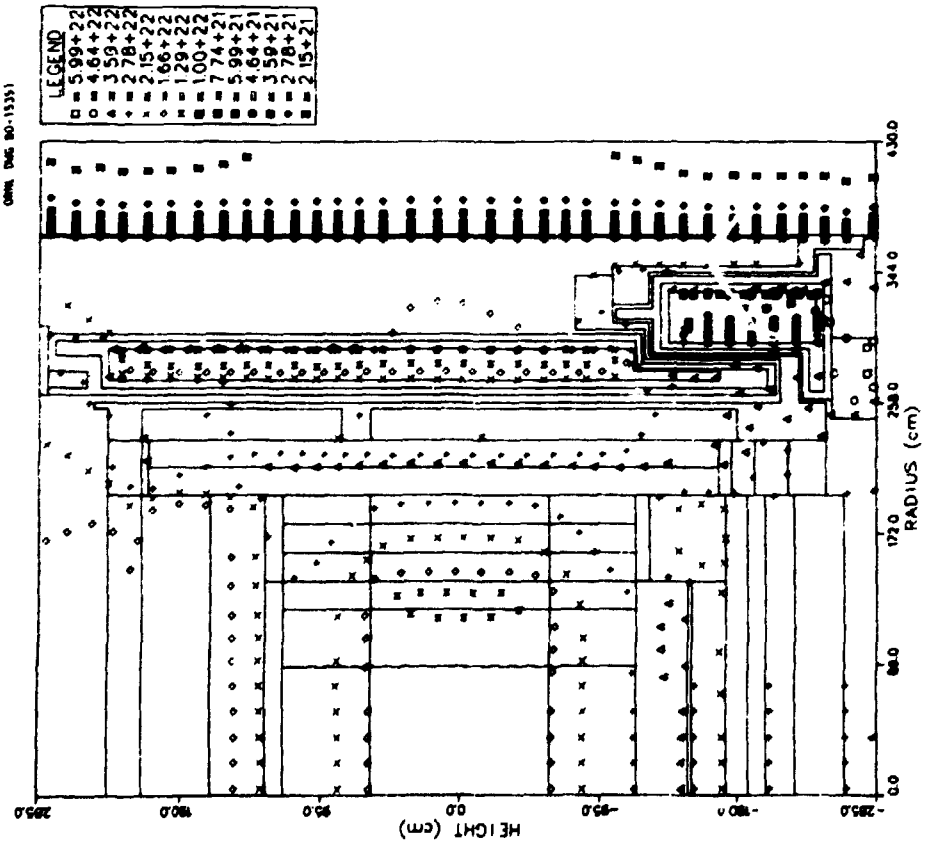

Fig. A-20. Isoplot of the permissible total neutron fluence for a 10% residual uniform elongation in SS316 in the Conceptual Upflow GCFR mid-level regions. (Results based on the nominal response function.)

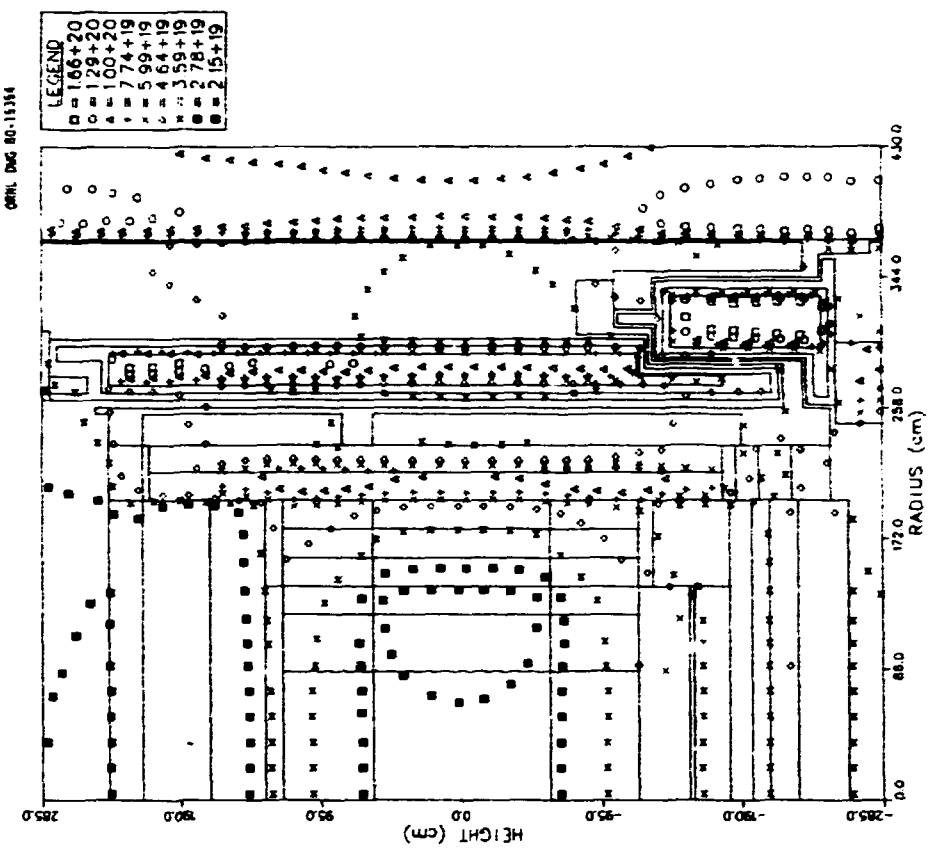

Fig. A-23. Isoplot of the permissible neutron fluence for a PCRV liner nil ductility temperature shift of 75°C for the Conceptual Upflow GCFR mid-level regions.

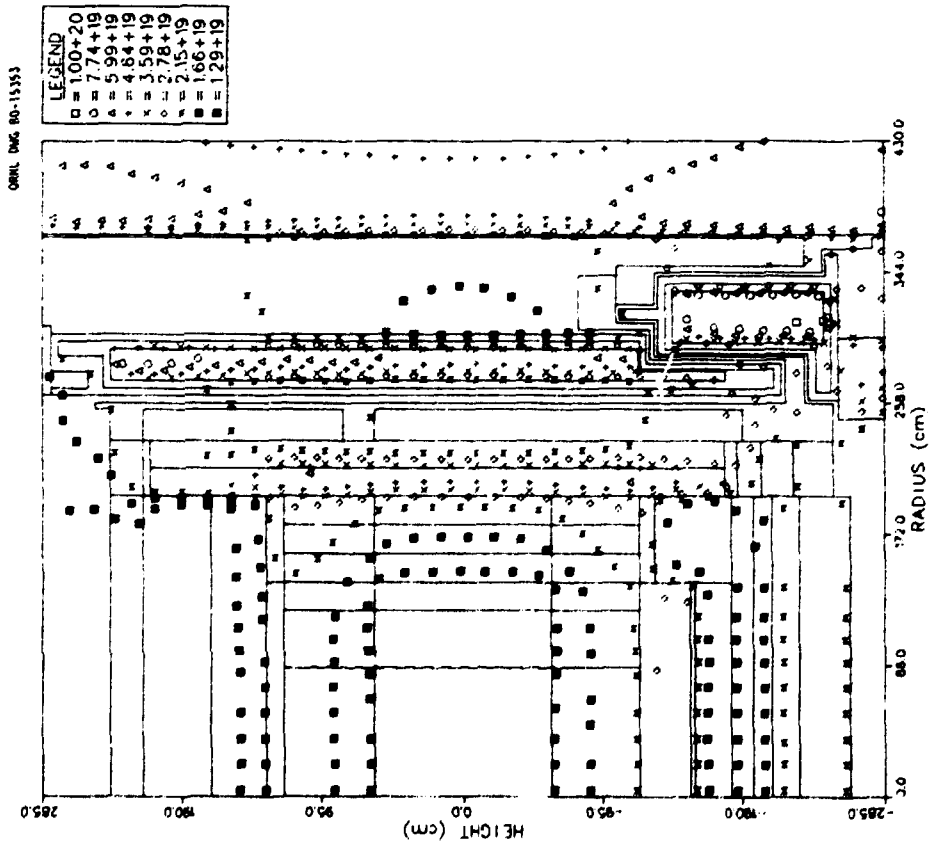

Fig. A-22. Isoplot of the permissible neutron fluence for a PCRV liner nil ductility temperature shift of 47°C for the Conceptual Upflow GCFR mid-level regions.

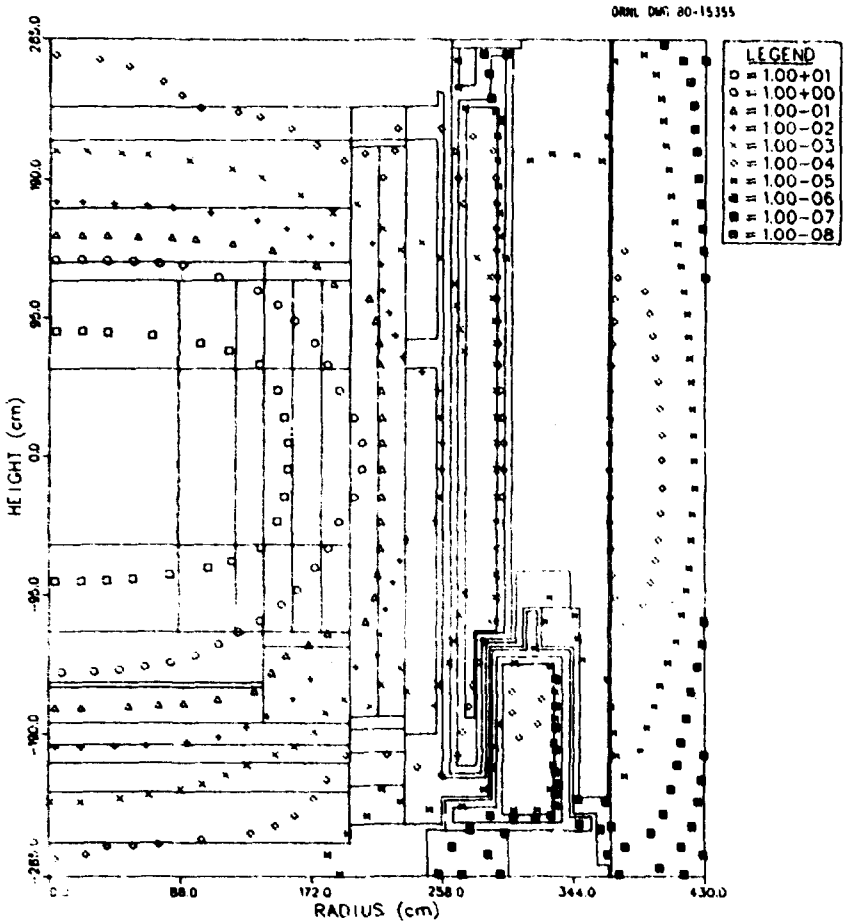

Fig. A-24. Isoplot of the fraction of the permissible neutron fluence received in the Conceptual Upflow GCFR mid-level regions based on the nominal 5% residual uniform elongation response function for SS316.

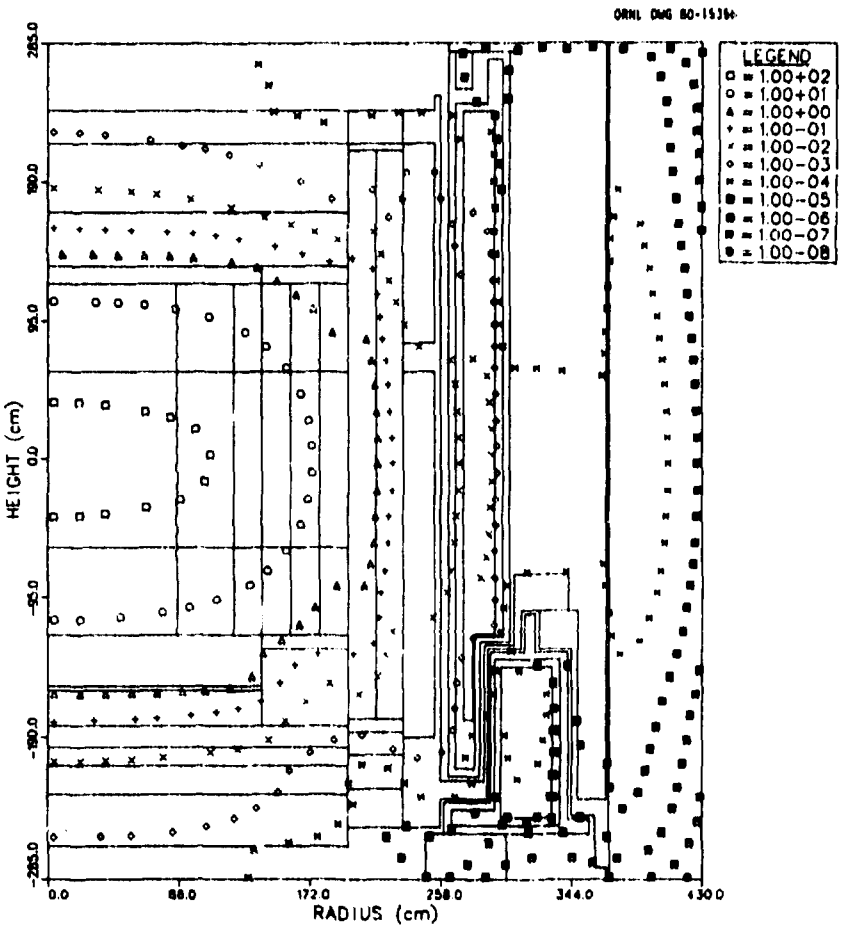

Fig. A-25. Isoplot of the fraction of the permissible neutron fluence received in the Conceptual Upflow GCFR mid-level regions based on the conservative 5% residual uniform elongation response function for SS316.

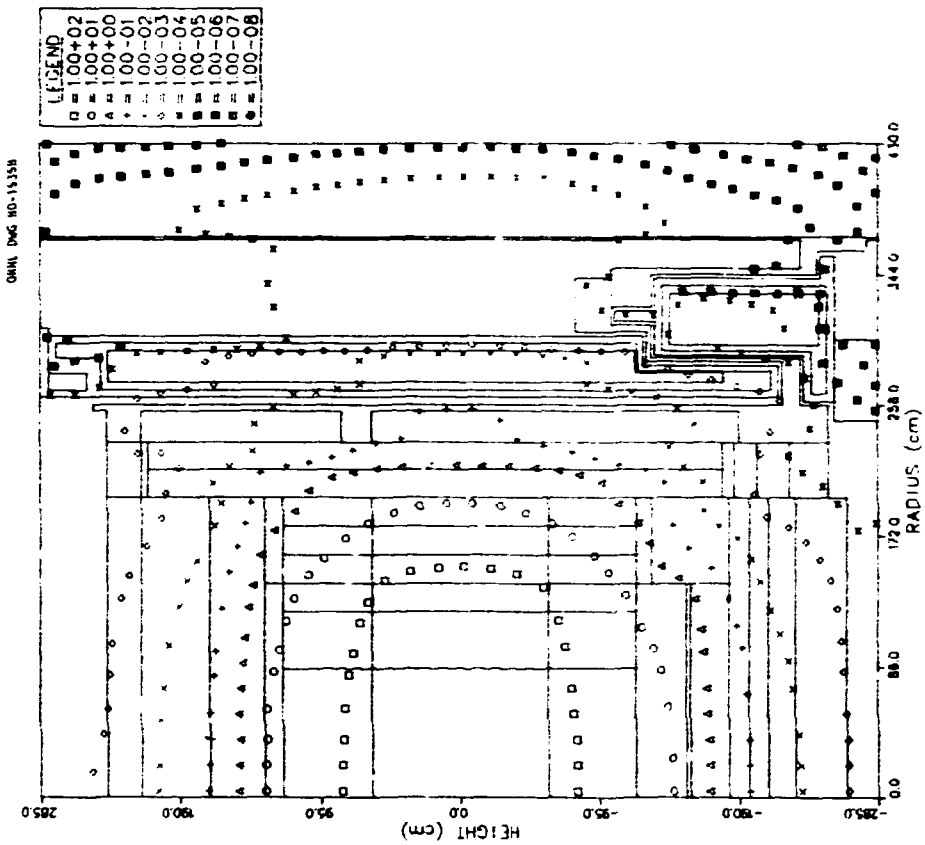

Fig. A-26. Isoplot of the fraction of the permissible neutron fluence received in the Conceptual Upflow GCFR mid-level regions based on the nominal 10% residual uniform elongation response function for SS316.

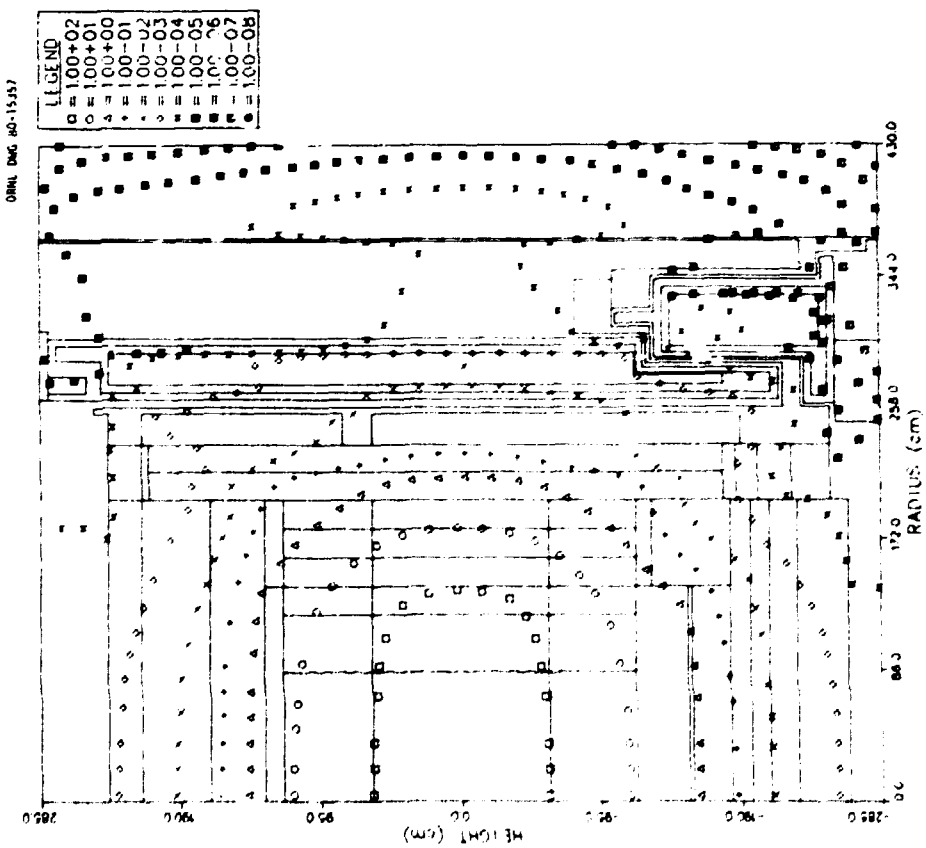

Fig. A-27. Isoplot of the fraction of the permissible neutron fluence received in the Conceptual Upflow GCFR mid-level regions based on the conservative 10% residual uniform elongation response function for SS316.

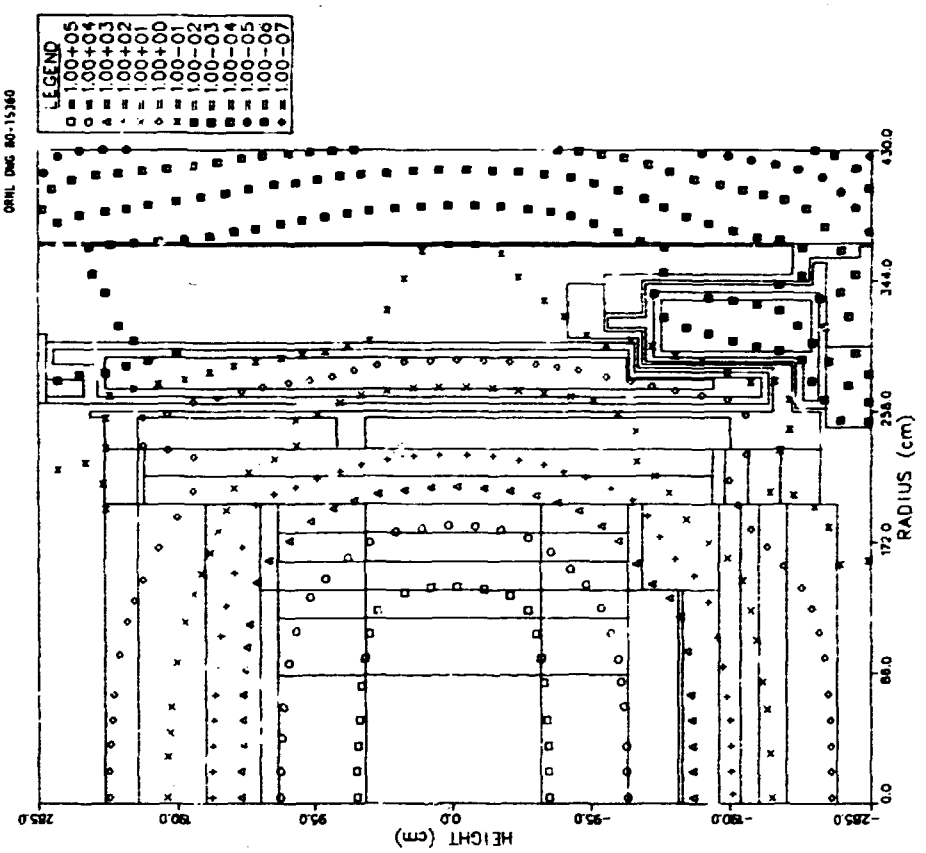

Fig. A-29. Isoplot of the fraction of the permissible neutron fluence received in the Conceptual Upflow GCFR mid-level regions based on the PCRV liner 75°C nil ductility temperature shift response function.

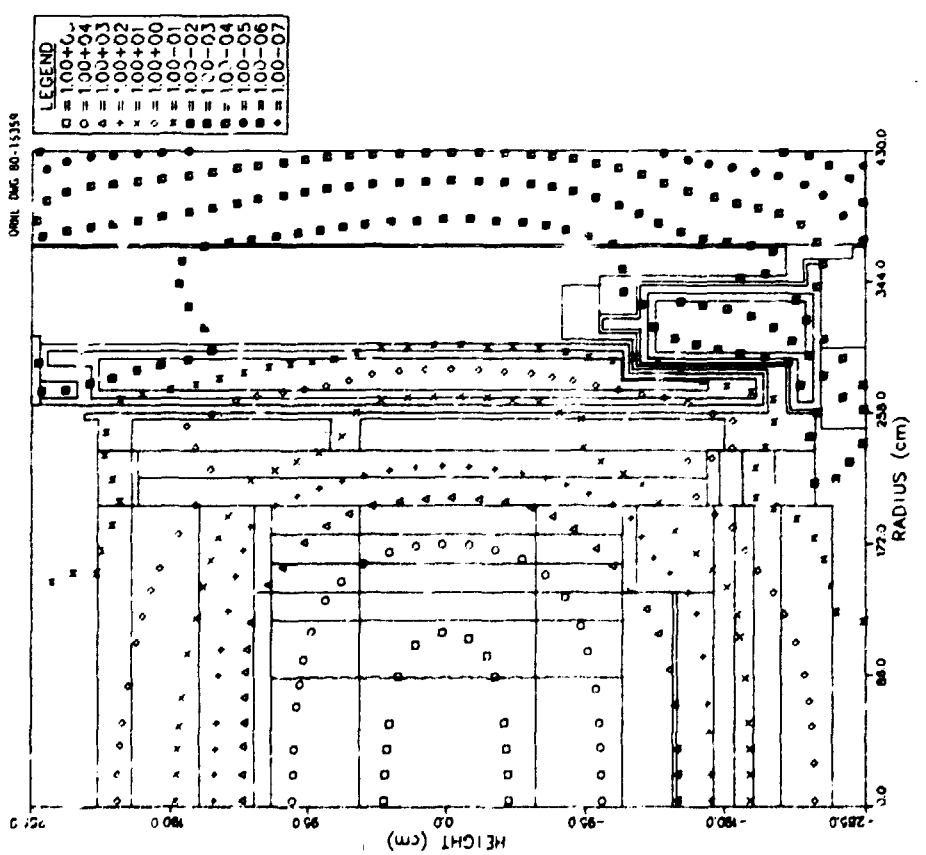

Fig. A-28. Isoplot of the fraction of the permissible neutron fluence received in the Conceptual Upflow GCFR mid-level regions based on the PCRV liner 47°C nil ductility temperature shift response function.

Appendix B

Isoplots of Additional Activities for the Conceptual Upflow GCFR Upper Regions

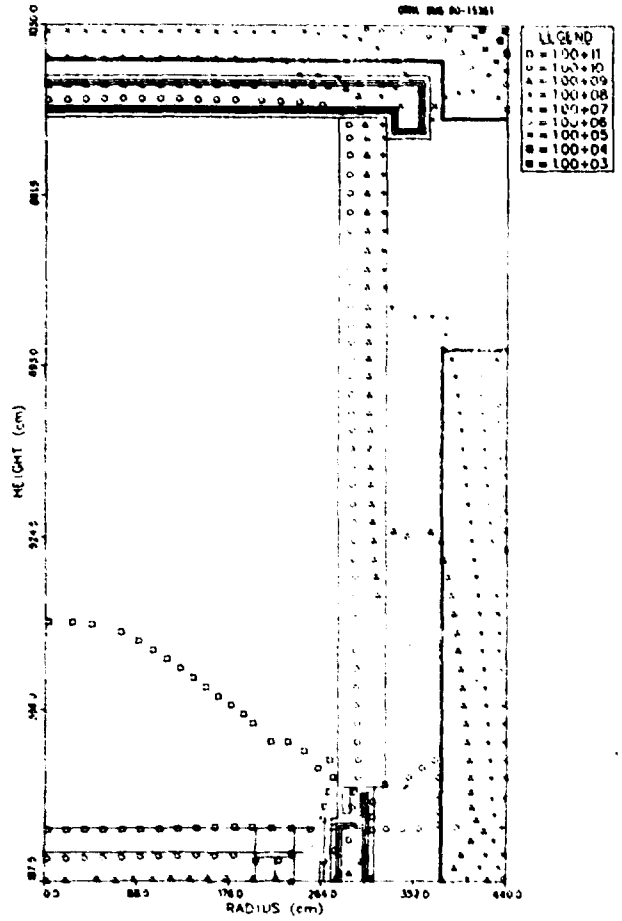

Fig. B-1. Isoplot of the total neutron flux ($cm^{-2} \cdot s^{-1}$) in the Conceptual Upflow GCFR upper regions.

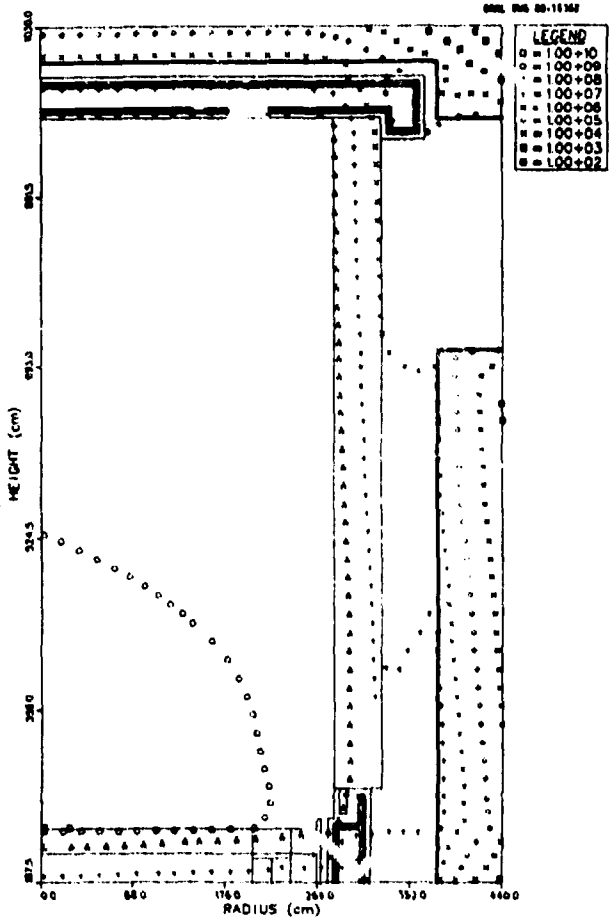

Fig. B-2. Isoplot of the fast (E > 1.0 MeV) neutron flux ($cm^{-2} \cdot s^{-1}$) in the Conceptual Upflow GCFR upper regions.

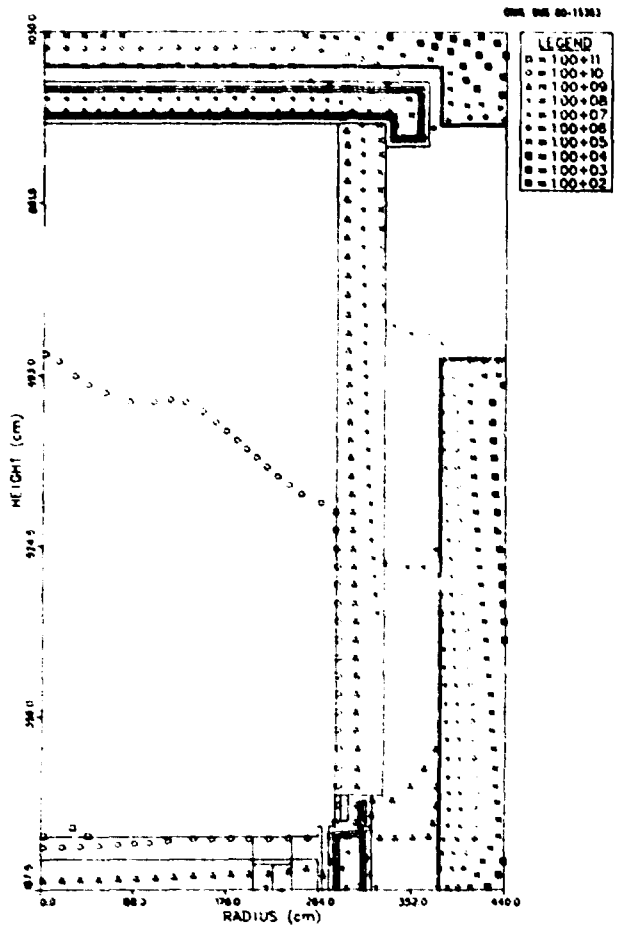

Fig. B-3. Isoplot of the fast (E > 0.1 MeV) neutron flux ($cm^{-2} \cdot s^{-1}$) in the Conceptual Upflow GCFR upper regions.

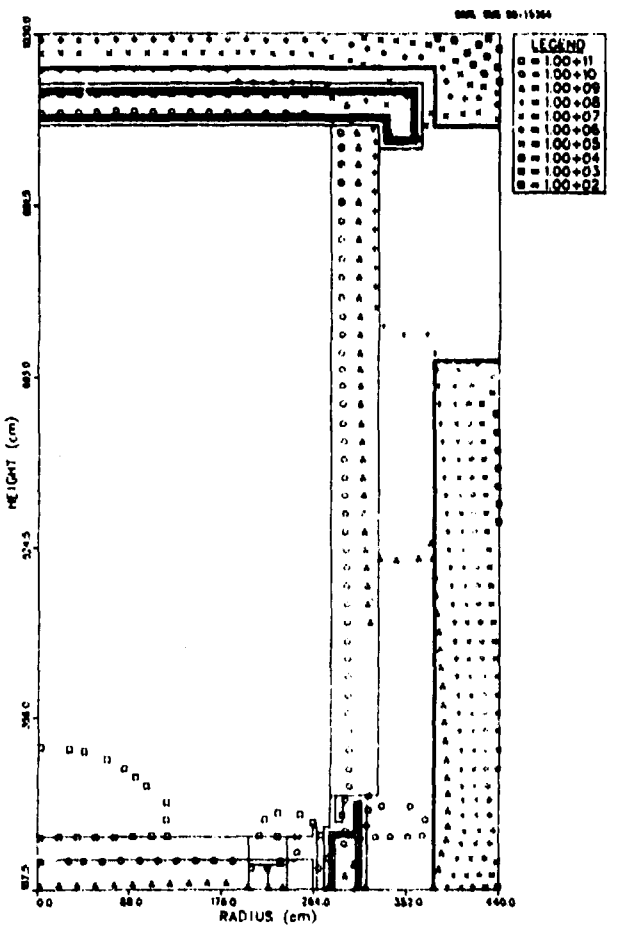

Fig. B-4. Isoplot of the intermediate (2.38 eV < E < 0.1 MeV) neutron flux ($cm^{-2} \cdot s^{-1}$) in the Conceptual Upflow GCFR upper regions.

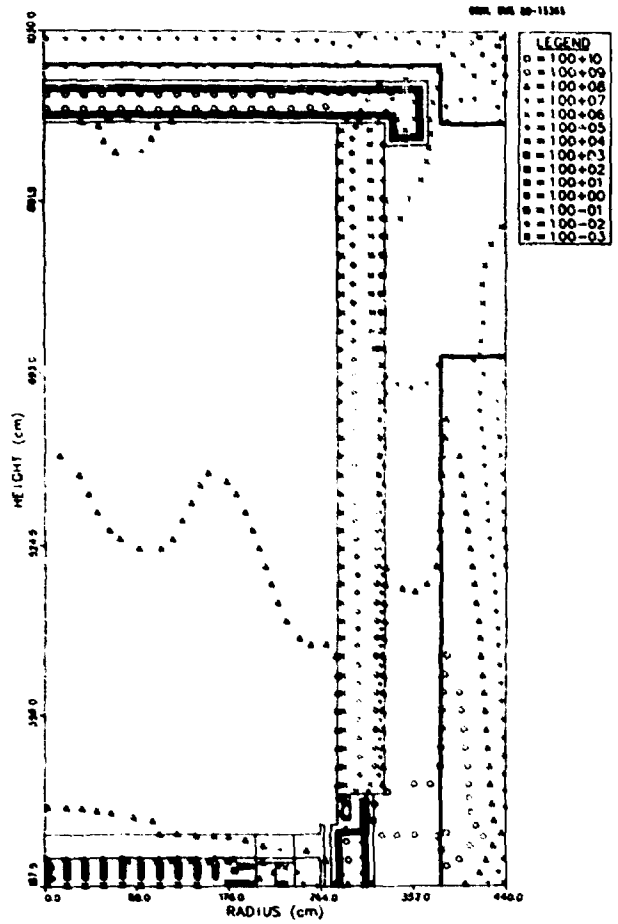

Fig. B-5. Isoplot of the thermal (E < 2.38 eV) neutron flux ($cm^{-2} \cdot s^{-1}$) in the Conceptual Upflow GCFR upper regions.

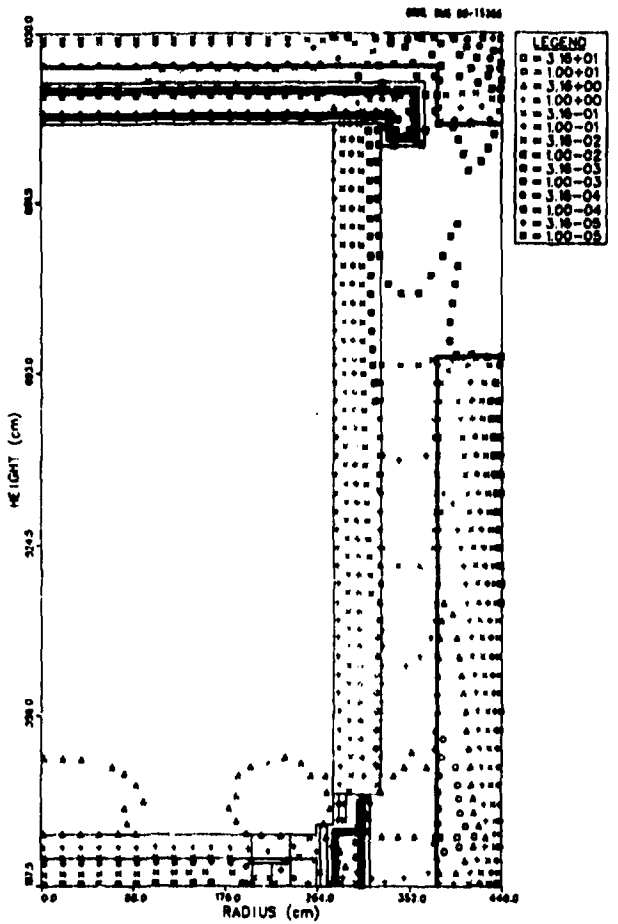

Fig. B-6. Isoplot of the heating (mW/cm^3) in boronated graphite in the Conceptual Upflow GCFR upper regions.

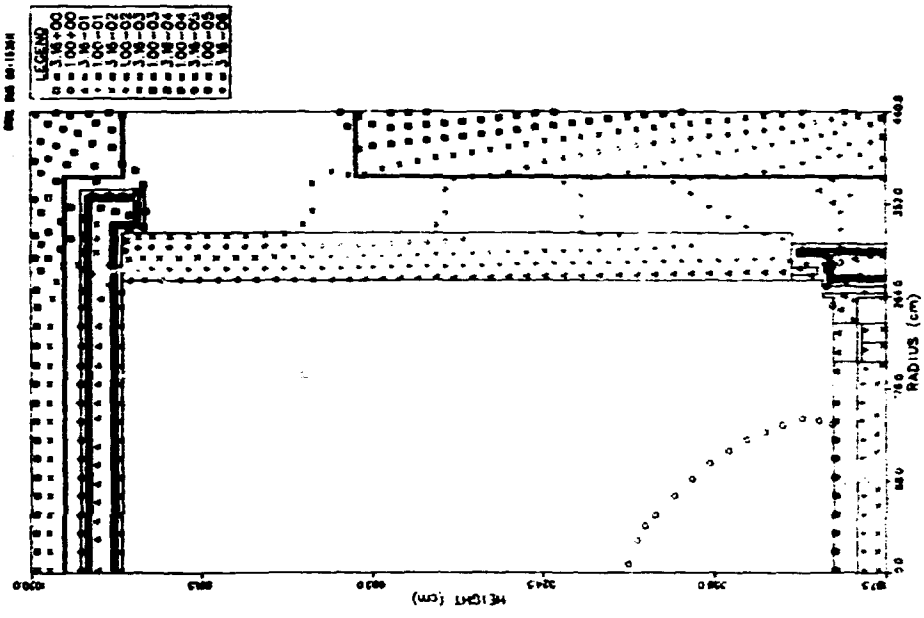

Fig. B-8. Isoplot of the total heating (mW/cm^3) in SS316 in the Conceptual Upflow GCFR upper regions.

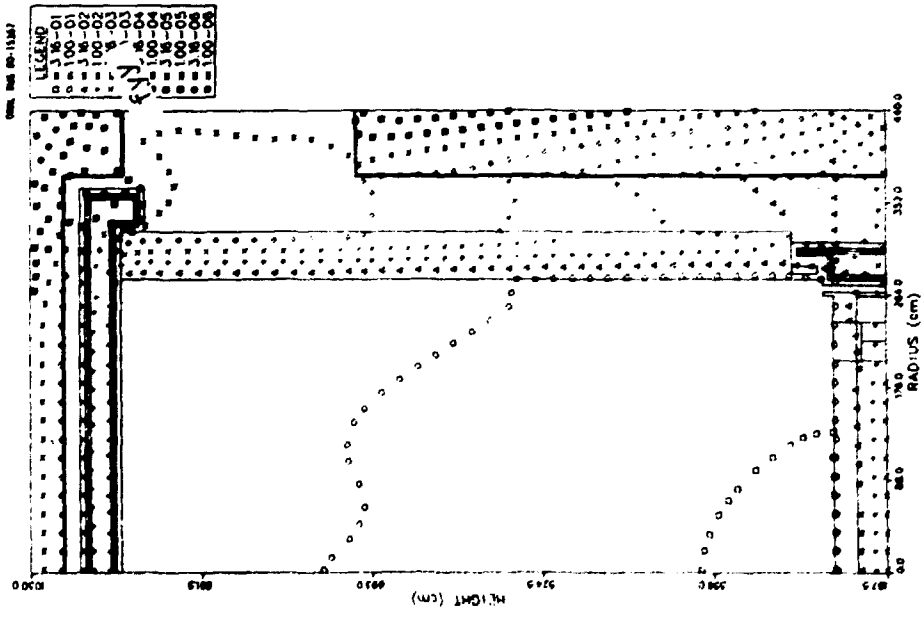

Fig. B-7. Isoplot of the total heating (mW/cm^3) in the Conceptual Upflow GCFR upper regions.

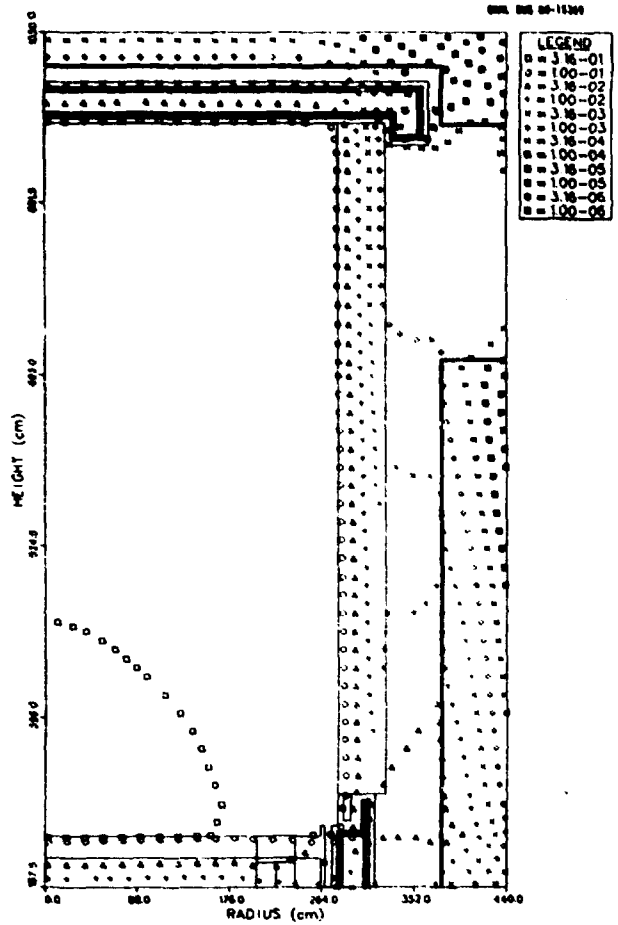

Fig. B-9. Isoplot of the total heating (mW/cm^3) in the Conceptual Upflow GCFR upper regions.

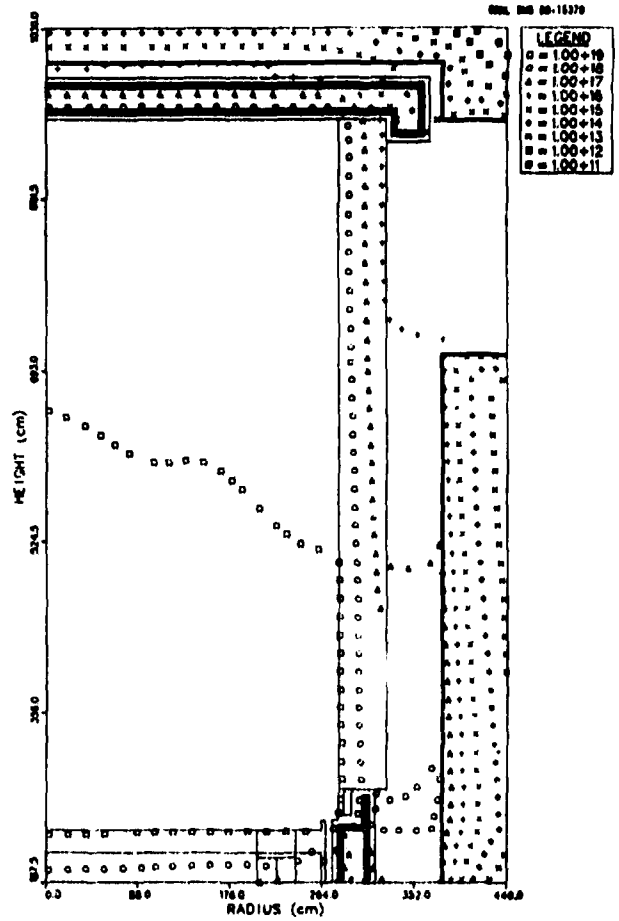

Fig. B-10. Isoplot of the equivalent fission fluence for graphite damage (cm^{-2}) in the Conceptual Upflow GCFR upper regions.

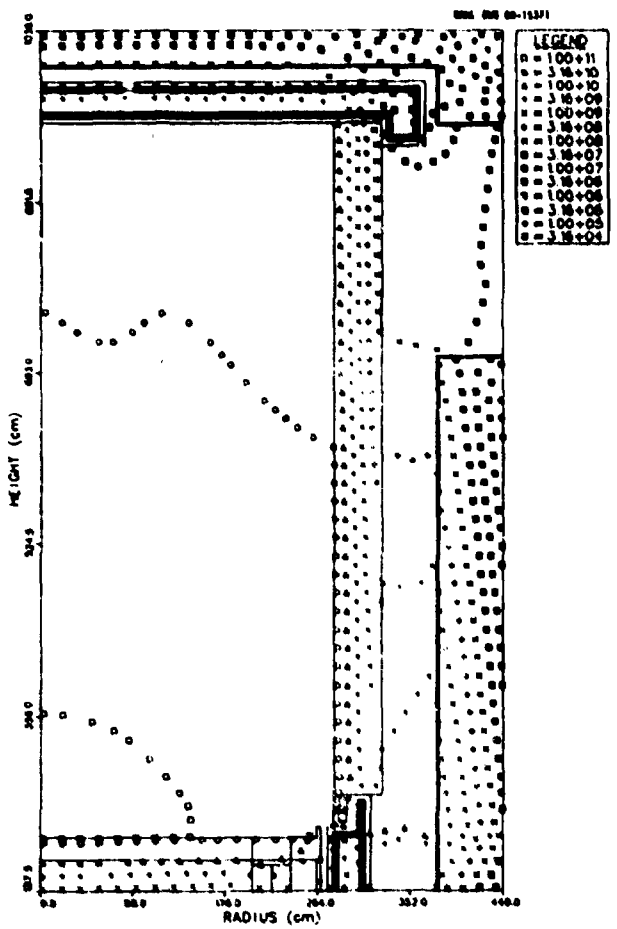

Fig. B-11. Isoplot of the total 24 full-power-year tissue dose (rd) in the Conceptual Upflow GCFR upper regions.

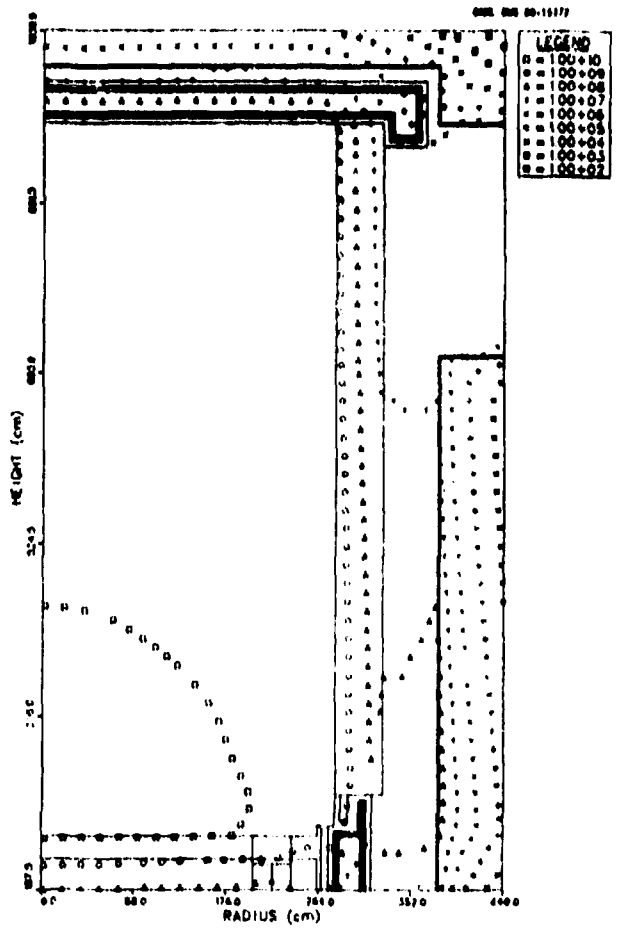

Fig. B-12. Isoplot of the total neutron energy flux ($MeV \cdot cm^{-2} \cdot s^{-1}$) in the Conceptual Upflow GCFR upper regions.

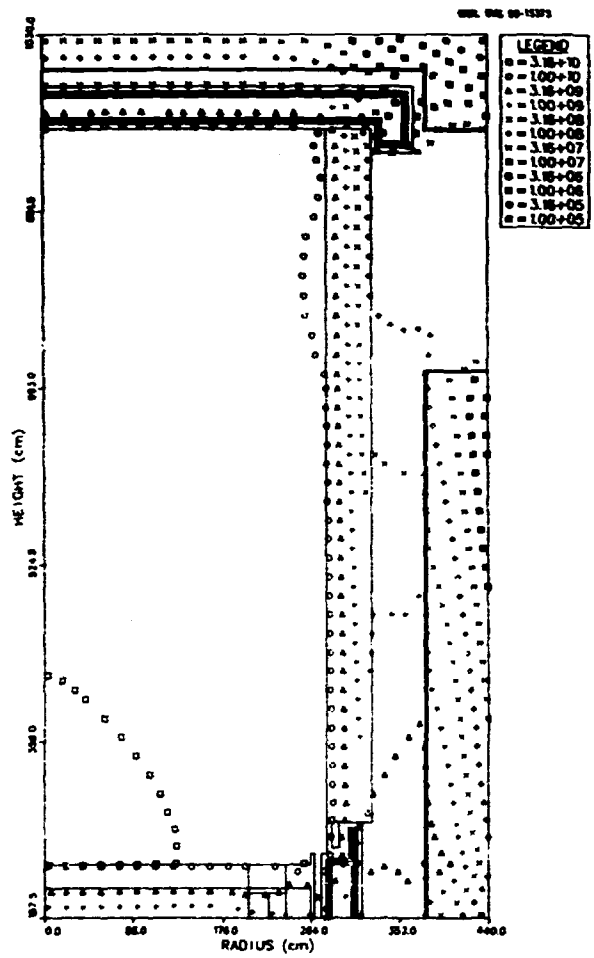

Fig. B-13. Isoplot of the total gamma-ray energy flux ($MeV \cdot cm^{-2} \cdot s^{-1}$) in the Conceptual Upflow GCFR upper regions.

Appendix C

Isoplots of Additional Activities for the Conceptual Upflow GCFR Lower Regions

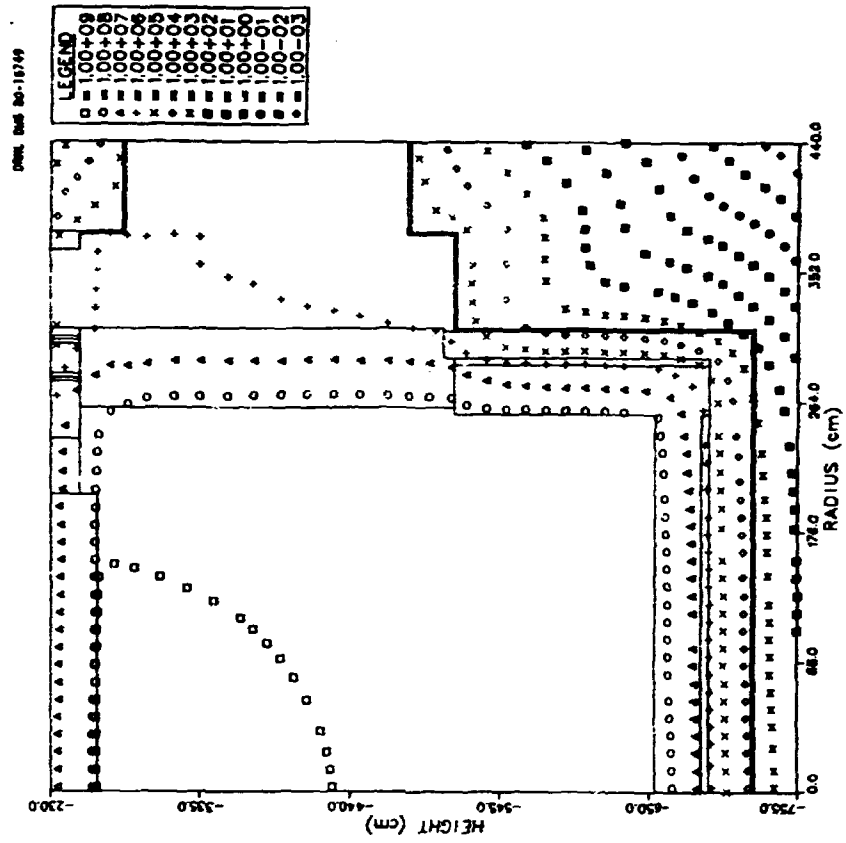

Fig. C-2. Isoplot of the fast ($E > 1.0$ MeV) neutron flux ($cm^{-2} \cdot s^{-1}$) in the Conceptual Upflow GCFR lower regions.

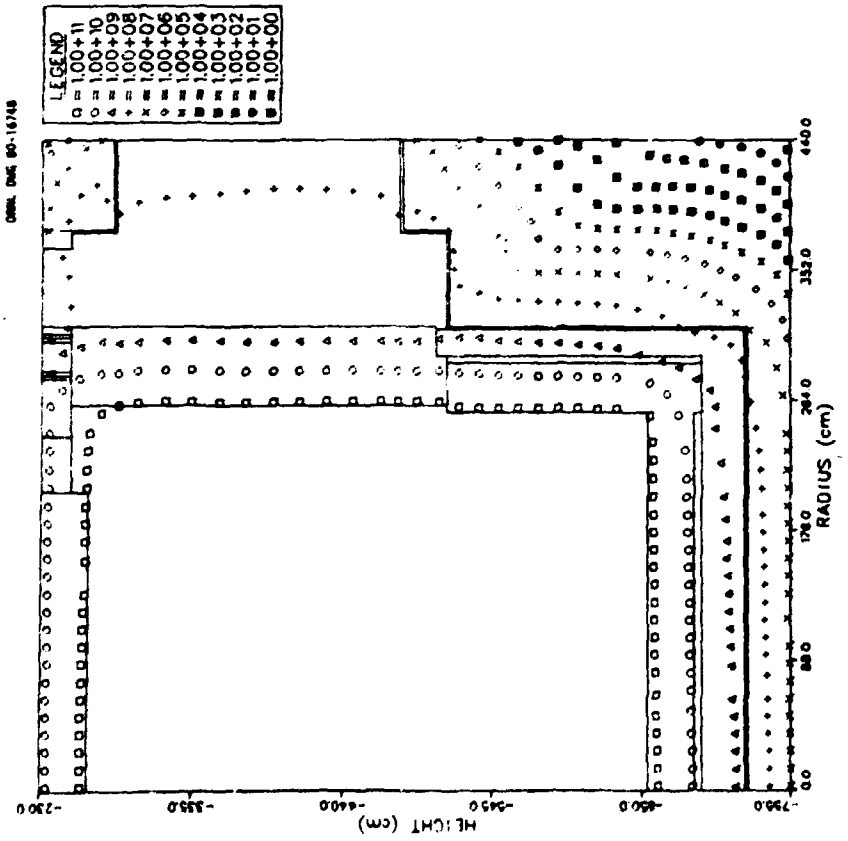

Fig. C-1. Isoplot of the total neutron flux ($cm^{-2} \cdot s^{-1}$) in the Conceptual Upflow GCFR lower regions.

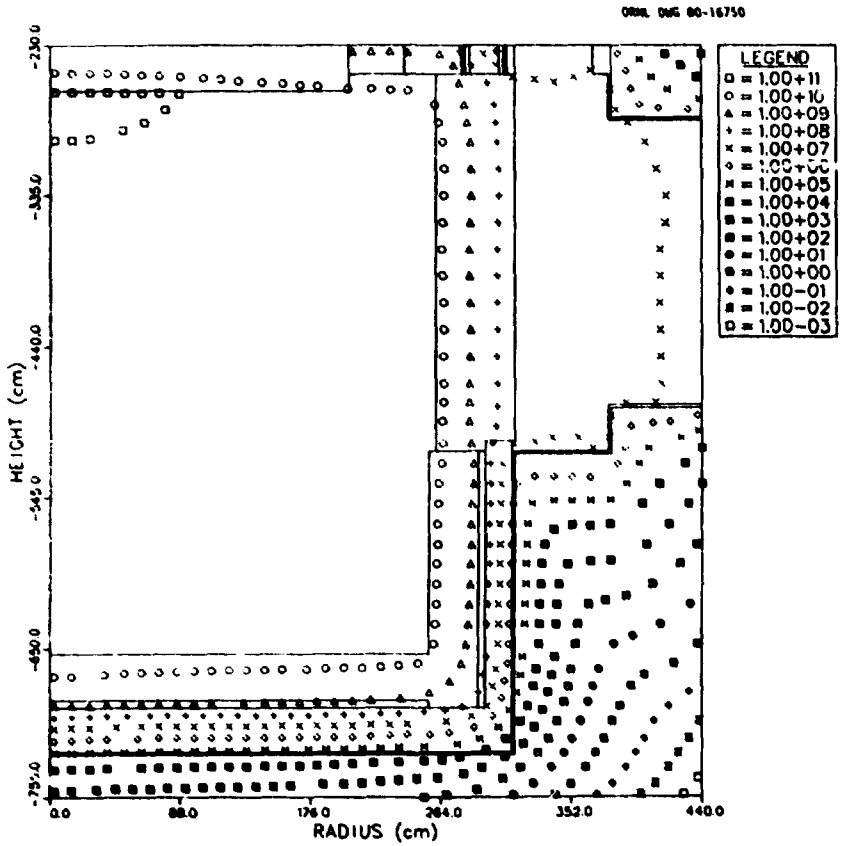

Fig. C-3. Isoplot of the fast (E > 0.1 MeV) neutron flux ($cm^{-2} \cdot s^{-1}$) in the Conceptual Upflow GCFR lower regions.

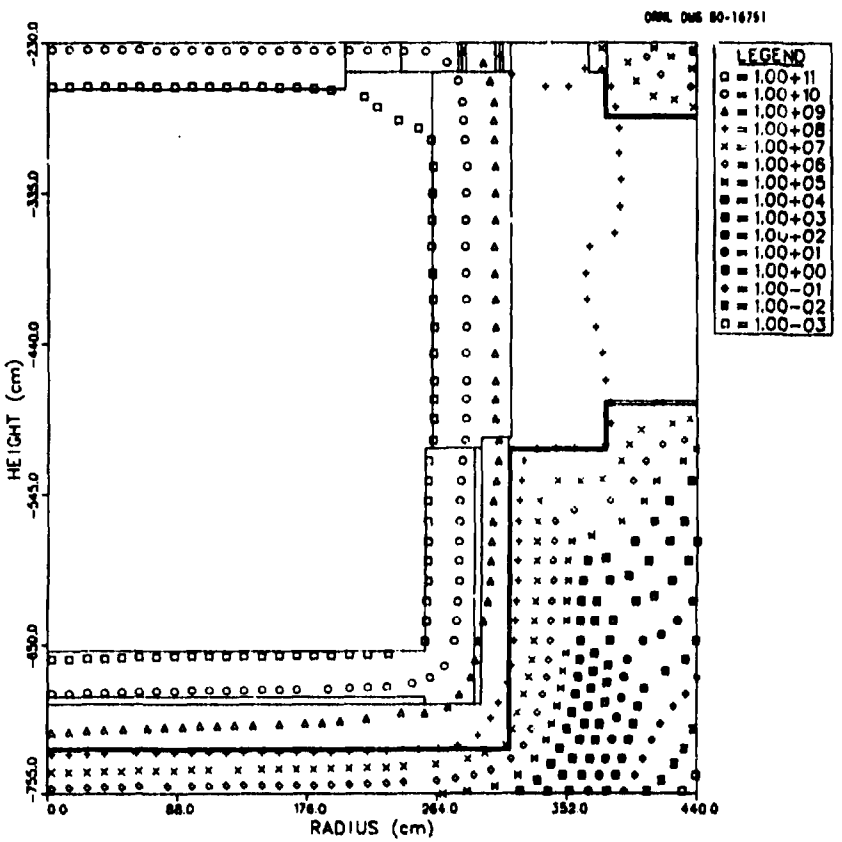

Fig. C-4. Isoplot of the intermediate (2.38 eV < E < 0.1 MeV) neutron flux ($cm^{-2} \cdot s^{-1}$) in the Conceptual Upflow GCFR lower regions.

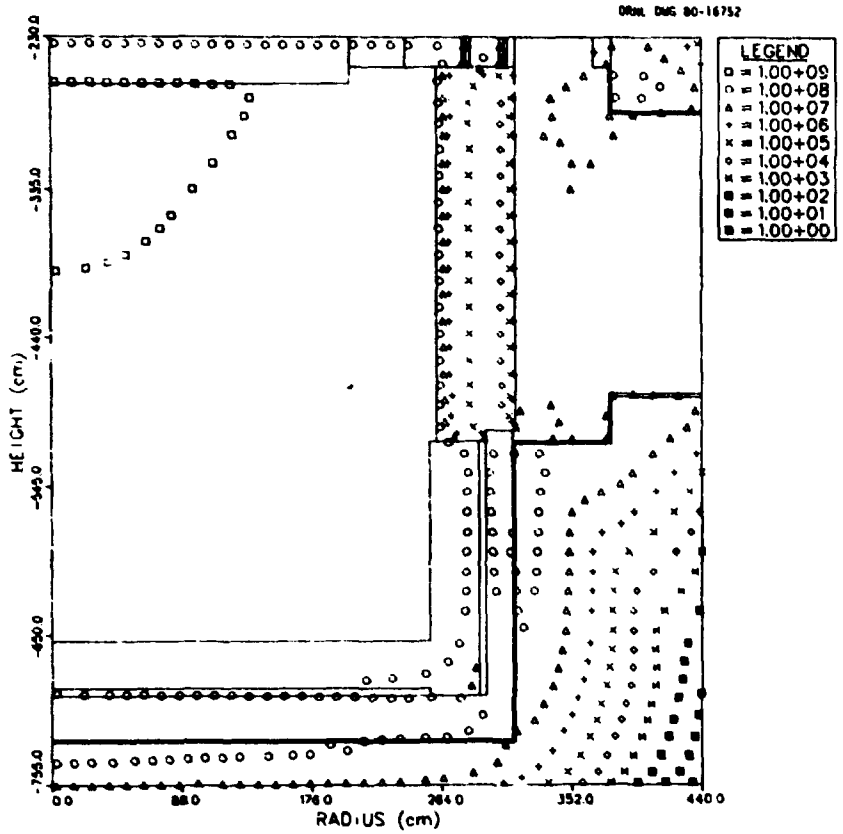

Fig. C-5. Isoplot of the thermal (E < 2.38 eV) neutron flux ($cm^{-2} \cdot s^{-1}$) in the Conceptual Upflow GCFR lower regions.

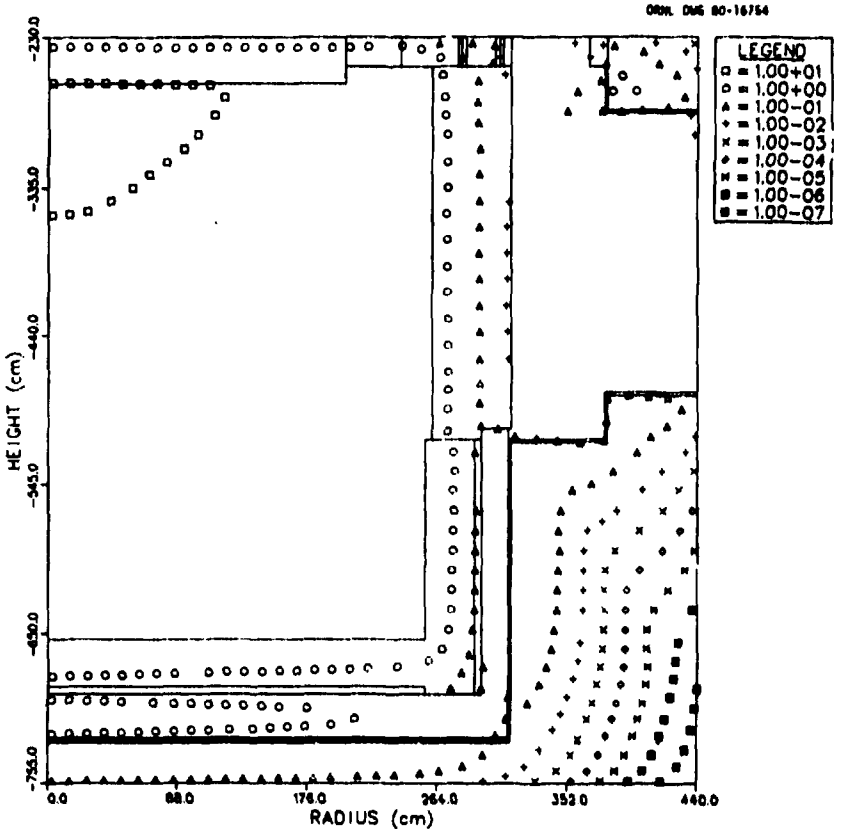

Fig. C-6. Isoplot of the total heating (mW/cm^3) in boronated graphite in the Conceptual Upflow GCFR lower regions.

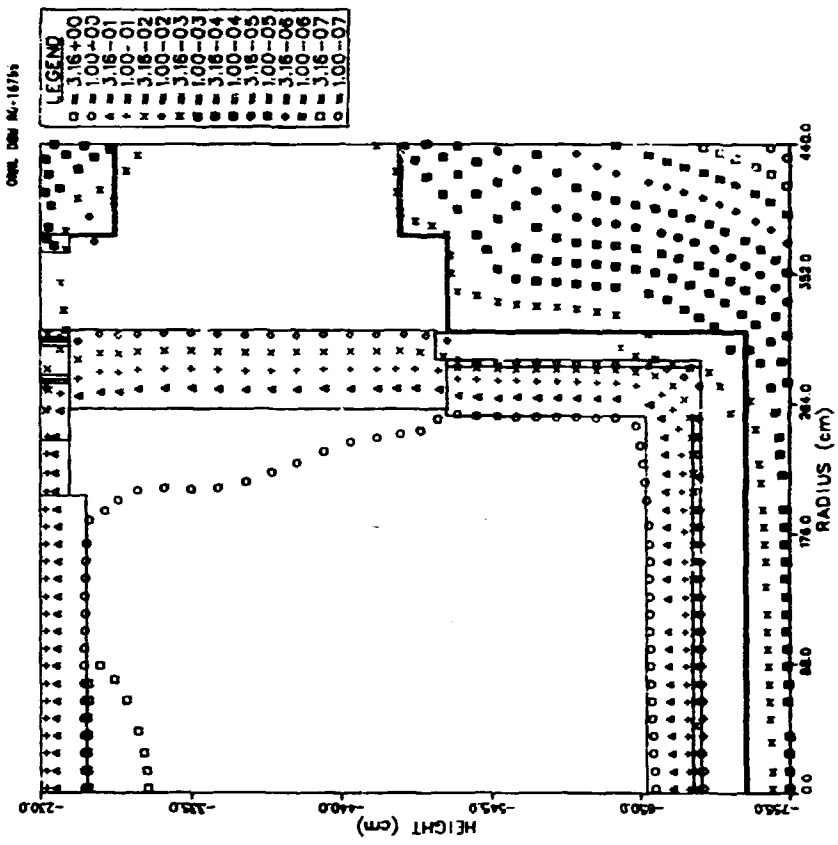

Fig. C-8. Isoplot of the total heating (mW/cm^3) in SS316 in the Conceptual Upflow GCFR lower regions.

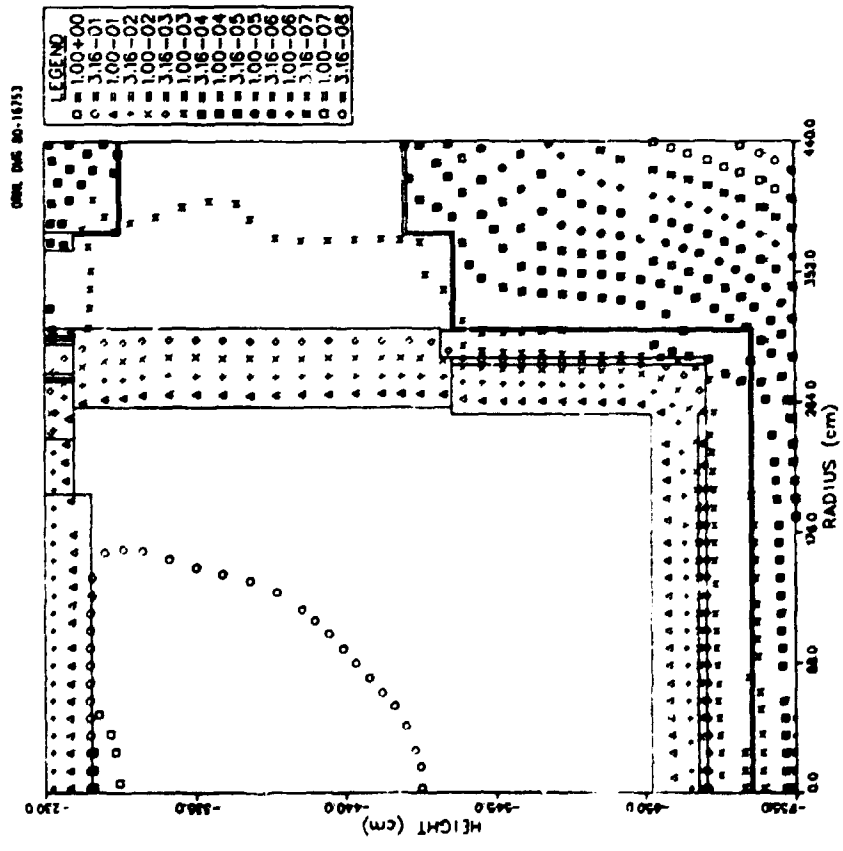

Fig. C-7. Isoplot of the total heating (mW/cm^3) in graphite in the Conceptual Upflow GCFR lower regions.

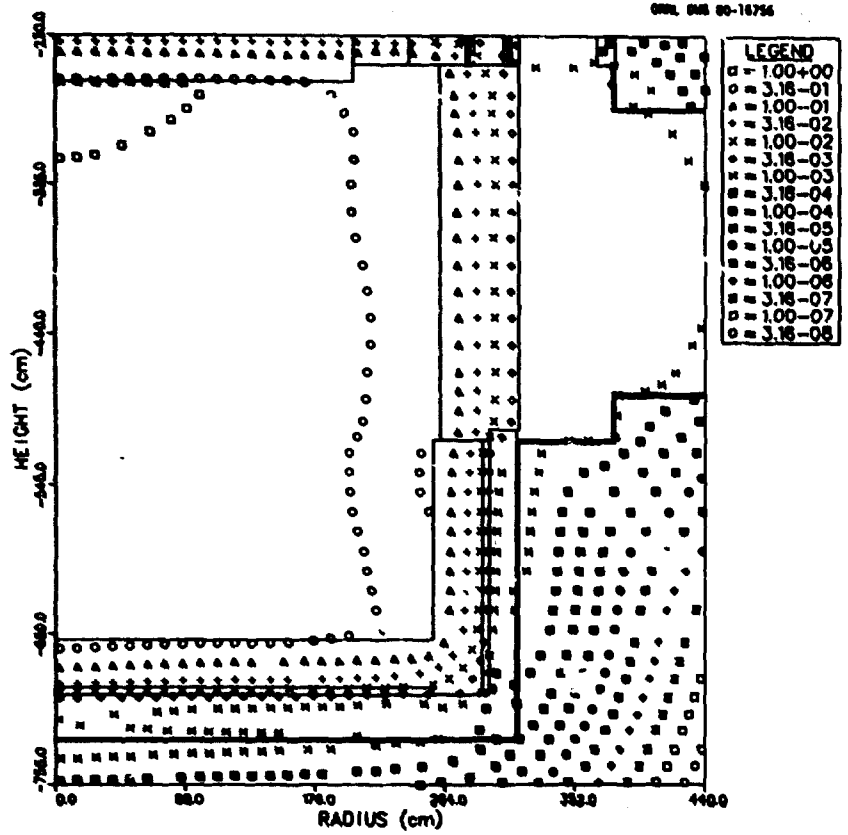

Fig. C-9. Isoplot of the total heating (mW/cm^3) in ordinary concrete in the Conceptual Upflow GCFR lower regions.

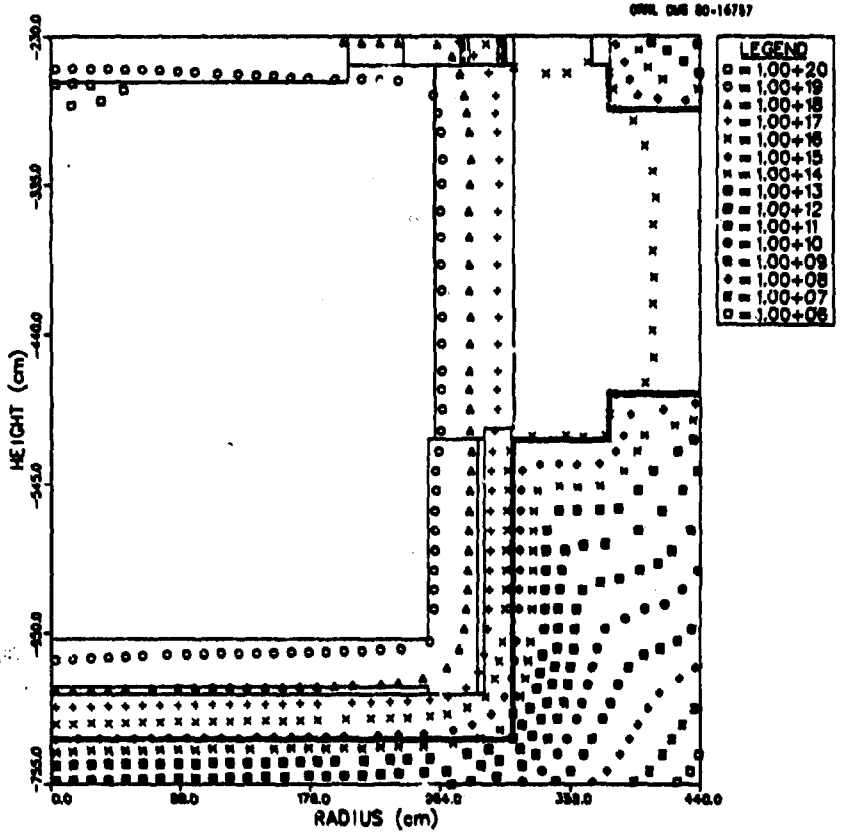

Fig. C-10. Isoplot of the equivalent fission fluence for graphite damage in the Conceptual Upflow GCFR lower regions.

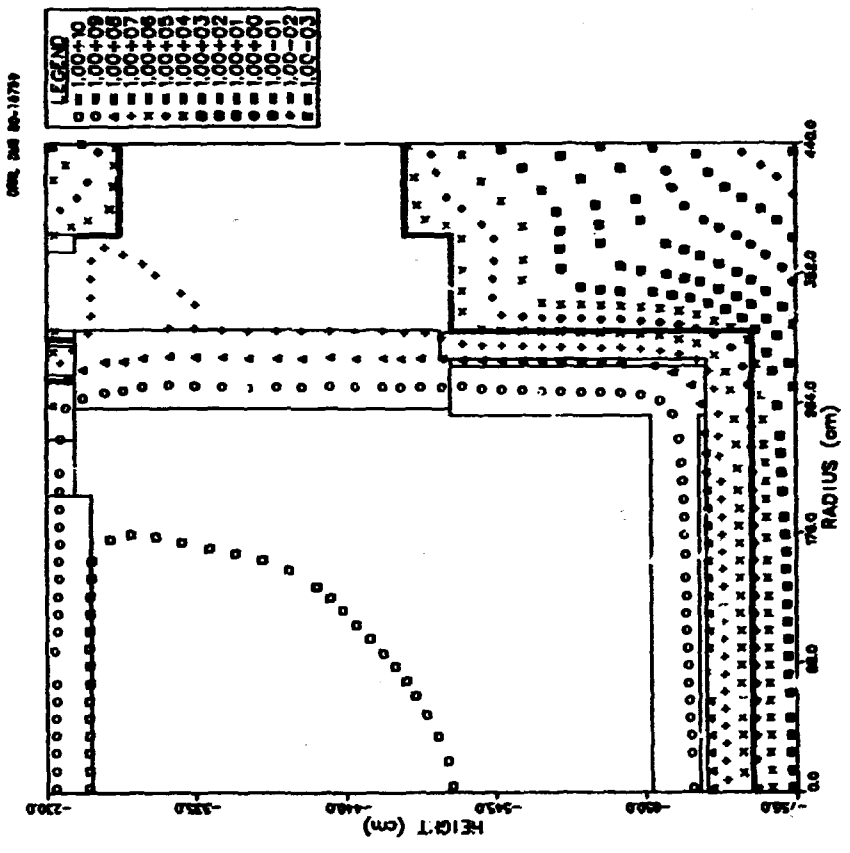

Fig. C-12. Isoplot of the total neutron energy flux ($MeV \cdot cm^{-2} \cdot s^{-1}$) in the Conceptual Upflow GCFR lower regions.

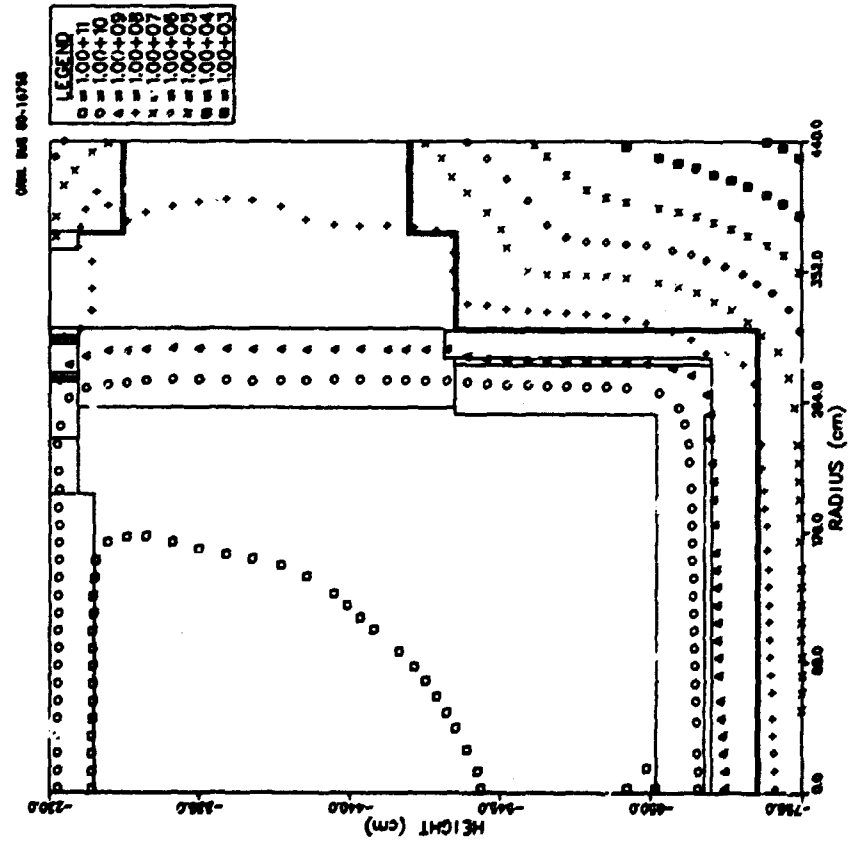

Fig. C-11. Isoplot of the total tissue dose (rd) in the Conceptual Upflow GCFR lower regions.

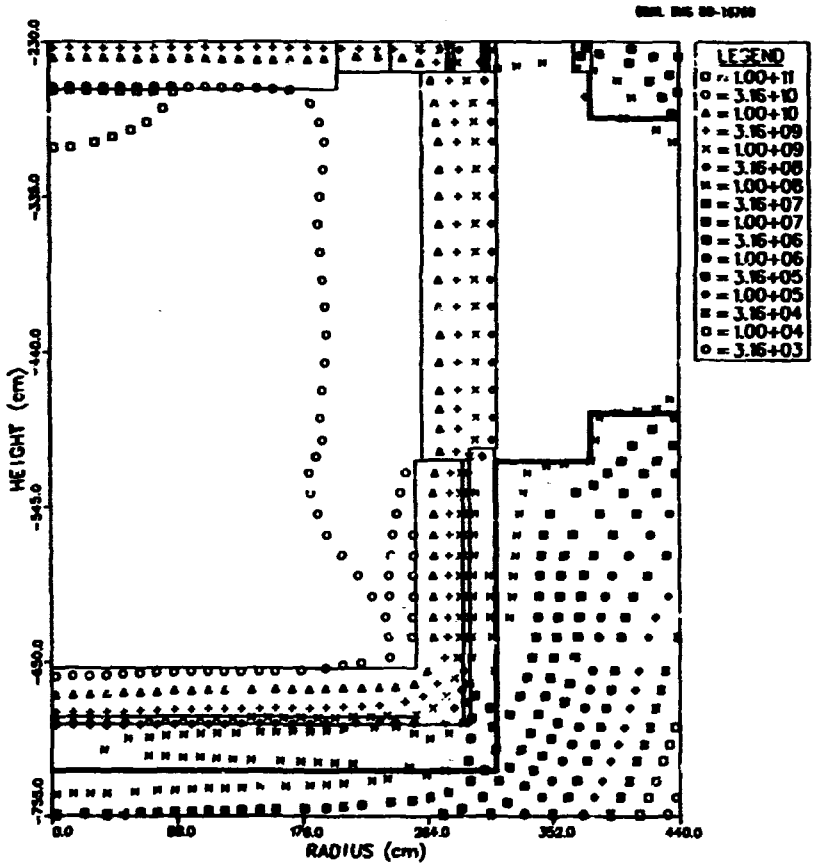

Fig. C-13. Isoplot of the total gamma-ray energy flux ($MeV \cdot cm^{-2} \cdot s^{-1}$) in the Conceptual Upflow GCFR lower regions.

Appendix D

Isoplots of Additional Activities for the GCFR Plenum Flow-Through Shield Analysis

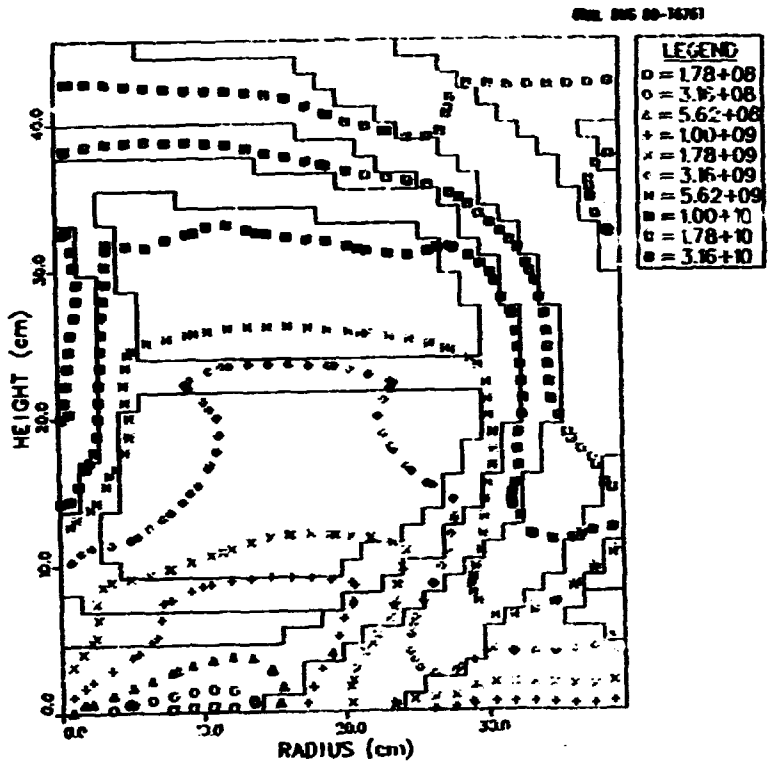

Fig. D-1. Isoplot of the total neutron flux ($cm^{-2} \cdot s^{-1}$) in a heterogeneous cell mockup of the GCFR upper plenum flow-through shield.

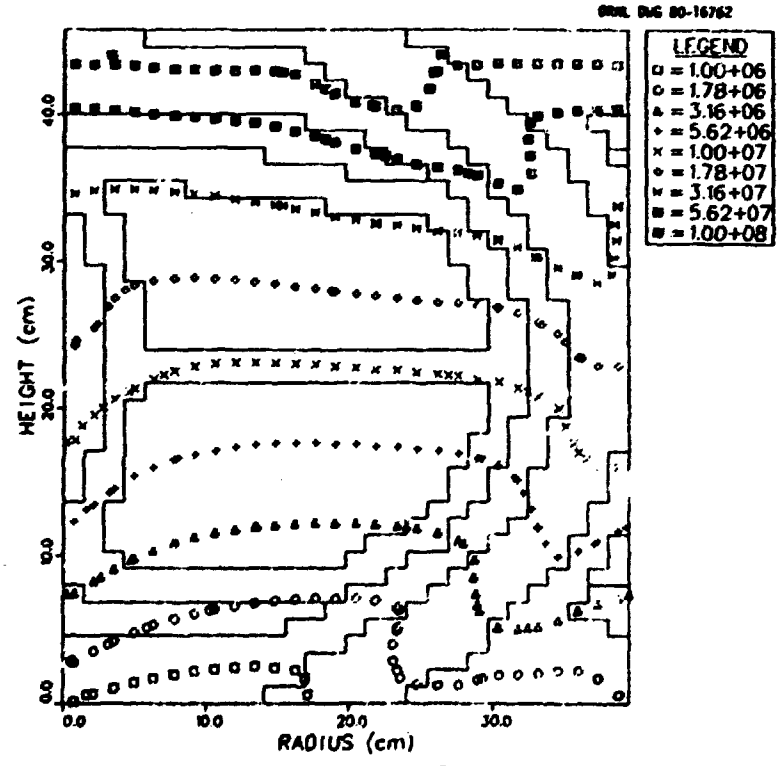

Fig. D-2. Isoplot of the fast energy (E > 1.0 MeV) neutron flux ($cm^{-2} \cdot s^{-1}$) in a heterogeneous cell mockup of the GCFR upper plenum flow-through shield.

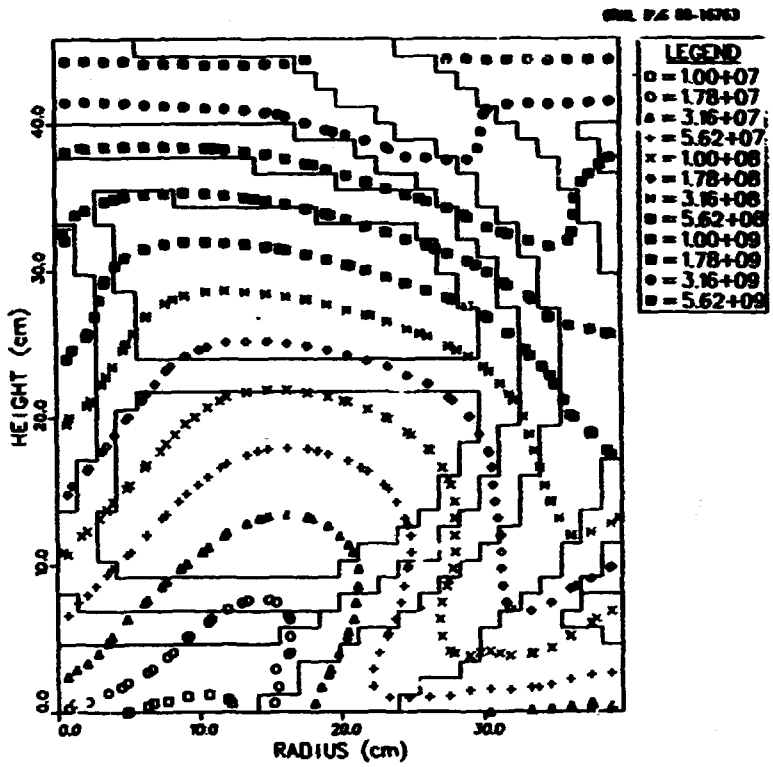

Fig. D-3. Isoplot of the fast energy (E > 0.1 MeV) neutron flux ($cm^{-2}.s^{-1}$) in a heterogeneous cell mockup of the GCFR upper plenum flow-through shield.

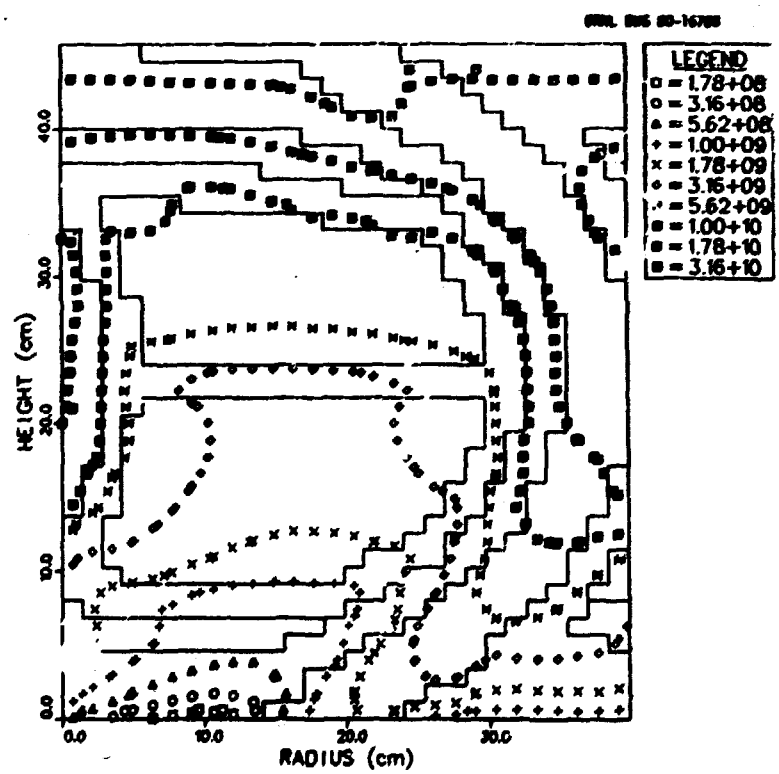

Fig. D-4. Isoplot of the intermediate energy (2.38 eV < E < 0.1 MeV) neutron flux ($cm^{-2}.s^{-1}$) in a heterogeneous cell mockup of the GCFR upper plenum flow-through shield.

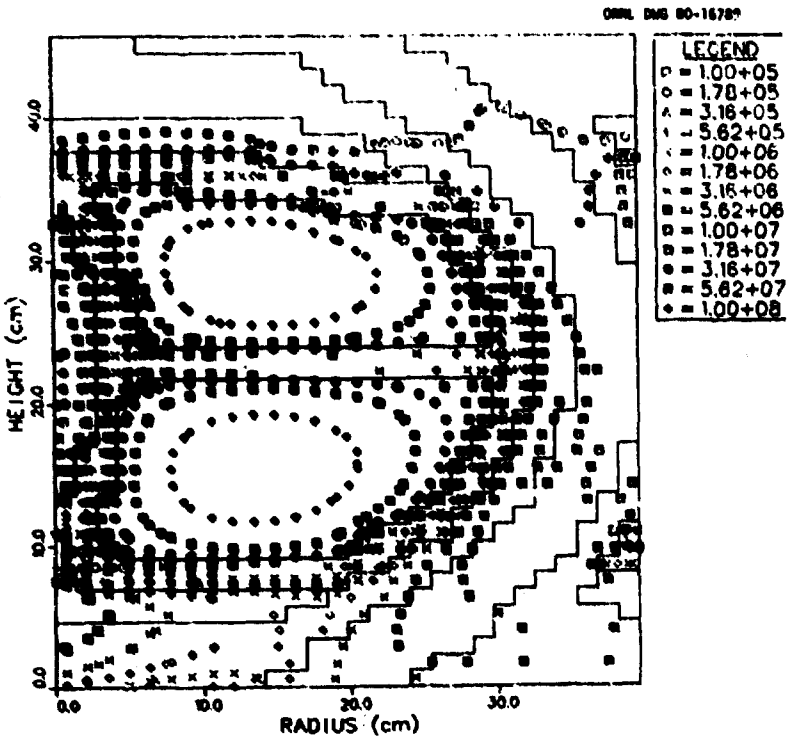

Fig. D-5. Isoplot of the thermal energy (E < 2.38 eV) neutron flux ($cm^{-2}.s^{-1}$) in a heterogeneous cell mockup of the GCFR upper plenum flow-through shield.

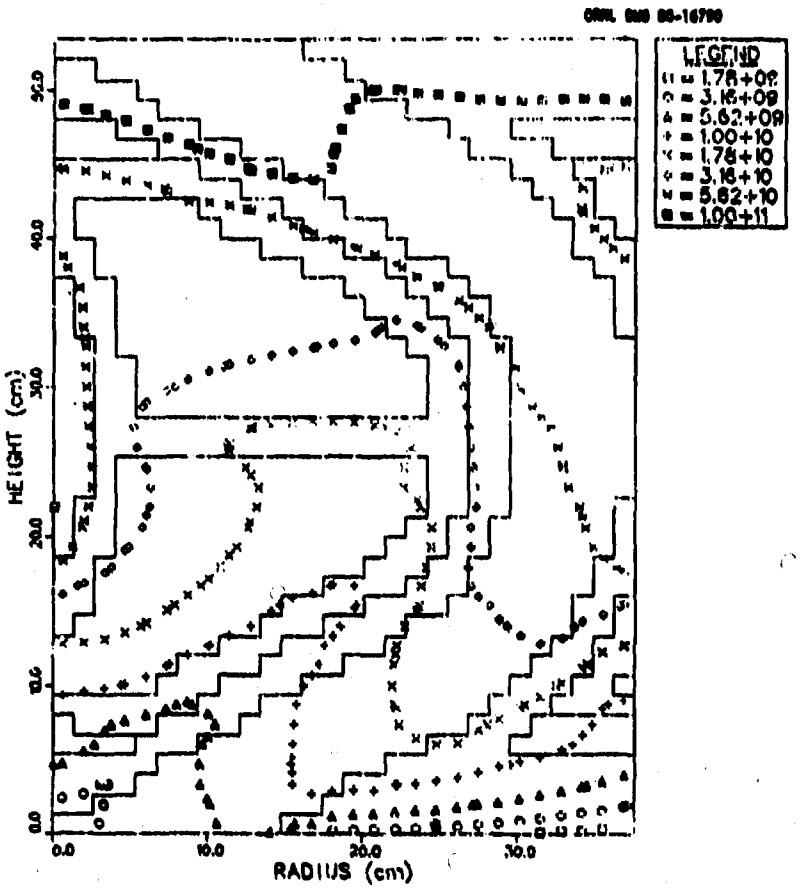

Fig. D-6. Isoplot of the total neutron flux ($cm^{-2}.s^{-1}$) in a heterogeneous cell mockup of the GCFR lower plenum flow-through shield.

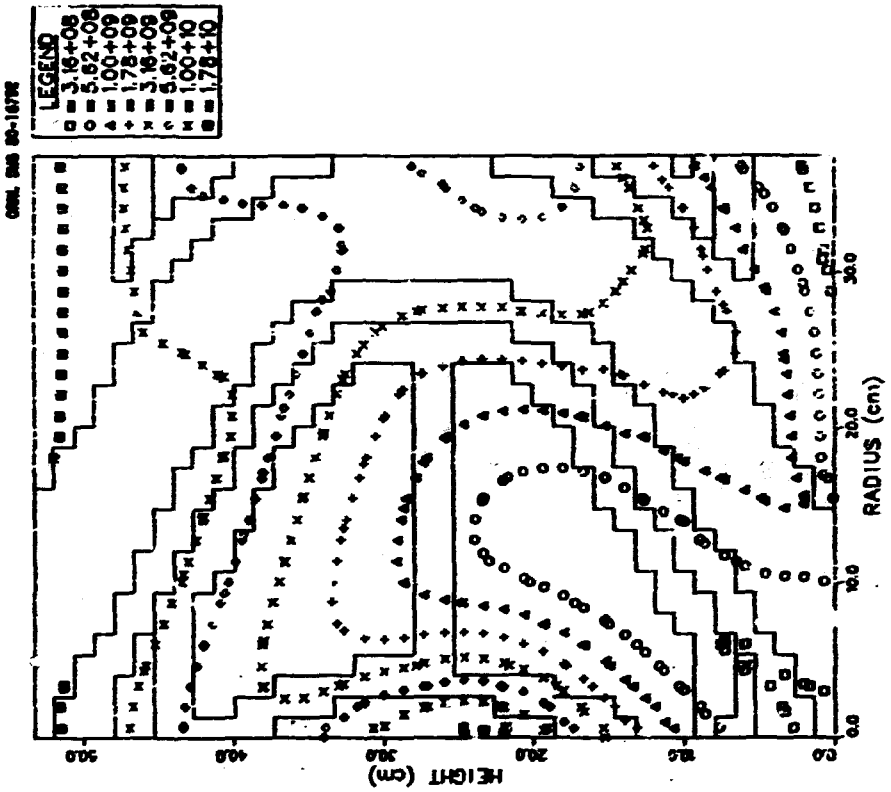

Fig. D-8. Isoplot of the fast energy (E > 0.1 MeV) neutron flux ($cm^{-2}.s^{-1}$) in a heterogeneous cell mockup of the GCFR lower plenum flow-through shield.

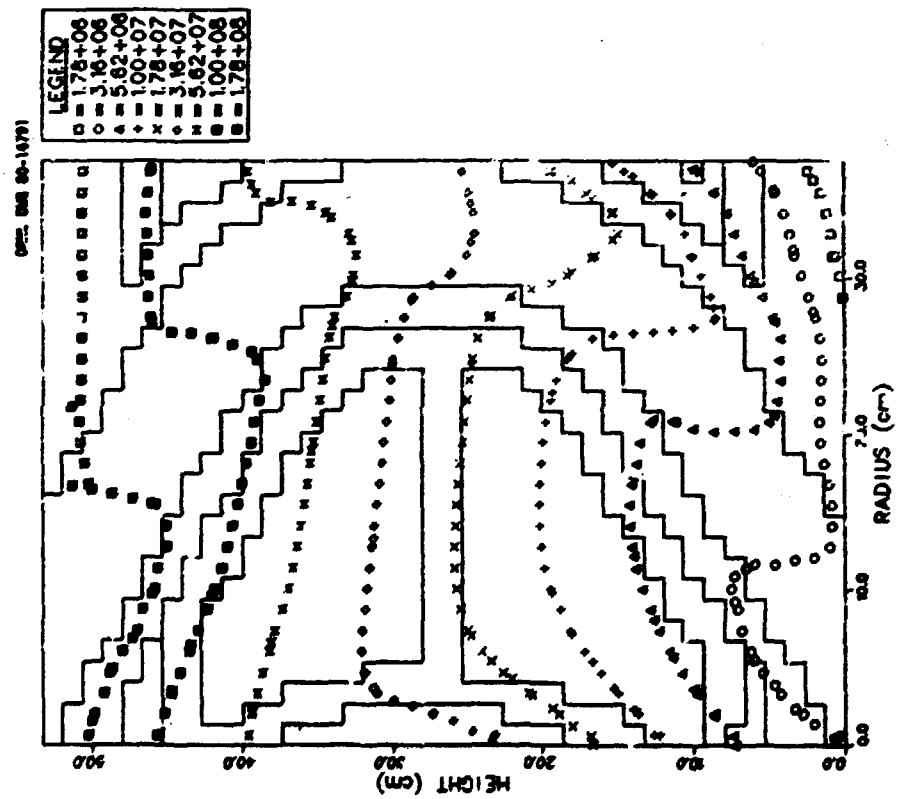

Fig. D-7. Isoplot of the fast energy (E > 1.0 MeV) neutron flux ($cm^{-2}.s^{-1}$) in a heterogeneous cell mockup of the GCFR lower plenum flow-through shield.

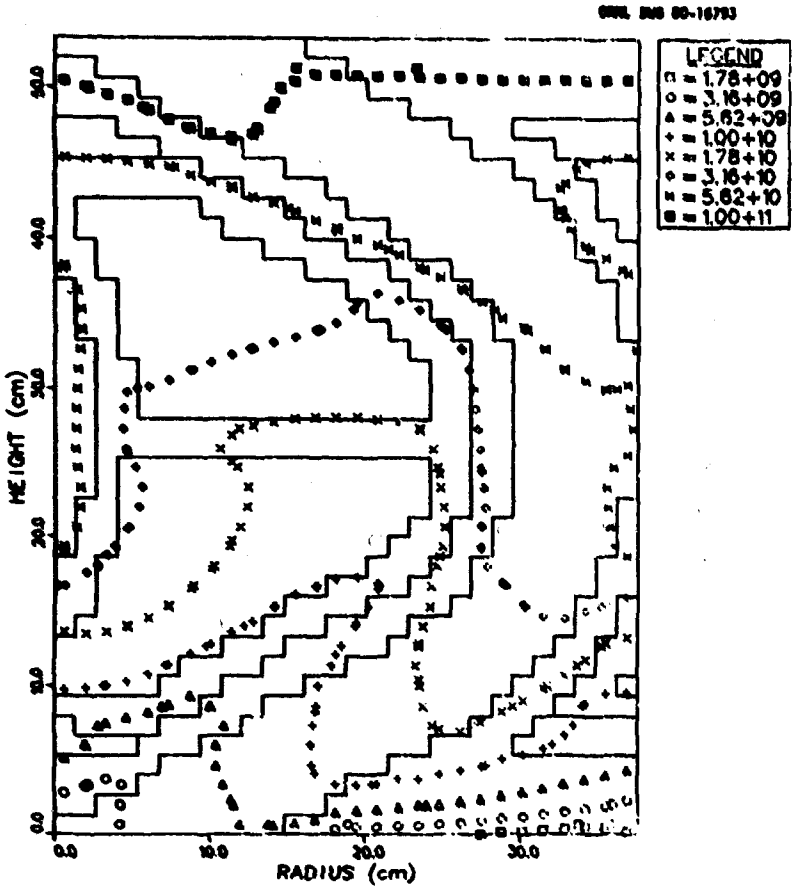

Fig. D-9. Isoplot of the intermediate energy (2.38 eV < E < 0.1 MeV) neutron flux ($cm^{-2} \cdot s^{-1}$) in a heterogeneous cell mockup of the GCFR lower plenum flow-through shield.

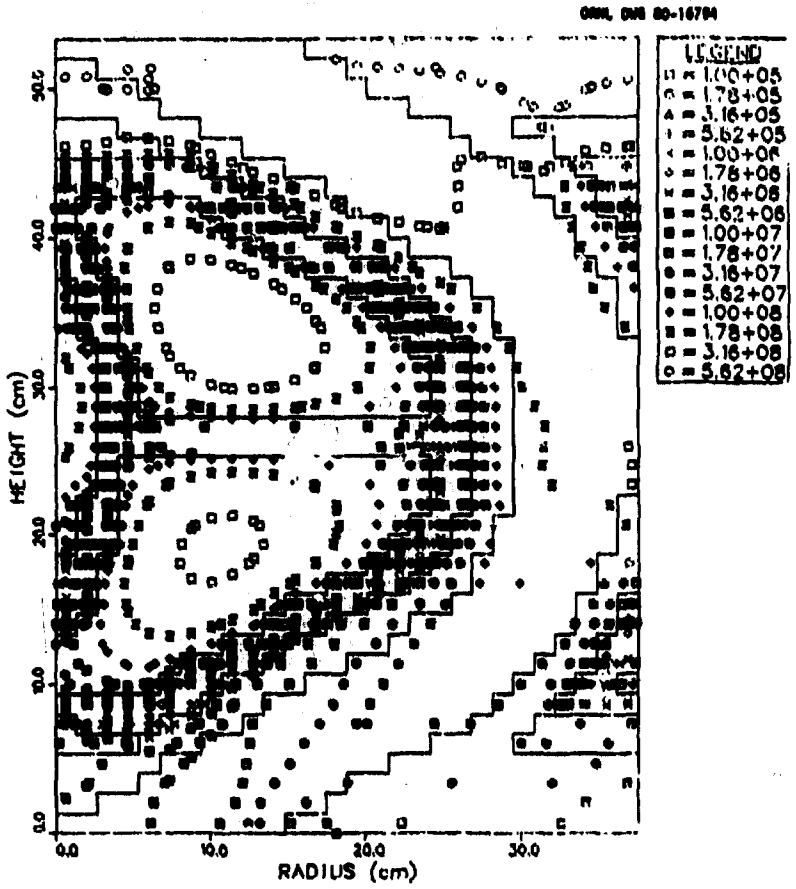

Fig. D-10. Isoplot of the thermal energy (E < 2.38 eV) neutron flux ($cm^{-2} \cdot s^{-1}$) in a heterogeneous cell mockup of the GCFR lower plenum flow-through shield.

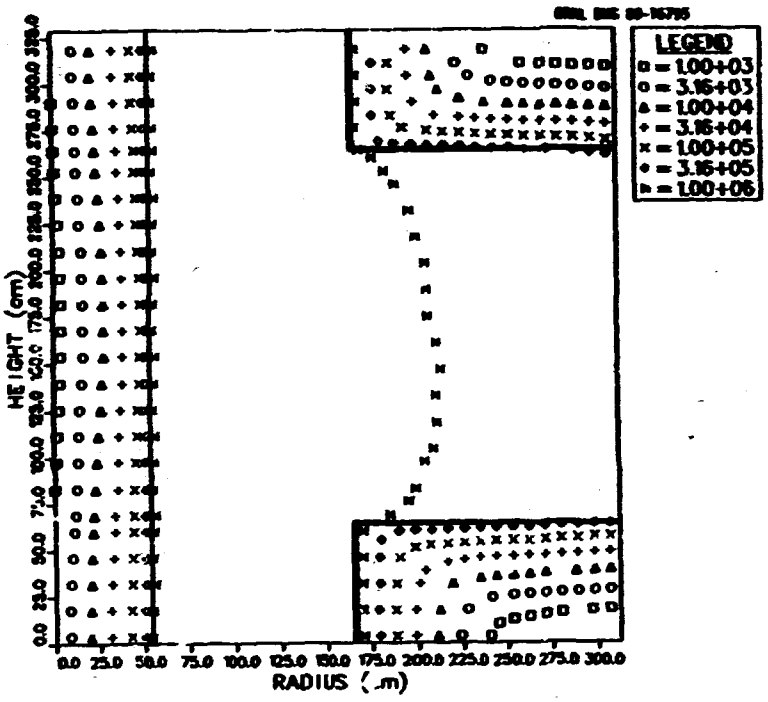

Fig. D-11. Isoplot of the fast energy (E > 1.0 MeV) neutron flux ($cm^{-2} \cdot s^{-1}$) in the Upflow GCFR inlet coolant duct region.

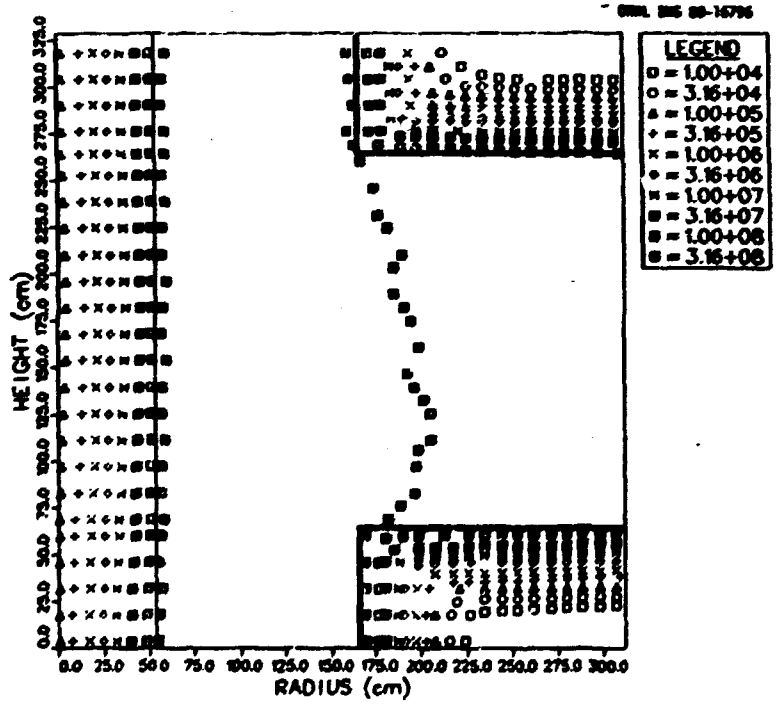

Fig. D-12. Isoplot of the fast energy (E > 0.1 MeV) neutron flux ($cm^{-2} \cdot s^{-1}$) in the Upflow GCFR inlet coolant duct region.

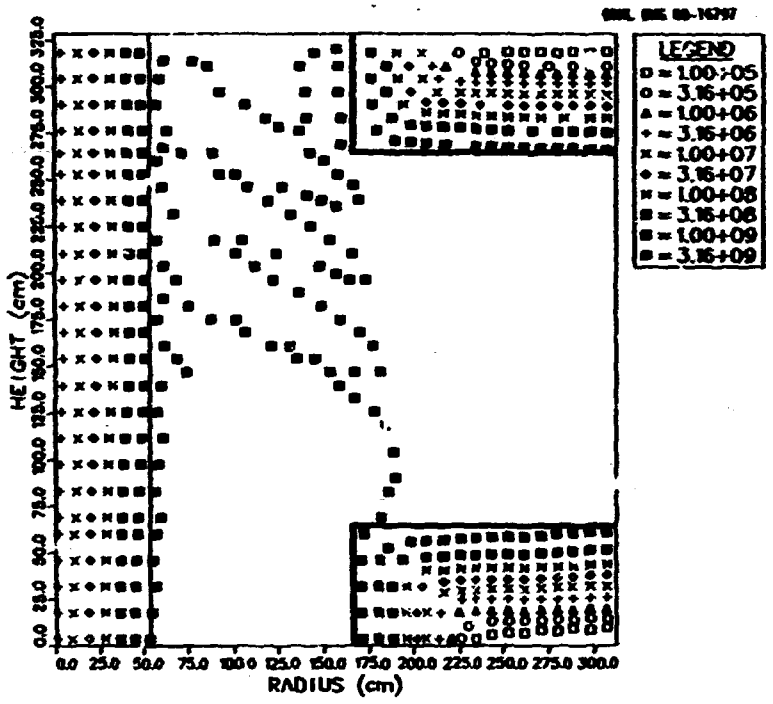

Fig. D-13. Isoplot of the intermediate energy (2.38 eV < E < 0.1 MeV) neutron flux ($cm^{-2} \cdot s^{-1}$) in the Upflow GCFR inlet coolant duct region.

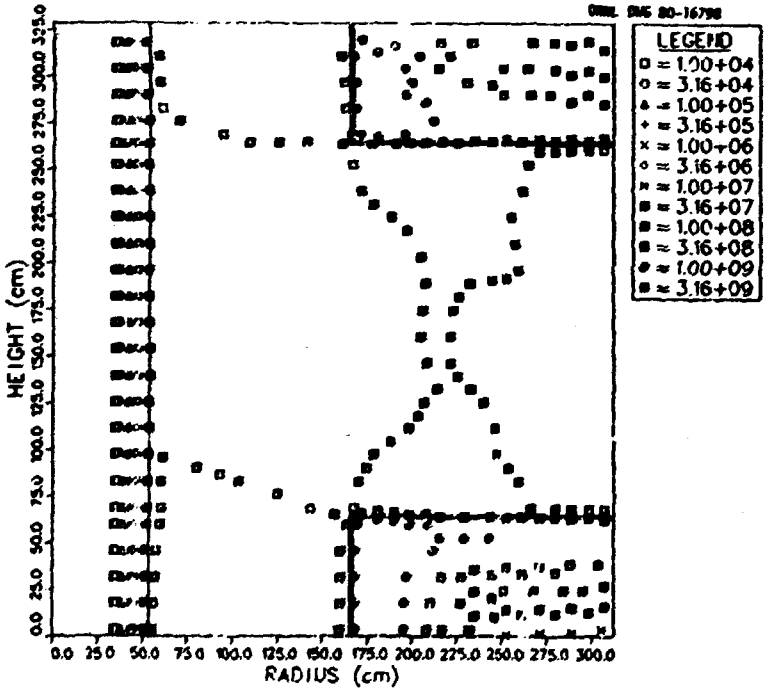

Fig. D-14. Isoplot of the thermal energy (E < 2.38 eV) neutron flux ($cm^{-2} \cdot s^{-1}$) in the Upflow GCFR coolant duct region.